THE UNIVERSITY OF
WARWICK

AUTHOR: **José Francisco Hernández Valle** DEGREE: **Ph.D.**

TITLE: **Pulsed-electromagnet EMAT for high temperature applications**

DATE OF DEPOSIT: .....

I **agree** that this thesis shall be available in accordance with the regulations governing the University of Warwick theses.

I **agree** that the summary of this thesis may be submitted for publication.

I **agree** that the thesis may be photocopied (single copies for study purposes only).

Theses with no restriction on photocopying will also be made available to the British Library for microfilming. The British Library may supply copies to individuals or libraries. subject to a statement from them that the copy is supplied for non-publishing purposes. All copies supplied by the British Library will carry the following statement:

> "Attention is drawn to the fact that the copyright of this thesis rests with its author. This copy of the thesis has been supplied on the condition that anyone who consults it is understood to recognise that its copyright rests with its author and that no quotation from the thesis and no information derived from it may be published without the author's written consent."

AUTHOR'S SIGNATURE: .....

USER'S DECLARATION

1. I undertake not to quote or make use of any information from this thesis without making acknowledgment to the author.
2. I further undertake to allow no-one else to use this thesis while it is in my care.

DATE SIGNATURE ADDRESS

.....

.....

.....

.....

.....

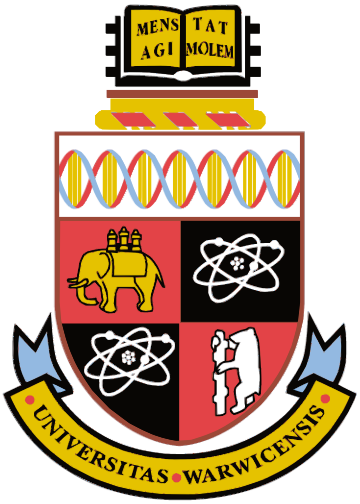

Pulsed-electromagnet EMAT for high temperature applications

by

José Francisco Hernández Valle

Thesis

Submitted to the University of Warwick

for the degree of

Doctor of Philosophy

Department of Physics

September 2011

THE UNIVERSITY OF WARWICK

Contents

List of Figures

List of Tables

Acknowledgments

I would like to sincerely thank my supervisor Dr. Steve Dixon for his excellent guidance, support and advice given to me throughout all this work. I am very grateful to him for giving me the opportunity to be part of the Ultrasonics group; which provided me with a lively and stimulating research environment. I would therefore like to extend my thanks to Dr. Rachel Edwards, Charley Fan, Philip Petcher, Steve Essex, Mark Potter, Sue Burrows, Hashimi Rosli, Tim Harrison, Samuel Hill, and all other colleagues with whom I enjoyed sharing time both in and outside the department.

I am indebted to Bob Day and David Greenshields from the Electronic Workshop, to Bob Bridgland and his team from the Mechanical Workshop, and finally to Tom Orthon, for their invaluable help and advice in the experimental part of this thesis, without them this research would probably have not materialized.

I also want to express my deepest gratitude to my family for their support throughout my studies. I have always felt that you were very close over the years despite the distance. Heartfelt thanks goes to my beloved Corita for standing by me every day and for continuously renewing my enthusiasm, without you the work would have been a great deal harder.

Lastly, I would like to acknowledge the funding provided by the Mexican National Council on Science and Technology (CONACYT) for the duration of my PhD.

Declarations

The work presented in this thesis is my original research. Wherever contributions of others are involved, every effort is made to indicate this clearly, with due reference to the literature, and acknowledgment of collaborative research and discussions. The work was done under the guidance of Dr. Steve Dixon at the Department of Physics, in the University of Warwick, during the period between October 2007 and September 2011.

No part of this work has been previously submitted to the University of Warwick, nor any other academic institution, for the admission to a higher degree. Some of the work has already appeared in the forms of publications, and those are listed in the List of publications section.

List of publications

1. F. Hernandez-Valle, S. Dixon. Pulsed electromagnet EMAT for ultrasonic measurements at elevated temperatures. Insight. Volume 53, pp. 96-99. February 2011. DOI: 10.1784/insi.2011.53.2.96

2. F. Hernandez-Valle, S. Dixon. Initial tests for designing a high temperature EMAT with pulsed electromagnet. NDT&E International, Volume 43, pp. 171-175. March 2010. DOI:10.1016/j.ndteint.2009.10.009

3. F. Hernandez-Valle, S. Dixon. Pulsed electromagnet EMAT for high temperature. In: AIP Conference proceedings 1211, Review of Progress in Quantitative Nondestructive Evaluation, Volume 29, pp. 957-962. July 2009.

4. S.B. Palmer, F. Hernandez-Valle, S. Dixon. Electromagnetic acoustic transduction using a pulsed electromagnet. In: SPIE Conference proceedings, Volume 7294, pp. 72940T. April 2009.

5. F. Hernandez-Valle, S. Dixon. Preliminary tests to design an EMAT with pulsed electromagnet for high temperature. In: AIP Conference proceedings 1096, Review of Progress in Quantitative Nondestructive Evaluation, Volume 28, pp. 936-941. July 2008.

Nomenclature

A_c	Cross section area
AC	Alternating current
AT	Active thermography
A_1, A_2	Amplitudes of first and second back-wall echoes
B	Magnetic field
B_c	Magnetic field (dynamic)
B_s or B_0	Magnetic field (static)
c_{ijkl}	4^{th} rank elasticity tensor (81 components)
CT	Computed tomography
d	Skin depth or depth of penetration
DC	Direct current
D	Electric displacement
$\bar{D}$	Mean scatterer diameter
e	Electron's charge
E	Electric field
E_z	Electric field at a depth z below the sample surface
E_{z_0}	Electric field at the sample surface
EC	Eddy current
ECT	Eddy current testing
EMAT	Electromagnetic Acoustic Transducer

f	Frequency
F	Lorentz force
FEA	Finite Element Analysis
H	Magnetic field strength
i	$\sqrt{-1}$
I	Total image current
I_c	Alternating current through EMAT coil
j	Current density
j_z	Current density at a depth z below the sample surface
j_{z_0}	Current density at the sample surface
k	Wave number
L	Length
L_{RT}	Sample thickness at room temperature
L_{ThExp}	Sample thickness correction for thermal expansion
m	Electron's mass
M	Magnetization force
M_n	Normal component of the magnetization at the surface
Magnesil	Ferromagnetic material (3% Si, 97% Fe)
MFL	Magnetic flux leakage
MOSFET	Metal-Oxide-Semiconductor Field-Effect Transistor
n_e	Electron density
$\vec{n}$	Unit vector normal to the sample surface
NdFeB	Neodymium-Iron-Boron
NDE	Nondestructive Evaluation
NDT	Nondestructive Testing
Nd:YAG	Neodymium:Yttrium Aluminium Garnet
PE	Pulsed electromagnet

PEC	Pulsed eddy current
PM	Permanent magnet
PT	Penetrant Testing
q	Electric charge
RT	Room temperature
SmCo	Samarium-Cobalt
SNR	Signal-to-Noise Ratio
t	Time
t_1, t_2	Transit times for the first and second back-wall echoes
T	Temperature during ultrasonic measurement
T_c	Curie temperature
T_0	Room temperature
v	Velocity of a charged particle
v_e	Mean electron velocity
v_i	Mean ion velocity
v_l	Longitudinal wave velocity
v_{ph}	Phase velocity
v_s	Shear wave velocity
VARIAC	Variable autotransformer
x, y, z	Cartesian coordinates
W	Width
z	Depth below the sample surface
Z_i	Ion's charge
$\alpha_{dB/mm}$	Attenuation per unit length
α_{Th}	Linear coefficient of thermal expansion
ΔT	Temperature difference (referred to room temperature)
ϵ_0	Permittivity (free space)

ϵ_r	Permittivity (relative)
ε	Strain
ε_{kl}	Strain tensor (Cartesian coordinates)
$\vec{\xi}$	Displacement vector
Γ_{ij}	Christoffel matrix
λ	Wavelength
λ, μ	Lamè parameters
μ_0	Permeability (free space)
μ_r	Permeability (relative)
ρ	Density
ρ_T	Density as a function of the temperature
ρ_{RT}	Density at room temperature
σ	Stress
σ_{ij}	Stress tensor (Cartesian coordinates)
σ	Conductivity
τ	Mean time of the electron-ion collisions
ω	Angular frequency
Blue $\otimes$	Represents a current going into the image plane
Red $\odot$	Represents a current coming out of the image plane
$\cdot$	Scalar product
$\times$	Vector product
∇	Vector differential operator
∇^2	Laplace operator

Abstract

This thesis is concerned with the design and implementation of an Electromagnetic Acoustic Transducer (EMAT) intended for high temperature ultrasonic applications; which benefits from a novel approach using a pulsed current electromagnet (PE) and a ceramic encapsulated spaced spiral coil, both designed to operate at elevated temperatures without any active cooling.
In detail all the steps taken towards the development of the PE-EMAT and its supporting electronics are presented here, together with the finite element simulations performed for the electromagnetic and ultrasonic analysis; which includes: the computation of the flux density produced by the electromagnet and its variation with lift-off (gap between core and metallic sample), the calculation and visualisation of the magnitude of the current density induced by an alternating current flowing in two different EMAT coil designs in non-magnetic and magnetic samples; as well as the validation of the propagation of the ultrasonic wave generated/detected by the PE-EMAT.
The experimental results regarding the performance of the PE-EMAT are also presented. Firstly, the performance at room temperature to show the shear wave generation in paramagnatic and ferromagnetic samples, the effect of the presence of an oxide layer adhered to the sample, and the lift-off performance. Secondly, the performance at a range of different temperatures to demonstrate that the PE-EMAT has been employed successfully at temperatures up to 600 ^{o}C, without using any active cooling system, and that is capable of performing ultrasonic measurements of sample thickness and material properties, without the use of any sort of couplant, nor the necessity of sample preparation.

Chapter 1

Introduction

1.1 Motivation

There are many instances in which components or entire plants operate at elevated temperatures. (e.g. power generation boilers and reactors, pressure vessels, pipelines, condenser tubes, pumps, heat exchangers, valves, etc.). The reliability of these critical components is vital and, precisely for this reason, has attracted the interest of those involved in the asset management process. In fact, some technical issues that arise frequently in this discipline are: how to determine the risk of damage and breakdown failure on the plant components, how to manage the risks meticulously, how to optimise cost of inspection and component replacement, and how to predict material degradation.

Nondestructive testing techniques are commonly used to answer many of these questions, and have proved to be a key tool in specific tasks, such as: corrosion detection and quantification, wall thickness measurements, weld inspections, and flaw detections[1–3]. Nonetheless, most of the inspections currently performed are done at lower or ambient temperatures[4,5], and occasionally sample preparation is required (e.g grinding or sandblasting away oxidised or corroded layers); which usually re-

quires shutting down the plant.

As will be seen in greater detail in the review of techniques for high temperature applications (see Chapter 4), an important trend in condition monitoring at such temperatures is to provide the user with real-time permanent monitoring capabilities[6]. Poor performance of commercial sensors at elevated temperatures is still a significant obstacle in many applications[7], and work is been done to face the challenges imposed by harsh environments using different approaches, such as: piezoelectirc transducers[8–14], electromagnetic acoustic transducers (EMATs)[15–19], laser-based methods[20–24], thermal[25,26] and eddy current techniques[27–29], amongst others.

Evidently, there is significant interest in continuing the progress and improvement of conditioning monitoring systems for high temperature applications, and an increasing demand of such systems that meets industrial requirements make the work described in this thesis particularly timely.

1.2 Nondestructive testing

The goal of any industry is to maximise profits by extending the life of its plant, equipment and final products at the least possible cost. To date, companies have achieved this by implementing different maintenance strategies, e.g. corrective (repairing when something breaks) or preventive (performing scheduled maintenance servicing). Different factors are taken into account in the selection of the appropriate strategy, and depend absolutely on the particular case.

Nondestructive Testing (NDT) techniques have proved to be key elements in addressing maintenance challenges. NDT is an interdisciplinary field which makes use of diverse techniques to determine component integrity and quantitatively measure the characteristics of single components or complete structures. As it is inferred from its name, it deals with assessments without damaging or destroying the ob-

jects under evaluation, and in doing so does not affect its fitness for purpose.

NDT, also known as Nondestructive Evaluation (NDE), is involved in various processes such as: engineering design, maintenance and service. With regard to engineering design, the application of NDT in the early design phase of a component, in combination with a rigorous analysis of material properties and its fatigue characteristics, can extend its life cycle, improve its performance and reduce costs through minimising failures. With respect to maintenance and service, NDT can reduce the frequency of unexpected maintenance and may lengthen the period between scheduled maintenance and prevent unnecessary shutdown, helping in this way to optimise these processes.

NDT is an established yet dynamic research field which is considered to be essential for various industrial environments. Numerous advances in the development of this field have been observed in the last few decades. There is not, and will probably never be, a technique that suits all environments and varieties of specimens; depending on the case in question, all NDT techniques will have some advantages and disadvantages. A review of the established techniques is presented in the following section.

1.3 Review of established techniques

There are several different techniques used in Nondestructive Testing. What follows is a brief description of the methods and techniques most commonly used, together with details of typical applications, advantages and disadvantages. The methods covered are: visual and optical inspection, penetrant testing, radiography, magnetic field methods, eddy current, thermographic testing and ultrasonic methods.

1.3.1 Visual and Optical inspections

Probably the oldest nondestructive test is visual inspection, but specific training and verification of the personnel are still required to provide a degree of confidence[30] and ensure a consistent standard of inspection. This method is the obvious choice if simple and direct examination is needed and gross abnormalities are expected. Therefore, speed and simplicity are its main advantages. On the other hand, the main disadvantages are that the result is valid only for surface conditions and the surface may require some preparation (e.g. cleaning, removing paint, sand-blasting). Even then, direct visual inspection on its own will not pick up all surface defects.

Regarding optical inspections, various techniques are applied for measuring flaws in components and determining stress conditions, for instance: holographic and speckle interferometry[31], and more recently, shearography[32] and digital shearography[33]. A helpful and crucial advantage of interferometric methods is its potential to examine an object at two different times and under possibly different conditions. The utility of these methods in NDT lies in the fact that the regenerated image can be used like a three-dimensional template against which any deviations in shape or dimensions of the object under study can be measured. Since lasers are an essential part of any interferometric technique, care must be taken to comply with safety requirements.

A detailed discussion on theories and applications of these techniques, together with reviews of the most prominent applications can be found in[34–38].

1.3.2 Penetrant testing

Penetrant testing (PT) is a well established NDT method that allows the inspection of a wide range of materials for discontinuities that are open to the surface.

PT methods make use of a contrasting colour material (e.g. fluorescent and dye penetrants) that seeps into a surface discontinuity to reveal its outline. In order to achieve good inspection results when PT methods are applied, a detailed visual examination of the surface to be tested should be conducted prior to any NDT. Strict procedures and specifications related to the materials being tested must be followed, and special cleaning of the specimen must be carried out. The main advantages for PT methods are: easy to apply, inexpensive, rapid, portable, and yields flaw location, orientation, approximate size and shape. On the other hand, its disadvantages are: poor on hot, dirty or rough surfaces, poor on porous materials, removal of paint or other protective coatings from the sample is needed, environmental and safety concerns are still important, and highly operator-dependent. More details about some important applications, advantages and limitations for this technique can be found elsewhere[39–41,30,42].

1.3.3 Radiography

Radiographic techniques have been in use for decades in a wide range of applications for NDT. Defects such as cracks, voids, and missing constituents during the manufacturing process are detectable with this sort of inspection. In subsequent sections three of the most common methods are presented and treated separately because of their source of radiation: X-ray, gamma-ray, and neutron radiation.

X-ray radiography

X-rays can be used to yield data in one-dimension (gauge measurement), two-dimensions (radiograph), or three-dimensions (computed tomography). Probably the most widely employed imaging method in NDT is the two-dimensional radiography, especially because it is applicable to finding voids, inclusions and open cracks. However, the advent of computers made it possible to acquire a large number

of radiographs at different angular orientations to the object, and made computed tomography (CT) systems a very serious competitor, particularly where information is needed in three spatial dimensions. One of the numerous advantages of using X-rays is that complex shapes can be readily assessed, it is suitable for sensing changes in elemental composition (mass, volume density or thickness), and although analysing and interpreting requires certain skills, expert interpretation is not always needed. Disadvantages include the following: serious safety concerns (not only is the radiation dangerous, but the high voltage needed to generate X-rays can also be dangerous), access to opposite sides of the test object is required, closed cracks are not detectable and flaws must be oriented nearly parallel to the direction of radiation travel. Finally, X-rays machines, especially CT systems, are very expensive and measurements can be time consuming depending on the computational capabilities to process a large number of images. More details about the basic theory, general equipment and procedures can be found in [43–46].

Gamma-ray radiography

Gamma-rays differ from X-rays in their penetrating power and their source. While X-rays are generated electrically, gamma-rays are produced by radioactive decay of unstable atomic nuclei; consequently there is a continuous reduction in the intensity of emitted radiation with time. Thus, the selection of a radioisotope for specific tasks is very important and is based primarily on the radiation energy, the source size, and the output. Since a very limited number of radioisotopes have the required properties (Iridium 192, Cesium 137 or Cobalt 60, amongst others), there is much less diversity in applications than for X-rays. However, when compared with X-ray sources for NDT, gamma-ray sources have the advantages of compactness, freedom from electrical power supplies, transportability and penetrating power. Regarding the latter, Cobalt 60 emits gamma-rays at 1.17 and 1.33 MeV, which may

appear to be comparable to the output of a 1-MV X-ray unit, however this is not correct, in fact a 2-MV X-ray unit would be required to generate X-rays having penetrating power equal to that of Cobalt 60[30]. There are also disadvantages, and these include: constant decay of the radioisotope, cost of replenishment when the dose rate falls below practical levels, special safety considerations due to the constant emission of radiation, and licensing and personnel training requirements. More information about the basic concepts, penetration capabilities and of recent applications of gamma rays for NDT can be found in[47–49].

Neutron radiography

Neutron radiography assesses the physical integrity of selected materials in a similar fashion to X-ray radiography. The effectiveness of both depends on the relative attenuation of the incident radiation intensity in the material under study. However, while the attenuation of X-rays increases with the atomic number, with neutrons the attenuation has a more complicated relationship with it[30].

Neutron radiography complements conventional X-ray radiography by having the capability of detecting flaws that cannot be effectively assessed with X-rays. The unique capability of neutrons is due to the fact that they do not interact with orbiting electrons in the atoms of materials being tested; which means that for heavy elements such as lead or iron, which strongly absorb X-rays, these elements offer little resistance to the passage of neutrons. Conversely, light elements such as hygrogen or lithium, which strongly absorb neutrons, let X-rays to pass through relatively easy. Disadvantages for neutron radiography include the fact that practical neutron sources are expensive, shielding materials are large and heavy, more complex film exposure procedures are required for this method than for X-ray radiography, and caution must be exercised at all times to protect personnel from radiation. More information regarding different neutron sources, equipment and recent applications

for NDT can be found in[44,50–53].

1.3.4 Magnetic field measurement methods

In magnetic flux leakage (MFL) for NDT purposes a sample is magnetized using either a permanent magnet, an electromagnet or an electrical current through a conductor. The surface is then scanned for magnetic leakage fields; which are magnetic field perturbations produced by nonmagnetic flaws, such as cracks or lack of material. A number of magnetic flux sensors can be used (e.g coils, C-core yokes, or solid state magnetic sensors). MFL methods are ideally suited for detection of surface cracks and near-surface inclusions in ferromagnetic materials, and for measurements of wall thinning in pipelines. Advantages of this method are: no contact with the sample is required, no specific surface preparation is needed, automatization can be accomplished, and sensitivity is limited by ambient noise and background magnetic fields. The greatest disadvantage of MFL is that it can be used only on ferromagnetic parts and magnetically permeable materials, only surface and near-surface defects can be detected, and access to the test surface is required. More details about these methods, including basic magnetism for NDT and detailed information about their applications can be seen in[54–57].

1.3.5 Eddy current testing

Eddy current (EC) technology measures the response of materials to electromagnetic fields over a specific frequency range (typically from few kHz to several MHz). From this response, material conditions such as thickness, presence of corrosion, hardness or defects (porosity and cracks) can be revealed. Primarily, EC probes inspect electrically conductive materials, although some low-conductivity materials such as graphite-epoxy composites can also be examined. Some advantages of this technique are: it can be automated and high-speed inspection is possible due to

its noncontacting approach, tests can be made inexpensively, surface preparation is often not required, inspection depth can be controlled by adjusting the current frequency, and finally this is one of the few methods used successfully for high temperature applications. This inspection method suffers from a number of drawbacks, which include: only surface or near surface flaws can be detected (depth of penetration is limited), sensitivity to lift-off variations and operator training is needed to correctly interpret results.

More recently, significant progress regarding pulsed eddy current (PEC) probes has been made. The basic advantages over conventional probes are, first, that the circuitry is relatively simple compared with that needed for broadband alternating current testing and, second, that a single transient response contains as much information as an entire spectrum of frequency domain excitations. However, data analysis is still a challenge and new methods to extract dominant features from PEC probe responses are being developed.

A detailed examination regarding basic concepts on generation and detection of EC and PEC probes, together with equipment requirements, can be found in [54,58–62].

1.3.6 Thermal testing

There are a number of different variants of thermal testing methods for NDT (active termography, photothermal radiometry, photoacoustic spectroscopy, amongst others). Common to all thermal inspection methods is the use of heat-sensing devices or substances to measure the resulting thermal gradients or atypical temperatures in samples when they are heated or cooled. One of the most widely used thermal technique in NDT is active thermography (AT), which integrates infrared imaging with external heating to assess subsurface structure. This technique focuses on the detection of defects such as voids, cracks, and delaminations in composites which are all very readily detected, using the variation in thermal properties

between the defect and the object under study. Amongst the strengths of AT are: its noncontact capability, its ability to perform measurements covering large areas (with large stand-offs if needed), and that the material property being tested (its thermal behaviour) is quite unique and different from the properties probed in other NDT methods. Amongst the weaknesses of AT are: frequent calibration may be required, sensitivity can be affected by reflected or background radiation, and initial cost of sensors and associated instrumentation is relatively high.

A detailed discussion about some of the most important applications for this technique can be found in [63–65].

1.3.7 Ultrasonic methods

Ultrasonic inspection consists of the generation, propagation and detection of sound waves through a material (typically $>$ 20kHz), to measure either or both the time of travel (velocity) and any change of intensity (attenuation) for a given propagation distance. Using these features in ultrasonic waves, the elastic constants (Young's modulus and Poisson's ratio, etc.), density, and geometry of a material can be determined. In addition, the position, size, and shape of a flaw can be resolved. Some advantages of ultrasonic methods are that they can be used for all types of materials including biological, metals, and ceramics. They offer contacting as well as noncontacting approaches, and only single-surface accessibility is required. Both internal and surface defects can be detected, and flaw imaging is possible. Conversely, disadvantages are: there can be difficulty in coupling to rough surfaces when contacting transducers are used, sensitivity is limited by the utilized frequency, special scanning systems may be required for inspecting large surfaces, and significant operator training is needed.

More information about the properties of ultrasonic waves can be found in chapter 2. Their applications in NDT are covered in greater depth in chapters 3 and 4,

where information regarding EMATs and piezoelectric transducers can be found. Additional details about ultrasonic methods can be found as well in other references[44,66–69].

1.4 Thesis outline

Chapter 2 gives an overview of basic ultrasonic theory on aspects relevant to this study, such as: introduction to wave propagation in solid media, shear and longitudinal bulk waves, different mechanisms that have an impact on the amplitude of the wave as it travels through the medium (absorption, scattering, geometric attenuation, and dispersion); as well as particular observations regarding the effect of rise in temperature. Additionally, this chapter also includes a section that describes the finite element simulations performed in commercial software packages (Comsol Multiphysics and PZFlex) to verify and/or improve comprehension of the experimental results obtained in this project.

Chapter 3 portrays a review of the operation principles of Electromagnetic Acoustic Transducers (EMATs). Also includes details on the electromagnetic coupling (image current generation and the skin effect), and generation mechanisms (Lorentz force and Magneto-elastic), and a specific section in which is demonstrated that EMATs are in actual fact velocity sensors. In addition, this chapter describes that wave modes excited by means of EMATs depend mainly on the geometrical configuration of its coil and the orientation of the bias magnetic field, thus a description of typical designs is included.

Chapter 4 presents a review of progress of the most representative transducers employed in high temperature applications, such as: piezoelectric transducers, EMATs, lasers, laser-EMAT combinations, thermal techniques and eddy current probes. In each case, a description on the advantages and disadvantages, as well as on their

limitations is included.

Chapter 5 deals with the steps taken towards the development of the pulsed electromagnet (PE)-EMAT and the supporting electronics designed specifically to meet the requirements of the system at room temperature. In particular, this chapter describes its operation and the optimisation process followed to obtain the maximum ultrasonic signal. Also, this chapter presents the results from the flux density produced by the electromagnet and the ultrasonic measurements, both carried out at room temperature in two different samples (aluminium and low carbon steel), as well as the results from the finite element simulations performed in Comsol and PZFlex.

Chapter 6 describes the steps taken to transform the PE-EMAT described in the previous chapter, into a transducer capable of withstanding elevated temperatures without the use of any active cooling. Additionally, this chapter presents the results of the measurements performed at elevated temperatures when the PE-EMAT is operating on low carbon steel. This includes the temperature dependence of: shear waves velocity, mass density, and attenuation.

Finally, *Chapter 7* presents the conclusions and highlights the main findings that arise as a result of the work presented in this thesis. In addition, the last part of this chapter is concerned to the research directions to follow from the findings of this work.

References

[1] T. Stubbs. The role of NDE in the life management of steam turbine rotors. *Insight*, 46(9):529–532, 2004.

[2] R.J. Ditchburn, S.K. Burke, and C.M. Scala. NDT of welds: State of the art. *NDT&E International*, 29(2):111–117, 1996.

[3] S.D. Kenny, K. Stamps, and P. Crowther. Development of NDT techniques and inspection for detection and sizing of thermal fatigue cracking in steam-pipework bores of flexibly operated coal-fired power stations. *Insight*, 45(2): 125–126, 2003.

[4] S. Baby, T. Balasubramanian, and R.J. Pardikar. Ultrasonic study for flaw detectability in ferritic butt welds at high temperatures. *Insight*, 45(1):87–91, 2003.

[5] S. Gongtian and T. Li. Infrared thermography for high-temperature pressure pipe. *Insight*, 49(3):151–153, 2007.

[6] K. J. Kirk, J. Elgoyhen, J.P. Hood, D. Hutson, R.S. Dwyer-Joyce, J. Zhang, and B.W. Drinkwater. Ultrasonic condition monitoring using thin-film piezoelectric sensors. *Insight*, 52(4):184–187, 2010.

[7] R. Kazys, A. Voleisis, and B. Voleisiene. High temperature ultrasonic transducers: review. *Ultragarsas*, 63(2):7–17, 2008.

[8] T. Arakawa, M. Tanosaki, and K. Yoshikawa. On-line monitoring techniques of crack propagation using brazed-type ultrasonic sensors for high temperature use. In *NDE in the nuclear and pressure vessel industries*, pages 217–221, 1995.

[9] C.-K Jen, B. Cao, K.T. Nguyen, C.A. Loong, and J.-G. Legoux. On-line ultrasonic monitoring of a die-casting process using buffer rods. *Ultrasonics*, 35(5): 335–344, 1997.

[10] A. McNab, K.J. Kirk, and A. Cochran. Ultrasonic transducers for high temperature applications. In *IEE Proceedings-Science, Measurement & Technology*, volume 145, pages 229–236, 1998.

[11] M. Kobayashi, T. R. Olding, M. Sayer, and C. K. Jen. Piezoelectric thick film ultrasonic transducers fabricated by a sol-gel spray technique. *Ultrasonics*, 39 (10):675–680, 2002.

[12] K.J. Kirk, C.K. Lee, and S. Cochran. Ultrasonic thin film transducers for high-temperature NDT. *Insight*, 47(2):85–87, 2005.

[13] I. Atkinson, C. Gregory, S.P. Kelly, and K.J. Kirk. Ultrasmart: Developments in ultrasonic flaw detection and monitoring for high temperature plant applications. In *Proceedings of CREEP8*, pages 1–13, 2007.

[14] F.B. Cegla and J.O. Davies. Ultrasonic crack monitoring at high temperatures using sh waves. In D.O. Thompson and D.E. Chimenti, editors, *Review of progress in Quantitative Nondestructive Evaluation Vol. 29*, pages 980–987, 2010.

[15] S. Dixon, C. Edwards, J. Reed, and S.B. Palmer. Using EMATs to measure the wall thickness of hot galvanizing kettles. *Insight*, 37(5):368–370, 1995.

[16] A. Idris. *Non-contact ultrasonic study on thixotropic alloys.* PhD thesis, University of Warwick, 1995.

[17] Md.S. Rohani. *The development of non-contact laser and EMAT ultrasound measurement systems for hot steel.* PhD thesis, University of Warwick, 1996.

[18] I. Baillie, P. Griffith, X. Jian, and S. Dixon. Implementing an ultrasonic inspection system to find surface and internal defects in hot, moving steel using EMATs. *Insight*, 49(2):87–92, 2007.

[19] I. Baillie. *The development of a laser-EMAT system suitable for on-line inspection in the continuous casting plant-Innovation report.* PhD thesis, University of Warwick, 2008.

[20] R.J. Dewhurst, C. Edwards, A.D.W. McKie, and S.B. Palmer. A remote laser system for ultrasonic velocity measurement at high temperatures. *Journal of Applied Physics*, 63(4):1225–1227, 1988.

[21] C.B. Scruby and B.C. Moss. Non-contact ultrasonic measurements on steel at elevated temperatures. *NDT&E International*, 26(4):177–188, 1993.

[22] A. Cand, J.P. Monchalin, and X. Jia. Detection of in-plane and out-of-plane ultrasonic displacements by a 2-channel confocal Fabry-Perot interferometer. *Applied Physics Letters*, 64(4):414–416, 1994.

[23] B. Hutchinson, B. Moss, A. Smith, A. Astill, C. Scruby, G. Engberg, and J. Bjorklund. Online characterisation of steel structures in hot strip mill using laser ultrasonic measurements. *Ironmaking & steelmaking*, 29(1):77–80, 2002.

[24] D. Lvesque, S.E. Kruger, G. Lamouche, R. Kolarik II, G. Jeskey, M. Choquet, and J.-P. Monchalin. Thickness and grain size monitoring in seamless tube-

making process using laser ultrasonics. *NDT&E International*, 39(8):622 – 626, 2006.

[25] X. Maldague. Pipe inspection by infrared thermography. *Materials Evaluation*, 57(9):899–902, 1999.

[26] G. Shen and T. Liebeaux. Infrared thermography for high-temperature pressure pipe. *Insight*, 49(3):151–153, 2007.

[27] J. Hansen. The eddy current inspection method - Part 4. Applications, practical testing and advanced concepts. *Insight*, 46(8):480–483, 2004.

[28] T. Kasuya, T. Okuyama, N. Sakurai, H. Huang, T. Uchimoto, T. Takagi, Y. Lu, and T. Shoji. In-situ eddy current monitoring under high temperature environment. *International Journal of Applied Electromagnetics and Mechanics*, 20: 163–170, 2004.

[29] R. Urayama, T. Uchimoto, and T. Takagi. Application of EMAT/EC dual probe to monitoring of wall thinning in high temperature environment. *International Journal of Applied Electromagnetics and Mechanics*, 33(3-4):1317–1327, 2010.

[30] D.E. Bray and D. McBride. *Nondestructive testing techniques*. New dimensions in engineering. John Wiley & Sons, Inc., 1992.

[31] R. Ambu, F. Aymerich, F. Ginesu, and P. Priolo. Assessment of ndt interferometric techniques for impact damage detection in composite laminates. *Composites Science and Technology*, 66(2):199–205, 2006.

[32] Y.Y. Hung and H.P. Ho. Shearography: An optical measurement technique and applications. *Materials Science and Engineering: R: Reports*, 49(3):61–87, 2005.

[33] V.R. Singh, J. Miao, Z. Wang, G. Hedge, and A. Asundi. Dynamic characterization of MEMS diaphragm using time averaged in-line digital holography. *Optics communications*, 280:285–290, 2007.

[34] H. Shang and J. Gao. Theories and industrial applications of optical interferometric NDT techniques: A review. *Insight*, 51(5):240–251, 2009.

[35] L. Bruno and A. Poggialini. Back to the future: From speckle to holography. *Optics and lasers in engineering*, 45(5):538–549, 2007.

[36] T. Kreis. *Handbook of holographic interferometry. Optical and digital methods.* Wiley-VCH, 2005.

[37] R. Jones and C. Wykes. *Holographic and speckle interferometry: a discussion of the theory, practice and application of the techniques.* Cambridge University Press, 1989.

[38] Y.Y. Hung and C.Y. Liang. Image-shearing camera for direct measurement of surface strains. *Applied Optics*, 18(7):1046–1051, 1979.

[39] S.J. Robinson, R. Goff, and A.G. Sherwin. Water based penetrants: Advantages and limitations. *Materials Evaluation*, 57(9):893–897, 1999.

[40] P. Hessinger and M.L. White. Treatment alternatives for liquid penetrant rinse waters. *Materials Evaluation*, 56(8):969–970, 1998.

[41] P.P. Prokhorenko, A.M. Sekerin, and A.P. Klornev. A quantitative estimation of penetrant systems. *Nondestructive Testing and Evaluation*, 13(6):325–345, 1997.

[42] A. Sherwin. Still a good rule - Visible penetrant inspection not to precede fluorescent. *Materials Evaluation*, 48(12):1456–1457, 1990.

[43] T. Matsumoto and H. Mimura. Point x-ray source using graphite nanofibers and its application to x-ray radiography. *Applied Physics Letters*, 82(10):1637–1639, 2003.

[44] P.J. Shull. *Nondestructive evaluation. Theory, techniques and applications.* CRC Press, 2002.

[45] P. Cloetens, M. Pateyron-Salome, J.Y. Buffiere, G. Peix, J. Baruchel, F. Peyrin, and M. Schlenker. Observation of microstructure and damage in materials by phase sensitive radiography and tomography. *Journal of Applied Physics*, 81 (9):5878–5886, 1997.

[46] G. Harding and J. Kosanetzky. Scattered X-ray beam nondestructive testing. *Nuclear Instruments and Methods in Physics Research Section A: Accelerators, Spectrometers, Detectors and Associated Equipment*, 280(2-3):517–528, 1989.

[47] M.S. Rapaport and A. Gayer. Application of gamma ray computed tomography to nondestructive testing. *NDT&E International*, 24(3):141–144, 1991.

[48] R. Halmshaw. BS-EN-444-1994-Nondestructive testing. General-Principles for radiographic examination of metallic materials by x-rays and gamma-rays. *Insight*, 36(8):618–619, 1994.

[49] C. Dragnea. The use of selenium-75 gamma-rays for the radiography of polyethylene materials used for natural gas and water distribution. *Insight*, 43(6):418–420, 2001.

[50] J.S. Brenizer, B. Hosticka, H. Berger, and G.T. Gillies. The use of contrast agents to enhance crack detection via neutron radiography. *NDT&E International*, 32(1):37–42, 1999.

[51] S. Casalta, G.G. Daquino, L. Metten, J. Oudaert, and A. Van de Sande. Digital image analysis of X-ray and neutron radiography for the inspection and the monitoring of nuclear materials. *NDT&E International*, 36(5):349–355, 2003.

[52] H. Berger. Advances in neutron radiographic techniques and applications: a method for nondestructive testing. *Applied Radiation and Isotopes*, 61(4):437–442, 2004.

[53] M. Michaloudaki, E. Lehmann, and D. Kosteas. Neutron imaging as a tool for the non-destructive evaluation of adhesive joints in aluminium. *International Journal of Adhesion and Adhesives*, 25(3):257–267, 2005.

[54] D.E. Bray and R.K. Stanley. *Nondestructive Evaluation: a tool in design, manufacturing, and service*. CRC Press, 1997.

[55] J. Blitz. *Electrical and magnetic methods of non-destructive testing*. Chapman & Hall, 1997.

[56] D. Lovejoy. *Magnetic particle inspection. A practical guide*. Kluwer Academic Publishers, 1993.

[57] D. Jiles. *Introduction to magnetism and magnetic materials*. Chapman & Hall, 1991.

[58] T. Chen, G.Y. Tian, A. Sophian, and P.W Que. Feature extraction and selection for defect classification of pulsed eddy current NDT. *NDT&E International*, 41 (6):467–476, 2008.

[59] A. Sophian, G.Y. Tian, D. Taylor, and J. Rudlin. A feature extraction technique based on principal component analysis for pulsed Eddy current NDT. *NDT&E International*, 36(1):37–41, 2003.

[60] J.R Bowler and M. Johnson. Pulsed eddy-current response to a conducting half-space. *IEEE Transactions on magnetics*, 33(3):2258–2264, 1997.

[61] S.J. Norton and J.R. Bowler. Theory of eddy current inversion. *Journal of Applied Physics*, 73(2):501–512, 1993.

[62] J.R. Bowler. Eddy current calculations using half-space Green's functions. *Journal of Applied Physics*, 61(3):833–839, 1987.

[63] N.P. Avdelidis and D.P. Almond. Through skin sensing assessment of aircraft structures using pulsed thermography. *NDT&E International*, 37(5):353–359, 2004.

[64] D.J. Titman. Applications of thermography in non-destructive testing of structures. *NDT&E International*, 34(2):1479–154, 2001.

[65] A. Moropoulou, M. Koui, and N.P. Avdelidis. Infrared thermography as an NDT tool in the evaluation of materials and techniques for the protection of historic monuments. *Insight*, 42(6):379–383, 2000.

[66] B.A. Auld. *Acoustic fields and waves in solids. Vol. 1.* Krieger publishing Co., 1990.

[67] J. Krautkramer and H. Krautkramer. *Ultrasonic testing of materials.* Springer-Verlag, 4th edition, 1990.

[68] J. D. Achenbach. Quantitative nondestructive evaluation. *International Journal of Solids and Structures*, 37(1-2):13–27, 2000.

[69] J.L. Rose. *Ultrasonic waves in solid media.* Cambridge University Press, 1st edition, 1999.

Chapter 2

Basic theory and review

The study and application of ultrasound (acoustic waves propagating at frequencies above $\approx$ 20 kHz) is known as ultrasonics, and describes the phenomenon of time-varying deformations or vibrations in solid, liquid or gaseous media[1–4]. To formulate a mathematical description of these vibrations it is necessary to relate the material deformation and the internal restoring forces that lead to those oscillatory motions. In the case of elastic solids[5–7], this formulation is given by the relationship between stress (σ) and strain (ε) in the sample, and using rectangular Cartesian coordinates (x, y, z axes), these conditions can be represented in the form of tensors as:

$$\sigma_{ij} = \begin{pmatrix} \sigma_{xx} & \sigma_{xy} & \sigma_{xz} \\ \sigma_{yx} & \sigma_{yy} & \sigma_{yz} \\ \sigma_{zx} & \sigma_{zy} & \sigma_{zz} \end{pmatrix} \tag{2.1}$$

$$\varepsilon_{ij} = \begin{pmatrix} \varepsilon_{xx} & \varepsilon_{xy} & \varepsilon_{xz} \\ \varepsilon_{yx} & \varepsilon_{yy} & \varepsilon_{yz} \\ \varepsilon_{zx} & \varepsilon_{zy} & \varepsilon_{zz} \end{pmatrix} \tag{2.2}$$

Since the tensors are symmetric, each component can be specified by one subscript rather than two, and they can be written as a six-element column matrix rather than as a nine-element matrix[8]. That is:

$$\sigma = \begin{pmatrix} \sigma_1 & \frac{1}{2}\sigma_6 & \frac{1}{2}\sigma_5 \\ \frac{1}{2}\sigma_6 & \sigma_2 & \frac{1}{2}\sigma_4 \\ \frac{1}{2}\sigma_5 & \frac{1}{2}\sigma_4 & \sigma_3 \end{pmatrix} = \begin{pmatrix} \sigma_1 \\ \sigma_2 \\ \sigma_3 \\ \sigma_4 \\ \sigma_5 \\ \sigma_6 \end{pmatrix} \tag{2.3}$$

$$\varepsilon = \begin{pmatrix} \varepsilon_1 & \frac{1}{2}\varepsilon_6 & \frac{1}{2}\varepsilon_5 \\ \frac{1}{2}\varepsilon_6 & \varepsilon_2 & \frac{1}{2}\varepsilon_4 \\ \frac{1}{2}\varepsilon_5 & \frac{1}{2}\varepsilon_4 & \varepsilon_3 \end{pmatrix} = \begin{pmatrix} \varepsilon_1 \\ \varepsilon_2 \\ \varepsilon_3 \\ \varepsilon_4 \\ \varepsilon_5 \\ \varepsilon_6 \end{pmatrix} \tag{2.4}$$

For small deformations (or within the linear elastic limit) it is an experimentally observed fact that the strain in a deformed body is linearly proportional to the applied stress (Hookes's law)[9], which can be stated as:

$$\sigma_{ij} = c_{ijkl}\varepsilon_{kl} \tag{2.5}$$

Where c_{ijkl} is a 4^{th} rank elasticity tensor with 81 components; which in case the stress symmetry condition is satisfied it can be reduced from 81 to 36 (2^{nd} rank

tensor), as it is shown in this equation:

$$\begin{pmatrix} \sigma_1 \\ \sigma_2 \\ \sigma_3 \\ \sigma_4 \\ \sigma_5 \\ \sigma_6 \end{pmatrix} = \begin{pmatrix} c_{11} & c_{12} & c_{13} & c_{14} & c_{15} & c_{16} \\ c_{21} & c_{22} & c_{23} & c_{24} & c_{25} & c_{26} \\ c_{31} & c_{32} & c_{33} & c_{34} & c_{35} & c_{36} \\ c_{41} & c_{42} & c_{43} & c_{44} & c_{45} & c_{46} \\ c_{51} & c_{52} & c_{53} & c_{54} & c_{55} & c_{56} \\ c_{61} & c_{62} & c_{63} & c_{64} & c_{65} & c_{66} \end{pmatrix} \cdot \begin{pmatrix} \varepsilon_1 \\ \varepsilon_2 \\ \varepsilon_3 \\ \varepsilon_4 \\ \varepsilon_5 \\ \varepsilon_6 \end{pmatrix} \tag{2.6}$$

The number of independent elastic stiffness constants needed to describe a body varies depending on its particular structure, thus for particular cases certain constants in the matrix can be null, or equal in magnitude.

Since the materials of interest for this project can be seen as isotropic, and provided that the general elastic isotropy condition is met ($c_{12} = c_{11} - 2c_{44}$), then it is possible to show that the stiffness matrix for this sort of medium can be reduced to[8]:

$$\begin{pmatrix} c_{11} & c_{12} & c_{12} & 0 & 0 & 0 \\ c_{12} & c_{11} & c_{12} & 0 & 0 & 0 \\ c_{12} & c_{12} & c_{11} & 0 & 0 & 0 \\ 0 & 0 & 0 & c_{44} & 0 & 0 \\ 0 & 0 & 0 & 0 & c_{44} & 0 \\ 0 & 0 & 0 & 0 & 0 & c_{44} \end{pmatrix} \tag{2.7}$$

Thus, it can be said that an isotropic medium has only two independent elastic constants; which are often taken to be the Lamè parameters (λ and μ), and are defined by:

$$\lambda = c_{12} \quad \text{and} \quad \mu = c_{44} \tag{2.8}$$

As will be seen in section 2.2, another useful relationship is to use the Lamè parameters into the general isotropy condition, as follows:

$$c_{11} = \lambda + 2\mu \tag{2.9}$$

2.1 Ultrasonic wave propagation

The propagation of a uniform plane wave in a freely vibrating medium (body force field is zero), can be described using the Christoffel equation [8]:

$$k^2 \Gamma_{ij} v_j - \rho\omega^2 v_i = 0 \tag{2.10}$$

where Γ_{ij} is the Christoffel matrix, k is the wave number, ρ is the density, ω is the angular frequency, and v is the phase velocity. This equation in full tensor form becomes:

$$k^2 \begin{bmatrix} \Gamma_{11} & \Gamma_{21} & \Gamma_{31} \\ \Gamma_{12} & \Gamma_{22} & \Gamma_{32} \\ \Gamma_{13} & \Gamma_{23} & \Gamma_{33} \end{bmatrix} \begin{bmatrix} v_x \\ v_y \\ v_z \end{bmatrix} - \rho\omega^2 \begin{bmatrix} v_x \\ v_y \\ v_z \end{bmatrix} = 0 \tag{2.11}$$

When the stiffness matrix is given by eq. 2.7, then the Christoffel matrix becomes a purely diagonal matrix, transforming the above equation into:

$$k^2 \begin{bmatrix} c_{44} & 0 & 0 \\ 0 & c_{44} & 0 \\ 0 & 0 & c_{11} \end{bmatrix} \begin{bmatrix} v_x \\ v_y \\ v_z \end{bmatrix} - \rho\omega^2 \begin{bmatrix} v_x \\ v_y \\ v_z \end{bmatrix} = 0 \tag{2.12}$$

which will define a wave solution dependent on wave propagation and polarization direction, as will be seen in next section.

2.2 Shear and Longitudinal bulk waves

In solids, both longitudinal (or compressional) and shear (or transverse) bulk waves can propagate through the medium. Longitudinal waves occur when the particle displacement is along the propagation direction of the wave. Whereas shear waves occur when the particle displacement is perpendicular to the propagation direction[10,11]. The particle displacement in shear waves can occur in two independent directions and depending on the orientation the waves can be further classified as polarized horizontally or vertically.

In order to determine the phase velocity for shear and longitudinal waves in an isotropic medium, three independent equations can be derived from eq. 2.12:

$$k^2 c_{44} v_x = \rho\omega^2 v_x,\ k^2 c_{44} v_y = \rho\omega^2 v_y, \quad \text{and} \quad k^2 c_{11} v_z = \rho\omega^2 v_z \tag{2.13}$$

According to these equations, the x-polarized (z-propagating) and y-polarized (z-propagating) shear wave solutions, must both satisfy:

$$k^2 c_{44} = \rho\omega^2 \tag{2.14}$$

Meanwhile, the longitudinal wave solution must satisfy:

$$k^2 c_{11} = \rho\omega^2 \tag{2.15}$$

Therefore, the phase velocity ($v = \omega/k$) being independent of direction for this sort of medium, has two values:

$$v_s = \sqrt{\frac{c_{44}}{\rho}} \tag{2.16}$$

for the two shear waves, and

$$v_l = \sqrt{\frac{c_{11}}{\rho}} \tag{2.17}$$

for the longitudinal wave.

Alternatively, these equations can also be expressed in terms of the Lamè parameters (see eqs. 2.8 and 2.9), as:

$$v_l = \sqrt{\frac{\lambda + 2\mu}{\rho}} \quad \text{and} \quad v_s = \sqrt{\frac{\mu}{\rho}} \tag{2.18}$$

2.3 Amplitude reduction of ultrasonic waves in solids

Ultrasound waves propagating in solids decrease in amplitude as they travel through the medium. Basically, this results from different mechanisms: absorption, scattering, geometric attenuation and dispersion[12–14]. A brief explanation of each mechanism is presented below.

Absorption is a direct conversion of sound energy into heat, for which several processes can be responsible. In general terms, absorption can be visualised as sort of damping effect on the particle oscillations. Absorption increases linearly with frequency, which explains why a rapid oscillation loses more energy than a slow oscillation.

Scattering results from the inhomogeneities in the material (e.g. porosity, grain boundaries, inclusions and phase changes in metals). When a wave encounters these material variations, it will reflect, refract, or mode-convert according to the angle of incidence, the change in density, and the change in elastic properties. The amount of energy that is scattered depends on the ratio between the mean scatterer diameter ($\bar{D}$) and the wavelength (λ) of the ultrasonic wave, and is classified in three different regimes: Rayleigh, stochastic, and diffusive[15,16]. In the Rayleigh regime, $\bar{D}$ is very

small when compared to λ and the attenuation coefficient is proportional to the fourth power of the frequency ($\bar{D}^3 f^4$). In the second regime (stochastic), where λ is approximately of the same order of magnitude than $\bar{D}$, the attenuation coefficient varies with the square of the frequency ($\bar{D} f^2$). Finally, in the third regime (diffusive), where λ is small in comparison to $\bar{D}$, the attenuation coefficient is independent of the frequency but varies with the inverse of the mean scatterer diameter ($1/\bar{D}$).

Geometric attenuation appears because of the fact that a true plane wave cannot exist, it must either diverge or converge, and as it does so the wave amplitude will geometrically attenuate or amplify. In this case, energy is redistributed over a different area but remains part of a single wave.

Dispersion refers to frequency-dependent effects in wave propagation. As seen in section 2.2, the phase velocity of a wave is defined as $v = \omega/k$, when ω is directly proportional to k then the group velocity ($\frac{d\omega}{dk}$) is equal to v. The group velocity is associated with the propagation velocity of a group of waves of different frequency, with a certain modulation envelope. Thus, when the proportionality is different to the aforementioned condition, the modulation envelope will become distorted.

2.4 Effect of rise in temperature in solids

Increasing the temperature in a solid medium produces an increment in the average inter-atomic separation (thermal expansion); which in turn affect its density and elastic constants. The density of a solid medium as a function of the temperature, can be given by [19]:

$$\rho_T = \frac{\rho_{RT}}{1 + 3\alpha_{Th}\Delta T} \tag{2.19}$$

where ρ_{RT} is the density at room temperature (20 °C), α_{Th} is the linear coefficient of thermal expansion and ΔT is the difference in temperature referred to room

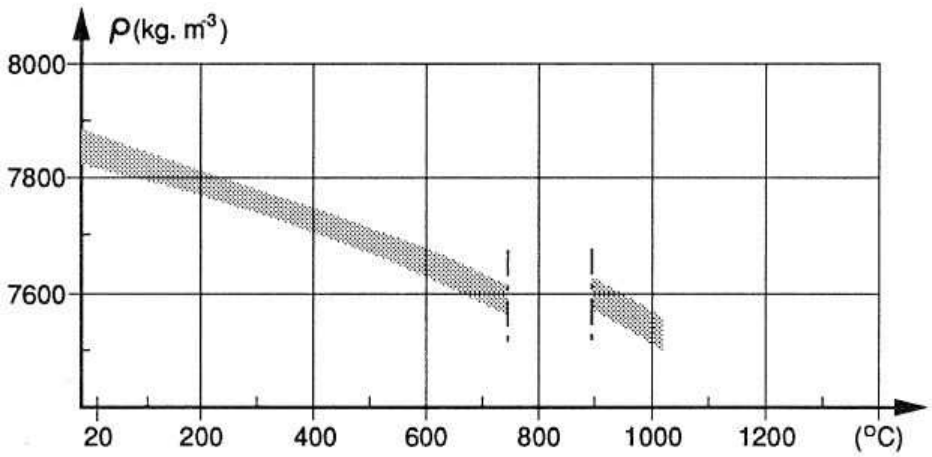

(a)

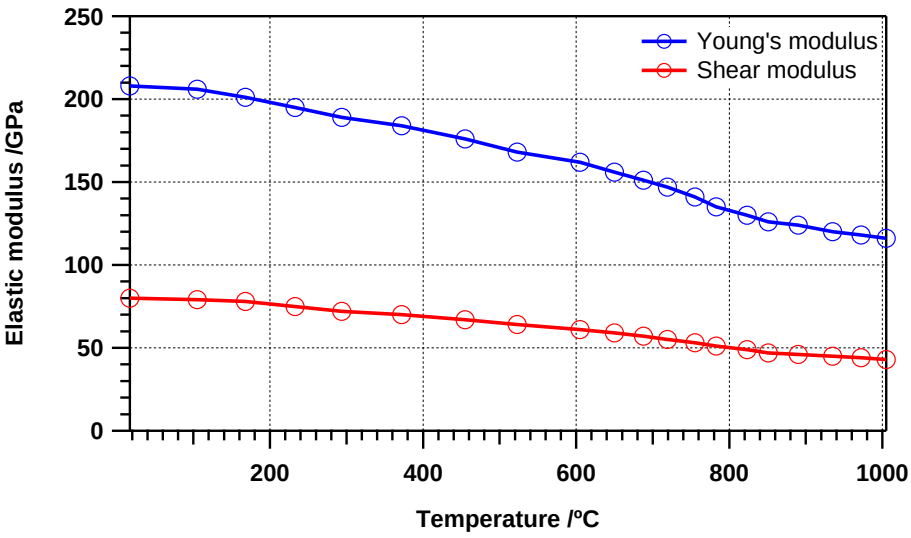

(b)

Figure 2.1: Effect of rise in temperature as a function of temperature in mild steel for: (a) Density (Original diagram appears in [17]); and (b) Shear and Young's modulus (Original diagram appears in [18]).

temperature. For the temperature range between room temperature and 1000 °C, a density change of approximately 3% is expected[17], and can be seen in figure 2.1(a). Experiments to measure the shear and Young's modulus variations for a similar range of temperature in mild steel[18,20], have shown that these quantities are expected to reduce by ≈39 % and ≈44 %, respectively, as can be seen in figure 2.1(b).

In addition, at higher temperatures the average sample grain size may increase; which will cause a change in the nature of ultrasound propagation (i.e. velocity and attenuation). Attenuation in conditions of rising temperatures is found to increase rapidly in the vicinity of the Curie temperature (T_c), where a transition from ferromagnetic to paramagnetic phase occurs. The phase transition is also associated with the rapid reduction in ultrasound velocity at T_c, for iron and steels[18].

The aforementioned changes as the temperature is raised impose different challenges. Evidently, a comprehensive study of the precision with which ultrasonic velocities and hence elastic constants can be measured is paramount in material property determination for high temperature applications.

2.5 Finite Element Analysis

Considerable research efforts have been devoted to study the underlying physical principles in the transduction mechanisms of Electromagnetic Acoustic Transducers (EMATs) for a wide variety of configurations and applications; which includes numerical simulation and finite element analysis of electromagnetic and ultrasonic phenomena[21–29] (e.g. eddy current induction, and generation-propagation-interaction of ultrasonic wave). Commercial software packages, such as Comsol Multiphysics and PZFlex, have been used for this purpose, and in the present body of work these packages were used to verify and/or improve comprehension of the

experimental results obtained during the project progress.

On the one hand, Comsol Multiphysics facilitates setting-up a model for electromagnetic analysis, especially when using its AC/DC module, since it has predefined physics interfaces; which allow to have control over the definitions of constants, the use of the material properties, and the boundary conditions. Additionally, the models can take advantage of symmetry where possible to reduce of computation time and exploit available memory. Specifically, this software was employed to compute and plot the flux density underneath the electromagnet central core leg, and its variation with lift-off (gap between the core and a metallic sample). This software was also employed to calculate and visualise the magnitude of the current density induced by an alternating current flowing in the EMAT coil in non-magnetic and magnetic metallic samples (e.g. aluminium and steel), and its variation with lift-off (gap between the metallic sample and the coil).

On the other hand, PZFlex was used to analyse and validate the propagation of the ultrasonic wave generated/detected by the PE-EMAT. This software was chosen since its explicit time-domain approach lends itself to rapid analysis of broadband wave propagation problems. Therefore, time-domain finite element models were implemented taking into account the geometry of the sample, its material properties, and specific boundary conditions, such as absorbing boundaries to prevent unwanted echo signals or symmetrical boundaries to reduce the model complexity and reduce the computation time needed in the simulations.

2.6 Summary

In this background chapter an overview of the mathematical formulation used to describe time-varying deformations and internal restoring forces that lead to ultrasonic wave propagation in solid media was presented. Then, basic charac-

teristics of longitudinal and shear bulk waves were recalled (particle displacement and propagation directions, and phase velocity); and a brief explanation of different mechanisms that have an impact on the amplitude of the ultrasonic wave as it travels through a medium was given (absorption, scattering, geometric attenuation, and dispersion).

It is known that increasing the temperature in a solid medium affects ultrasonic propagation. Thus, considerations on the effect of rise in temperature in solids were given in this chapter (thermal expansion, density and elastic constants changes), with references to quantitative data obtained by other researchers for range of temperatures that includes the experimental temperatures used in this body of work.

Finally, a section devoted to finite element analysis was presented. References to work that show the research efforts devoted to study the underlying physical principles in the transduction mechanisms of Electromagnetic Acoustic Transducers (EMATs) were included. Together with descriptions of the electromagnetic and ultrasonic analysis performed using commercial software packages (Comsol Multiphysics and PZFlex), in order to verify and/or improve comprehension of the experimental results obtained in this body of work.

To conclude with the background chapters of this work a review of the operation principles of EMATs is presented in chapter (3); and an overview of the most representative transducers employed in NDT for high temperature applications is presented in chapter 4.

References

[1] R. B. Lindsay. *Acoustics: historical and philosophical development.* Benchmark papers in acoustics. Dowden, Hutchinson & Ross, 1973.

[2] K.F. Graff. Ultrasonics: Historical Aspects. In *Ultrasonics Symposium*, pages 1–10, 1977.

[3] G.A. Georgiou and T.B. Wooldridge. The basic principles, capabilities and limitations of ultrasonic NDT - Part 2. *Insight*, 42(11):708–712, 2000.

[4] R.E. Green. Non-contact ultrasonic techniques. *Ultrasonics*, 42:9–16, 2004.

[5] A.E.H. Love. *A treatise on the mathematical theory of elasticity.* Cambridge University Press, 4th edition, 1927.

[6] W.P. Mason. Physical Acoustics and the Properties of Solids. *Journal of the Acoustical Society of America*, 28(6):1197–1206, 1956.

[7] J.D. Achenbach. *Wave propagation in elastic solids.* Series in applied mathematics and mechanics. North-Holland, 1st edition, 1973.

[8] B.A. Auld. *Acoustic fields and waves in solids. Vol. 1.* Krieger publishing Co., 1990.

[9] J.L. Rose. *Ultrasonic waves in solid media.* Cambridge University Press, 1st edition, 1999.

[10] C. Kittel. Ultrasonics research and the properties of matter. *Reports on Progress in Physics*, 11(1):205, 1947.

[11] J.D.N. Ckeeke. *Fundamentals and applications of ultrasonic waves*. CRC series in pure and applied physics. CRC Press, 2002.

[12] W.P. Mason and H.J. McSkimin. Attenuation and scattering of high frequency sound waves in metals and glasses. *Journal of the Acoustical Society of America*, 19(3):464–473, 1947.

[13] J. Krautkramer and H. Krautkramer. *Ultrasonic testing of materials*. Springer-Verlag, 4th edition, 1990.

[14] R.B. Thompson. Ultrasonic measurement of mechanical properties. In *Ultrasonics Symposium*, pages 735–744, 1996.

[15] E.P. Papadakis. Revised grain-scattering formulas and tables. *Journal of the Acoustical Society of America*, 37(4):703–710, 1965.

[16] E.P. Papadakis. Ultrasonic attenuation caused by scattering in polycrystalline metals. *Journal of the Acoustical Society of America*, 37(4):711–717, 1965.

[17] ASM. *Properties and Selection-Irons, Steels, and High-Performance Alloys. ASM Handbook*, volume 1. ASM International, 1990.

[18] C.B. Scruby and B.C. Moss. Non-contact ultrasonic measurements on steel at elevated temperatures. *NDT&E International*, 26(4):177–188, 1993.

[19] F.A. Silber and C. Ganglbauer. Ultrasonic testing of hot welds. *Non-Destructive Testing*, 3(6):429–432, 1970.

[20] Md.S. Rohani. *The development of non-contact laser and EMAT ultrasound measurement systems for hot steel*. PhD thesis, University of Warwick, 1996.

[21] K. Kawashima. Theory and numerical calculation of the acoustic field produced in metal by an electromagnetic ultrasonic transducer. *Journal of the Acoustical Society of America*, 60(5):1089–1099, 1976.

[22] K. Kawashima. Quantitative calculation and measurement of longitudinal and transverse ultrasonic wave pulses in solid. *IEEE Transactions on sonics and ultrasonics*, 31(2):83–93, 1984.

[23] R. Ludwig and X.-W. Dai. Numerical simulation of electromagnetic acoustic transducer in the time domain. *Journal of Applied Physics*, 69(1):89–98, 1991.

[24] R. Jafari-Shapoorabadi, A. Konrad, and A.N. Sinclair. Improved Finite Element Method for EMAT analysis and design. *IEEE Transactions on magnetics*, 37(4):2821–2823, 2001.

[25] R. Jafari-Shapoorabadi, A. Konrad, and A. N. Sinclair. Computation of current densities in the receiving mode of electromagnetic acoustic transducers. *Journal of Applied Physics*, 97(10):10Q106, 2005.

[26] R.S. Edwards, X. Jian, Y. Fan, and S. Dixon. Signal enhancement of the in-plane and out-of-plane rayleigh wave components. *Applied Physics Letters*, 87: 194104(1)–194104(3), 2005.

[27] X. Jian, S. Dixon, K.T.V. Grattan, and R.S. Edwards. A model for pulsed Rayleigh wave and optimal EMAT design. *Sensors and Actuators A-Physical*, 128:296–304, 2006.

[28] X. Jian, J.P. Weight, K.T.V. Grattan, and S. Dixon. A model for transient ultrasonic field in solid generated by a transducer in immersion. *Sensors and Actuators A-Physical*, 133:439–446, 2007.

[29] M. Eskandarzade, T. Kundu, N. Liebeaux, D. Placko, and F. Mobadersani. Numerical simulation of electromagnetic acoustic transducers using distributed point source method. *Ultrasonics*, 50(6):583–591, 2010.

Chapter 3

EMAT operation principles

An Electromagnetic Acoustic Transducer (EMAT) consists of a coil to induce dynamic electromagnetic fields at the surface of a conductive material, and an element to provide a biasing magnetic field; which can be provided through permanent magnets or electromagnets. Depending on the geometry and arrangement of the coil and the magnet configuration, generation of different wave modes and polarisations are possible. Figure 3.1 shows a simple schematic diagram displaying the components of an EMAT.

Probably the earliest application of an EMAT to NDT was in 1939, when Randall[1] used a magnet and a coil to generate longitudinal vibrations in one end of a brass bar, and a similar arrangement of a magnet and a coil to detect the vibrating motion in the other end. Twenty years later, a similar configuration of magnets and coils was used to study the effects of radiation damage on the mechanical properties of metals[2]. In later years, there were many fundamental advances and some theoretical models to describe the transduction mechanism were developed[3,4]; effects in the transduction efficiency on ferromagnetic materials were described[5,6]; and precise descriptions on how practical transducers may be constructed and used for making measurements were published[7–9].

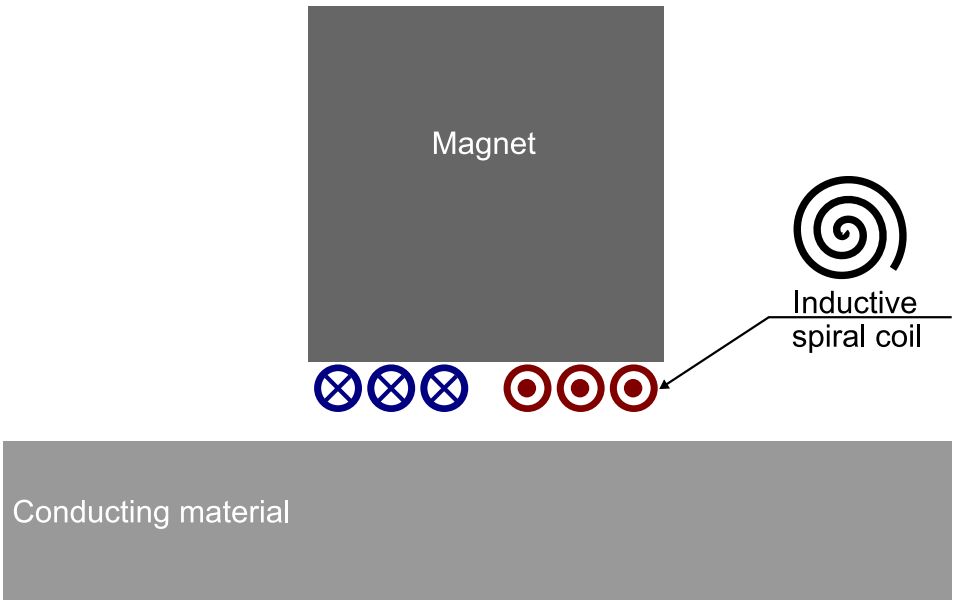

Figure 3.1: Cross-sectional schematic diagram of an EMAT and its typical components. Note: blue $\otimes$ represents a current going into the image plane, and a red $\odot$ represents a current coming out of the page.

The basic principles of operation of EMATs, including mechanisms that contribute to the coupling, and its supporting electronics are described in subsequent sections.

3.1 Maxwell's equations

Electromagnetic coupling allows EMATs to generate and detect ultrasound in metals without having direct contact between the transducer and the sample. The electrical energy is coupled into the sample as acoustic energy through two mechanisms: the Lorentz mechanism[10–13] (see section 3.3), and the magnetoelastic mechanisms[6,14] (see section 3.4). In order to describe the electromagnetic interactions between the EMAT and an electrically conductive sample, a framework defined by Maxwell's equations[15] is required, as listed in the following expressions.

$$\nabla \cdot \vec{D} = \rho \tag{3.1}$$

$$\nabla \cdot \vec{B} = 0 \tag{3.2}$$

$$\nabla \times \vec{E} = -\frac{\partial \vec{B}}{\partial t} \tag{3.3}$$

$$\nabla \times \vec{H} = \vec{j} + \frac{\partial \vec{D}}{\partial t} \tag{3.4}$$

where $\vec{D}$ is the electric displacement, ρ is the charge density, $\vec{B}$ is the magnetic field, $\vec{E}$ is the electric field, $\vec{H}$ is the magnetic field strength and $\vec{j}$ is the current density. The following relationships[15] also accompany Maxwell's equations:

$$\vec{D} = \epsilon_0 \epsilon_r \vec{E} \tag{3.5}$$

$$\vec{B} = \mu_0 \mu_r \vec{H} \tag{3.6}$$

where ϵ is the permittivity, μ is the permeability and subscripts $_0$ and $_r$ refer to the free space and the relative values respectively.

3.2 Image current and the skin effect

The first step to couple electromagnetically an EMAT to a conducting sample is injecting an alternating current ($\vec{I_c}$) through its inductive coil. The dynamic magnetic field ($\vec{B_c}$) associated with the generation current penetrates into the sample surface and is related to the induced electric field ($\vec{E}$) at the perimeter of the sample, as stated in Faraday's law (equation 3.3). The electric field in the electromagnetic wave sets up an image current (also known as eddy current) in the sample surface. Such a current will produce a magnetic field on its own, and resist the penetration of the electromagnetic wave deeper into the sample.

In order to make this clearer, it is necessary to derive an expression which represents an electromagnetic wave propagating in a conducting sample, using the following

procedure[15]:

$$\begin{aligned} \nabla \times \vec{E} &= -\frac{\partial \vec{B}}{\partial t} \\ \nabla \times (\nabla \times \vec{E}) &= -\frac{\partial}{\partial t}(\nabla \times \vec{B}) \end{aligned} \tag{3.7}$$

The function $\nabla \times (\nabla \times \vec{E})$ can be replaced using a vector identity:

$$\nabla \times (\nabla \times \vec{E}) = -\nabla^2 \vec{E} + \nabla(\nabla \cdot \vec{E}) \tag{3.8}$$

Additionally, if it is assumed that the net charge density in the sample remains zero ($\nabla \cdot \vec{E} = 0$), then the vector identity further simplifies ($\nabla \times (\nabla \times \vec{E}) = -\nabla^2 \vec{E}$), reducing equation 3.7 to:

$$\nabla^2 \vec{E} = \frac{\partial}{\partial t}(\nabla \times \vec{B}) \tag{3.9}$$

The right hand side of this equation can be expressed in terms of the electric field as:

$$\nabla^2 \vec{E} = \mu_0 \mu_r \sigma \frac{\partial \vec{E}}{\partial t} + \mu_0 \mu_r \epsilon_0 \epsilon_r \frac{\partial^2 \vec{E}}{\partial t^2} \tag{3.10}$$

The second term in the right hand side of this equation can be neglected since the sample is conductive and EMATs normally use frequencies lower than 100 MHz[14]; which implies that $\sigma >> \omega \epsilon_0 \epsilon_r$. Thus equation 3.10 takes the form:

$$\nabla^2 \vec{E} = \mu_0 \mu_r \sigma \frac{\partial \vec{E}}{\partial t} \tag{3.11}$$

When looking for a solution to this equation that represents an attenuated plane wave moving in the z-direction (inwards the sample), in such a wave:

$$\nabla^2 \vec{E} = \frac{\partial^2 \vec{E}}{\partial z^2} \tag{3.12}$$

Thus the differential equation obeyed by the plane wave becomes:

$$\frac{\partial^2 \vec{E}}{\partial z^2} = \mu_0 \mu_r \sigma \frac{\partial \vec{E}}{\partial t} \tag{3.13}$$

The quantity that measures how rapidly this plane wave is attenuated in the sample is called the skin depth or depth of penetration (d), and can be derived from equation 3.13 [15]:

$$d = \sqrt{\frac{2}{\mu_0 \mu_r \sigma \omega}} \tag{3.14}$$

The attenuated plane wave solution in terms of the skin depth has the form:

$$\vec{E_z} = \vec{E}_{z_0} e^{i(\omega t - \frac{z}{d})} e^{-\frac{z}{d}} \tag{3.15}$$

where $\vec{E_z}$ is the electric field inside the conductive sample at a depth z below the sample surface, $\vec{E}_{z_0}$ is the electric field at the sample surface, t is the time, and ω the angular frequency. The term $e^{-\frac{z}{d}}$ is the attenuation of the electric field as it increases with penetration depth, and the term $e^{-i(\frac{z}{d})}$ its phase relationship.

It is worth noting that if the thickness of the sample is much greater than the skin depth, its behaviour towards high-frequency alternating currents (as those injected through the inductive coil of an EMAT), becomes a surface phenomenon rather than a volume phenomenon. The resistivity in the surface is the resistance of a conducting sample of equal length and width, and has simply the dimension of

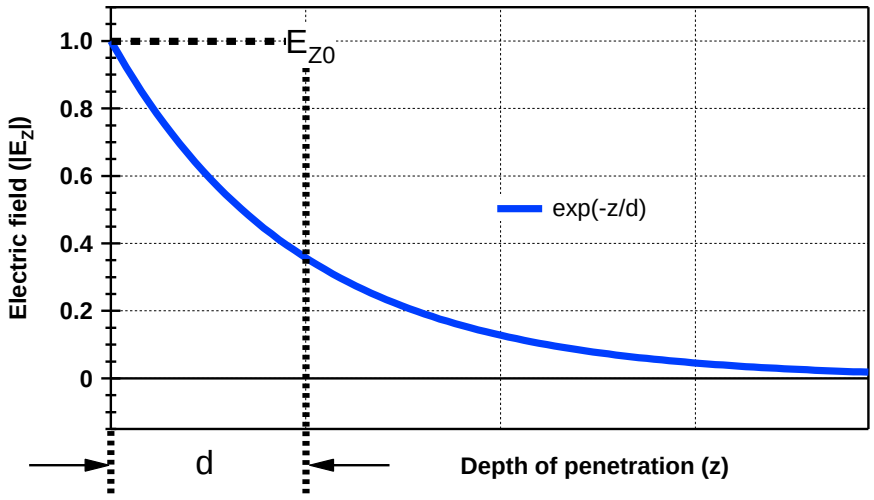

Figure 3.2: Attenuation of the electric field with distance inwards from the surface of a conductor. The curve is the magnitude of the electric field $|E_z|$.

resistance. Figure 3.3 shows a slab of conducting material that will be used to describe this phenomenon.

Since the conducting sample obeys Ohm's law ($\vec{j} = \sigma\vec{E}$, σ being the sample's conductivity), the calculation of the total current in the surface of the slab, and its corresponding current density can be done by expressing the latter as an equation analogous to 3.15:

$$\begin{aligned} \vec{j_z} &= \vec{j}_{z_0} e^{i(\omega t - \frac{z}{d})} e^{-\frac{z}{d}} \\ \vec{j_z} &= \vec{j}_{z_0} e^{i(\omega t)} e^{-(1+i)(\frac{z}{d})} \end{aligned} \tag{3.16}$$

where $\vec{j_z}$ is the current density at a depth z below the sample surface, $\vec{j}_{z_0}$ is the current density at the surface of the conducting sample. The decay of the current density is shown by the amplified shaded region on the left hand side of figure 3.3. The total image current (I) is given by the integral for infinite depth of $\vec{j_z}$ over the

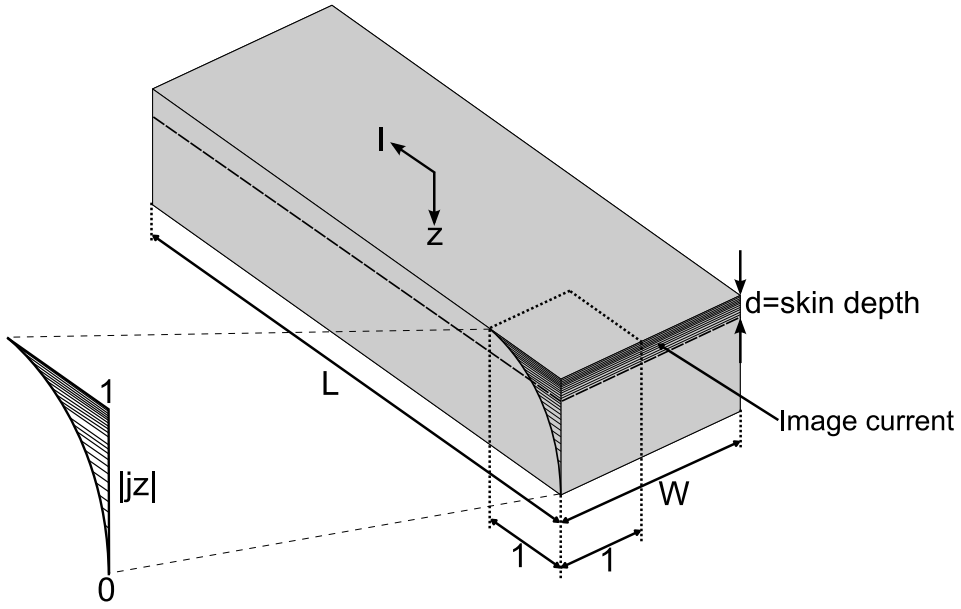

Figure 3.3: Diagram illustrating the skin effect on the surface of a slab of conducting material.

width W, as shown in[16]:

$$\begin{aligned} \vec{I} &= W\int_0^\infty \vec{j}_z dz \\ &= \vec{j}_{z_0} e^{i(\omega t)} W \int_0^\infty e^{-(1+i)(\frac{z}{d})} dz \\ &= \vec{j}_{z_0} e^{i(\omega t)} W \frac{d}{1+i} \end{aligned} \tag{3.17}$$

The surface impedance of the sample can be calculated from the image current and the voltage ($\vec{V}$) on the surface along the length of the slab (L), and can be expressed as[16]:

$$\begin{aligned} \vec{Z} &= \frac{\vec{V}}{\vec{I}} \\ &= (1+i)\frac{\rho L}{Wd} \\ &= (1+i)\frac{\rho L}{W(\sqrt{\frac{2}{\mu_0 \mu_r \sigma \omega}})} \end{aligned}$$

$$
\begin{aligned}
&= (1+i)\frac{\rho L}{W(\frac{1}{\sqrt{\mu_0\mu_r\sigma\pi f}})} \\
&= (1+i)\frac{\rho L\sqrt{\mu_0\mu_r\sigma\pi f}}{W} \\
&= (1+i)\frac{L}{W}\sqrt{\mu_0\mu_r\rho\pi f} \\
&= e^{i\pi/4}\frac{L}{W}\sqrt{\mu_0\mu_r\rho\pi f} \qquad (3.18)
\end{aligned}
$$

This approximation leads to the conclusion that, for any given frequency, the resistive and inductive part of the complex impedance are equal in magnitude, and the average of the image current inside the conducting sample is $\pi/4$ phase behind the induced electric field described at the beginning of this section, and a total of $3\pi/4$ phase lag from the generation current $\vec{I_c}$:

$$
\begin{aligned}
\vec{I} &= \frac{\vec{E}}{Z} \propto \frac{\vec{I_c}e^{-i\pi/2}}{e^{i\pi/4}} \\
&\propto \vec{I_c}e^{-i3\pi/4} \qquad (3.19)
\end{aligned}
$$

To summarize, the analysis presented here has shown that the induced image current must be at least $\pi/2$ phase behind the generation current anywhere in the sample, and if the sample has infinite depth, then the average of the image current in the sample has a phase lag of $3\pi/4$. Thus, is possible to represent graphically the generation of an image current when an alternating current is passing through a wire as it is shown in figure 3.4.

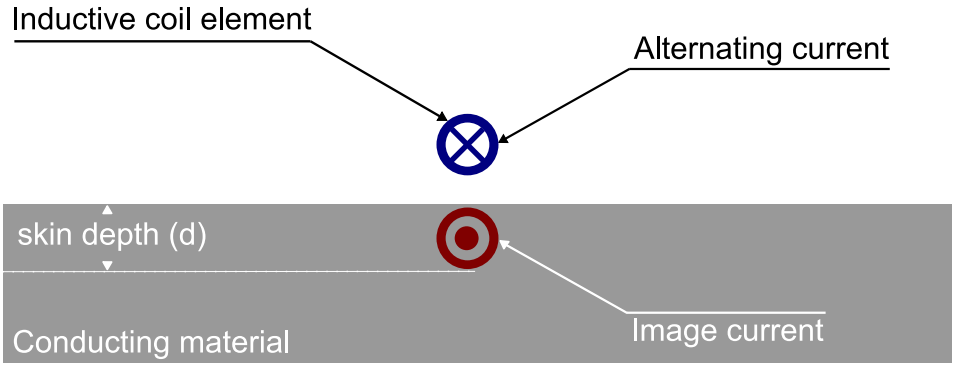

Figure 3.4: Diagram illustrating the generation of an image current at the surface of a conducting material when an alternating current is passing through a wire.

3.3 The Lorentz force mechanism

The force $\vec{F}$ experienced by charged particles in a medium subjected to the presence of an electric and magnetic field is the Lorentz force[17]:

$$\vec{F} = q(\vec{E} + \vec{v} \times \vec{B}) \tag{3.20}$$

where q is the electric charge, $\vec{E}$ is the electric field, $\vec{v}$ is velocity of the charged particle and $\vec{B}$ is the magnetic field. If the medium is macroscopically neutral in terms of electric charge density, then the Lorentz force is therefore reduced to:

$$\vec{F} = q\vec{v} \times \vec{B} \tag{3.21}$$

The magnetic field in this equation is the superposition of all sources of magnetic field; which are: the (quasi-) static magnetic field B_s from the EMAT itself (usually supplied by permanent magnet or an electromagnet), and the dynamic magnetic field B_c produced by the generation current. Figure 3.5 displays the Lorentz force due to a B_s, and figure 3.6 shows the Lorentz force as a result of the B_c.

The Lorentz contribution is generally dominated by the force generated from the static magnetic field, especially if the generation current is below 100 A through a

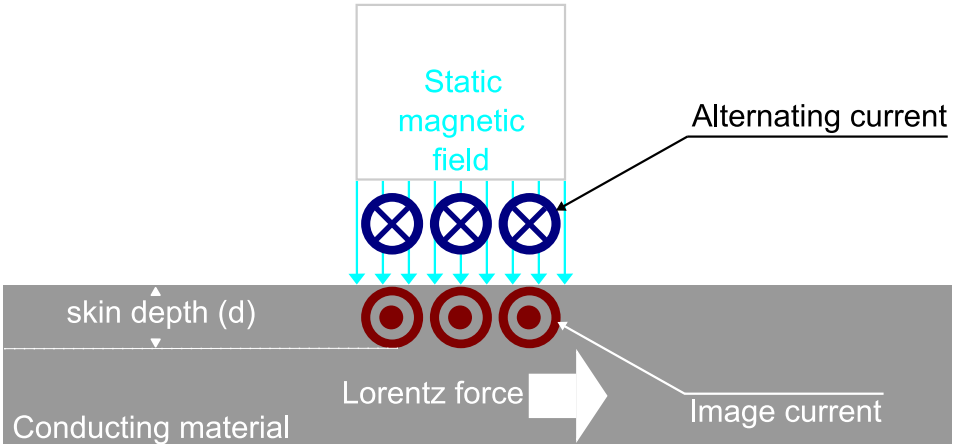

Figure 3.5: Diagram showing the Lorentz force arising from the interaction between the static magnetic field and the eddy currents induced in the near-surface of the sample.

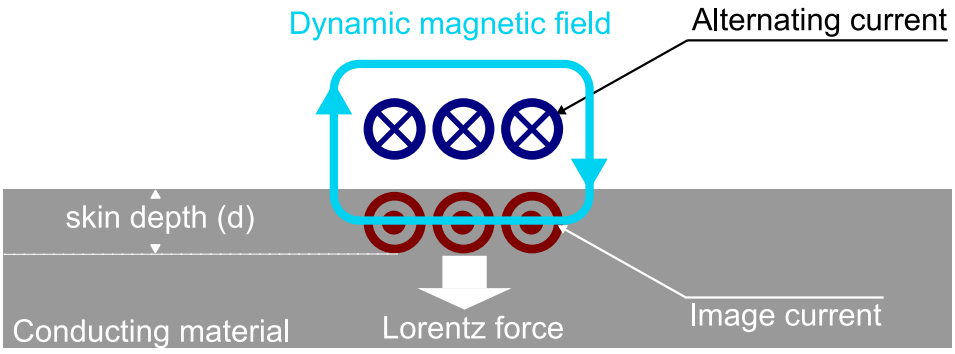

Figure 3.6: Diagram showing the Lorentz force arising from the dynamic magnetic field and the eddy currents induced in the near-surface of the sample.

typical EMAT coil. Above 500 A the force generated by the dynamic field is still relatively small[18,19], but not insignificant (e.g. 0.3 mT for a specific coil design reported in[20]).

To complete the discussion about equation 3.21, in metallic samples electrons are the only charge carrier of electric current, thus the equation of motion of an electron is[14]:

$$m\frac{d\vec{v_e}}{dt} = -e(\vec{E} + \vec{v_e} \times \vec{B}) - \frac{m\vec{v_e}}{\tau} \tag{3.22}$$

where m denotes the electron's mass and e the electron's charge, τ is the mean time of the electron-ion collisions (10^{-14} s for common metals at room temperature[14]). If the mean electron velocity is not changing, then the left-hand side of equation 3.22 is equal to zero, and the expression can be rearranged such that:

$$-e(\vec{E} + \vec{v_e} \times \vec{B}) = \frac{m\vec{v_e}}{\tau} \tag{3.23}$$

Now, considering a volume of a metal, which has an electron density of n_e and ion density N_i, the transfer of momentum to the ions from the scattering of electrons imparts a force per unit volume on the ions approximated as:

$$\vec{F} = N_i Z_i(\vec{E} + \vec{v_i} \times \vec{B}) + n_e\frac{m\vec{v_e}}{\tau} \tag{3.24}$$

here Z_i is the charge of the ion, and $\vec{v_i}$ is the average velocity of the ions. Given that the sample is charge neutral ($N_i Z_i = n_e e$) and also that $\vec{v_e} >> \vec{v_i}$, equation 3.24 reduces to:

$$\vec{F} = -n_e e\vec{v_e} \times \vec{B} = \vec{j} \times \vec{B} \tag{3.25}$$

where $\vec{j}$ is the image current density.

In summary, when the existence of an image current in the metallic sample has been defined, and in the presence of a magnetic field $\vec{B}$, the Lorentz force in equation 3.25 can cause an ultrasonic wave to propagate in the medium.

3.4 The Magneto-elastic mechanisms

The Lorentz mechanism outlined in the previous section will always be acting when an EMAT is used on a conducting sample. This same mechanism acts on ferromagnetic metals but two more mechanisms have to be considered: magnetization force and magnetostriction [21].

The magnetization force ($\vec{M}$) arises when ferromagnetic materials are exposed to an external field strength ($\vec{H}$). Following Hirao and Ogi [14], the force acting in the bulk of a sample and on its surface can be written as:

$$\vec{F} = \int_V \nabla^*(\vec{M} \cdot \vec{H})dv + \frac{1}{2}\mu_0 \int_S \vec{n} M_n^2 dS \tag{3.26}$$

∇^* denotes *nabla* operating only on the magnetic field intensity, $\vec{n}$ is a unit vector normal to the sample surface, and M_n is the normal component of the magnetization at the surface. The first integrand in this equation is known as the magnetization force. The second term appears because of a steep change of the electromagnetic fields at the surface and vanishes inside the sample.

Magnetostriction, on the other hand, is due to the fact that ferromagnetic domains tend to align along the direction of an external magnetic field, causing a net mechanical strain [22]. When the magnetic field has a time-varying component this strain can be exploited to launch ultrasonic waves [5,6].

The ultrasound transduction efficiency from this mechanism is strongly dependent on the physical material properties such as: elastic constants, electrical and mag-

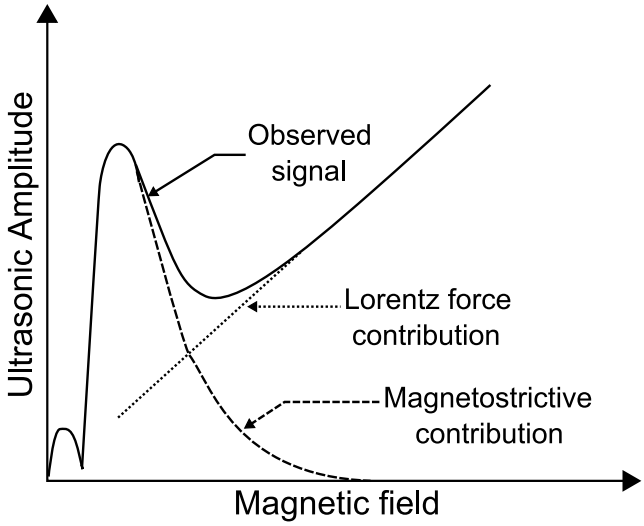

Figure 3.7: Schematic dependence of transduction efficiency due to Lorentz force and magnetostriction generation mechanisms in iron (after Thompson[6]).

netic properties; it also depends on the bias magnetic field and on the variation of all these factors as a result of temperature changes. Thompson[6] showed that the contribution of magnetostriction to the transduction efficiency is dominant at lower bias fields, but at high fields the Lorentz contribution prevails over magnetostriction (see figure 3.7).

The bias field configuration in EMATs is important when considering which mechanism is the dominant contributor to the transduction efficiency. Thompson[5] established that magnetostriction is the leading phenomenon in those EMAT configurations where the bias field is parallel to the surface. However, when the field is normal to the sample, some authors claimed that the Lorentz force dominates[23], while others[21,14] claimed that magnetostriction is the major contributor for most practical cases.

A thorough study on the operation of EMATs in ferromagnetic samples by Kiteley[24] demonstrated that for a normal bias field EMAT (as is the case of the EMAT system presented in this body of work), the Lorentz force is the dominant transduction mechanism in low tensile carbon steel, mild steel and cast irons. Whilst for

nickel and invar (nickel steel alloy), their highly non linear dependency regarding the bias field was attributed to an essentially magnetostrictive mechanism.
More recently, Ribichini *et al.*[25–27], have confirmed this showing that in a wide variety of steel samples the magnetostriction contribution is never larger than 5-10%. They also proved that using the same EMAT system on different steel samples is possible and small variations in signal amplitude would be expected (measured amplitudes do not differ by more than a factor of 2), since the Lorentz force is relatively insensitive to the range of material properties of steels. The only exceptions they found were when using the EMAT system in austenitic steel samples and steel samples with highly magnetostrictive oxide layer adhered to the surface. In those cases, the decrease in signal amplitude obtained in austenitic steel was attributed to the fact that the flux density was significantly smaller than in the case of ferromagnetic steels (refer to section 5.7 to compare the performance of the EMAT system presented in this work in non-magnetic and magnetic samples); whereas the increase in signal amplitude in the presence of an oxide layer was attributed to the higher contribution of magnetostriction to the transduction efficiency (refer to section 5.8 to observe the effect of an oxide layer adhered to a magnetic sample).

3.5 EMAT as ultrasound detector

As an ultrasonic wave propagates through a conducting sample, there is motion of the atoms in the lattice normal to the direction of propagation, the ions and conduction electrons will move in unison. When this motion occurs in the presence of a static magnetic field parallel to the wave propagation, both the electrons and ions experience a Lorentz force. The resultant acceleration of ions due to this force is insignificant when compared to that of the electrons, so that only electrons give

rise to an eddy current (strictly electrons with energies above or around the Fermi level[28]); which, in its turn, will generate an image current on the EMAT coil as described in section 3.3 for the generation process.

A key observation in the detection mechanism is that EMATs are in actual fact considered as particle velocity sensors[4], which can be shown following the procedure used by Dixon *et al.*[29]. For an ultrasonic wave travelling up to the material surface, its displacement can be described by the expression:

$$\vec{S}(t,z) = \vec{S_0} e^{i(\omega t - kz)} \tag{3.27}$$

where ω is the angular frequency of the ultrasonic wave, k is the wave number, t is the time and z is the direction of propagation. At the surface, the displacement vector ($\vec{\xi}$) is given by the sum of the wave travelling up to the surface and the reflection travelling away (see figure 3.8), as follows:

$$\vec{\xi} = \vec{S_0} e^{i(\omega t)} e^{ikz} e^{-ikz} = \vec{S_0} e^{i(\omega t)} (2cos(kz)) \tag{3.28}$$

Since the electric field induced inside the sample by the acoustic wave is proportional to the product of the rate of change of the displacement ($\frac{\partial \vec{\xi}}{\partial t}$) and the static magnetic field ($\vec{B_0}$)[14], then the current density at the surface ($\vec{j}(z)$) can be expressed as:

$$\vec{j}(z) = \sigma \frac{\partial \vec{\xi}}{\partial t} \vec{B_0} = i\omega\sigma \vec{S_0} e^{i(\omega t)} (2cos(kz)) \tag{3.29}$$

As the eddy current is confined within the electromagnetic skin depth (d) for a particular frequency, this implies that $z \leq d$. Additionally, the skin depth is much smaller than the ultrasonic wavelength in most cases ($kd << 1 \Rightarrow cos(kd) \approx 1$),

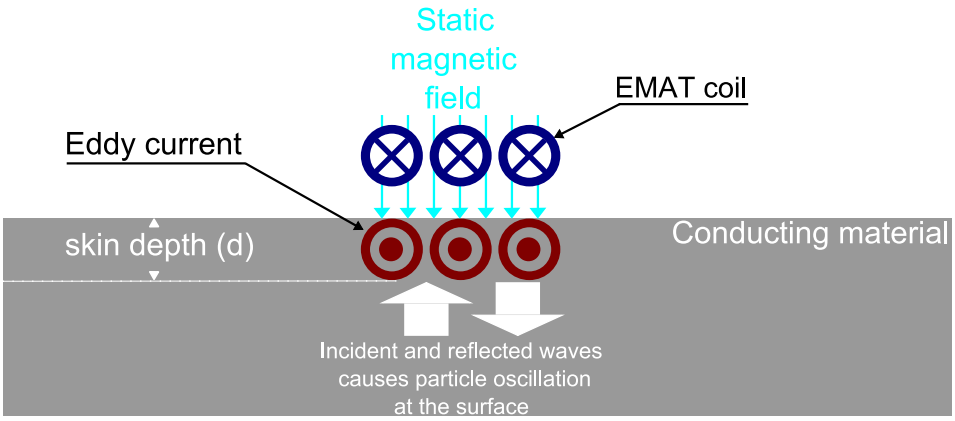

Figure 3.8: EMAT detection mechanism. The interaction between the particle displacement (at a speed $\frac{\partial \vec{\xi}}{\partial t}$) and the magnetic field ($\vec{B_0}$), sets eddy currents in the near-surface of the sample that will be detected by the EMAT coil.

thus the current density at the surface can be approximated to:

$$\vec{j}(z) \approx i\omega\sigma 2\vec{S_0}(t,0)e^{i(\omega t)} \approx 2\sigma\frac{\partial}{\partial t}(\vec{S_0}(t,0)) \tag{3.30}$$

which indicates that EMATs are in fact velocity sensors.

3.6 EMAT coil

Wave modes excited by means of EMATs depend mainly on the geometrical configuration of its coil and the orientation of the bias magnetic field. From these two elements, probably the most important is the high frequency coil, since its design can be optimised to maximise the ultrasonic generation/detection, assisting in this manner to fully exploit the advantage of a couplant-free sample evaluation system.

Typical coil designs include spiral, racetrack, and meander coils[14,30]; which can be seen in the schematic diagram shown in figure 3.9. The first two coils are mainly used for bulk-wave EMATs[7,8], and the latter is used for SH-wave[31], Rayleigh-wave and Lamb-wave EMATs[11].

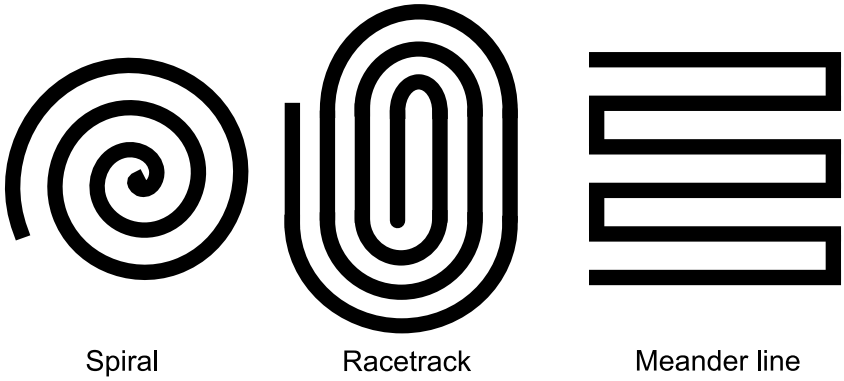

Figure 3.9: Schematic diagram showing some typical EMAT coil designs (Top view).

There are two different techniques to fabricate EMAT coils: printed circuit and wire wound coils. Printed circuit techniques permit to print any arbitrary pattern with high accuracy, typically within one micrometer[14], however this technique does not allow compact inter-winding separation affecting the eddy current induction and, consequently, the ultrasound generation. Moreover, this technique is limited for high temperature applications, since copper coils are frequently printed on polyimide resin laminates such as Tufnol; which only withstand temperatures below 250 ^{o}C[32]. On the other hand, wire wound coils have advantages over printed coils, they are flexible, high turn density is possible, and can be used for high temperature applications when encapsulated in high temperature ceramic adhesive, as will be shown in chapter 6. Figure 3.10 shows two spiral coils, a printed circuit board and wire wound coil versions.

The most important factor that must be taken into consideration when designing an EMAT coil is its impedance. In this regard, it has been shown that the capacitance between the coil and the metal sample, and the capacitance of inter-winding has a significant effect on the EMAT behaviour; specially for high-frequency wideband ultrasonic generation up to 30 MHz[33]. With respect to inductance, it has been demonstrated that the inductance of the coil increases with lift-off due to the decreasing mutual inductive coupling with the sample until it reaches its maximum

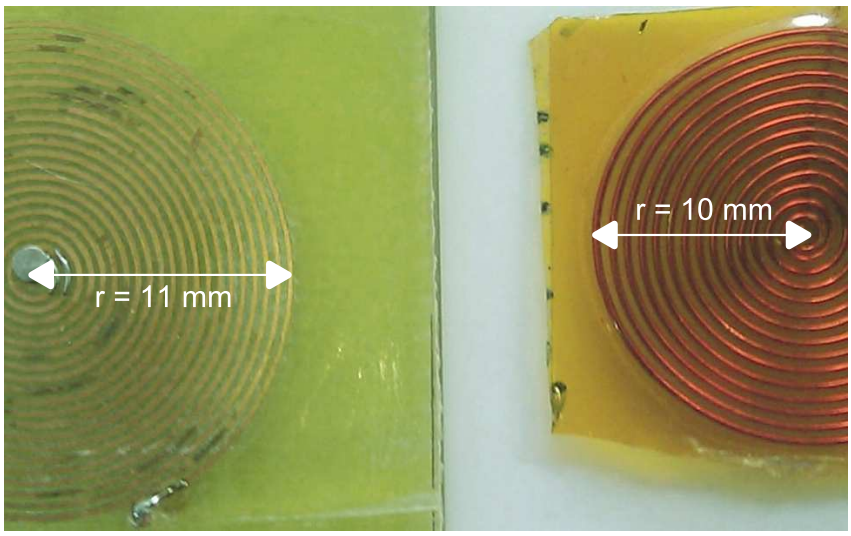

Figure 3.10: Photograph of different spiral coils. Printed circuit and wire wound versions.

value in free space[34].

A very detailed derivation of the sensitivity of an annular coil (special case of an spiral coil with just one turn) above metal samples is given by Jian *et al.*[35], discussing the influence of the lift-off, coil radius, material magnetic permeability and electrical conductivity on the coil impedance.

3.7 Electromagnet

Typically EMATs utilise permanent magnets to provide the bias magnetic field needed for operation, this is mainly because they can exert high magnetic fields with small structures. By far the most compact EMATs are constructed using rare-earth magnets: neodymium-iron-boron (NdFeB) or samarium-cobalt (SmCo). NdFeB magnets exhibit the highest remanent flux density (1.42 - 1.47T[36]) amongst commercially available magnets. However, because of their low Curie temperature they cannot be used at high temperatures, normally below 80 ^{o}C[14]. SmCo mag-

nets are more stable for high temperature operation than NdFeB magnets, but their maximum working temperature is below 300 ^{o}C[37]. Another limitation regarding the use of permanent magnets is that the magnetic field is fixed and cannot be increased; which would be desirable in ferromagnetic samples (permeability decreases when increasing the field).

A different approach is to utilise an electromagnet as was typical in the earlier generations of EMATs[9,8] and is still used in some recent designs[38]. The obvious advantages are that electromagnets can control the strength of the biasing magnetic field and that they can be used at elevated temperatures, well beyond the maximum operation temperature of permanent magnets.

Direct current (dc) electromagnets find limited use because the power requirements are quite high and because of the rapid heating of the energising coil caused by passing continuous current through it. This is because the Joule heating is proportional to the square of the current (I^2) in the energising coil[22]. For instance, if the current is doubled in a coil of fixed resistance the Joule heating is quadrupled.

An alternative to overcome these limitations, is to use pulsed current electromagnets, which operate by discharging a bank of capacitors using a fast switching device capable of withstanding high voltages and high currents (such a power MOSFET). The short duration high-current pulses produces high field strengths, with very little heating in the energising coil and, at the same time, reducing the power requirements considerably. For the purposes of the work presented here, this approach was chosen to generate the bias magnetic field needed for the EMAT operation. The design considerations of the electromagnet and its driving circuit are presented in chapter 5.

3.8 Summary

In this chapter a review of the operation principles of Electromagnetic Acoustic Transducers (EMATs) was portrayed. It was shown that electromagnetic coupling allows EMATs to generate and detect ultrasound in metals without having direct contact between the transducer and the sample. Also shown was the fact that the electrical energy is coupled into the sample as acoustic energy through two mechanisms: the Lorentz mechanism (see section 3.3), and the magnetoelastic mechanisms (see section 3.4). Additionally, a specific section regarding the detection mechanism was devoted to demonstrate that EMATs are in actual fact particle velocity sensors, following the procedure used by other researchers (see section 3.5). Then, it was recalled that wave modes excited by means of EMATs depend mainly on the geometrical configuration of its coil and the orientation of the bias magnetic field. Regarding the EMAT coil, a description of typical coil designs and configurations was included, together with factors that have to be taken into consideration in the coil design to fully exploit the advantage of a couplant-free sample evaluation system (see section 3.6).

It is known that typically EMATs use permanent magnets since they provide high magnetic fields with a compact size. For high temperatures, their relatively low Curie temperature is a disadvantage (e.g. 300 °C for SmCo, and 100 °C for NdFeB). A different approach is to utilise an electromagnet as was typical in the earlier generations of EMATs; the obvious advantages are that electromagnets can control the strength of the biasing magnetic field and that they can be used at elevated temperatures, well beyond the maximum operation temperature of permanent magnets. Thus, to conclude this chapter, the advantages of using a pulsed-current electromagnet for high temperature applications are also included.

References

[1] R. H. Randall, F.C. Rose, and C. Zener. Intercrystalline thermal currents as a source of internal friction. *Physical Reviews*, 56(4):343–348, 1939.

[2] D.O. Thompson and D.K. Holmes. Dislocation Contribution to the Temperature Dependence of the Internal Friction and Young's Modulus of Copper. *Journal of Applied Physics*, 30(4):525–541, 1959.

[3] E.R. Dobbs. Electromagnetic generation of ultrasonic waves in metals. *Journal of Physics and Chemistry of Solids*, 31(8):1657–1667, 1970.

[4] K. Kawashima. Theory and numerical calculation of the acoustic field produced in metal by an electromagnetic ultrasonic transducer. *Journal of the Acoustical Society of America*, 60(5):1089–1099, 1976.

[5] R. B. Thompson. Mechanisms of electromagnetic generation and detection of ultrasonic Lamb waves in iron-nickel alloy polycrystals. *Journal of Applied Physics*, 48(12):4942–4950, 1977.

[6] R. B. Thompson. A model for the electromagnetic generation of ultrasonic guided waves in ferromagnetic metal polycrystals. *IEEE Transactions on sonics and ultrasonics*, SU-25(1):7–15, 1978.

[7] B.W. Maxfield, M. Linzer, W.B. McConnaughey, and J.K. Hulbert. Design

of permanent magnet electromagnetic acoustic-wave transducers (EMATS). In *Ultrasonics symposium*, pages 22–25, 1976.

[8] B.W. Maxfield and C.M. Fortunko. The design and use of Electromagnetic Acoustic Wave Transducers (EMATs). *Materials Evaluation*, 41:1399–1408, 1983.

[9] W. Mohr and W. Repplinger. Ema-Excitation of ultrasonic bulk waves with the purpose of application in NDE. In J. deKlerk and B.R. McAvoy, editors, *Ultrasonics Symposium*, pages 126–131, 1978.

[10] M.R. Gaerttner, W.D. Wallace, and B.W. Maxfield. Experiments relating to the theory of magnetic direct generation of ultrasound in metals. *Physical Review*, 184(3):702–704, 1969.

[11] R.B. Thompson. A model for the Electromagnetic Generation and Detection of Rayleigh and Lamb Waves. *IEEE Transactions on Sonics and Ultrasonics*, 20(4):340–346, October 1973. doi: 10.1109/T-SU.1973.29770.

[12] W.P. Mason and R.N. Thurston. *Physical acoustics: Principles and methods*, volume 10. Academic Press, 1973.

[13] W.P. Mason and R.N. Thurston. *Physical acoustics: Principles and methods*, volume 14. Academic Press, 1979.

[14] M. Hirao and H. Ogi. *EMATs for Science and Industry. Noncontacting Ultrasonic Measurements*. Kluwer Academic Publishers, 2003.

[15] I.S. Grant and W.R. Phillips. *Electromagnetism*. John Wiley & Sons, 1991.

[16] H.A. Wheeler. Formulas for the Skin Effect. *Proceedings of the IRE*, 30(30): 412–424, 1942.

[17] D.S. Jones. *The theory of electromagnetism*. Pergamon Press, 1964.

[18] S. Dixon and X. Jian. Eddy current generation enhancement using ferrite for electromagnetic acoustic transduction. *Applied Physics Letters*, 89:193503(1)–193503(3), 2006.

[19] X. Jian and S. Dixon. Enhancement of EMAT and eddy current using a ferrite back-plate. *Sensors and Actuators A-Physical*, 136:132–136, 2007.

[20] Y. Fan. *The analysis of surface defects using the ultrasonic Rayleigh surface*. PhD thesis, University of Warwick, 2008.

[21] H. Ogi. Field dependence of coupling efficiency between electromagnetic field and ultrasonic bulk waves. *Journal of Applied Physics*, 82(8):3940–3949, 1997.

[22] D. Jiles. *Introduction to magnetism and magnetic materials*. Chapman & Hall, 1991.

[23] A. Wilbrand. Quantitative modelling and experimental analysis of the physical properties of electromagnetic ultrasonic transducers. In *Review of progress in quantitative nondestructive evaluation, Vol. 7*, pages 671–678, 1987.

[24] I.D. Kiteley. *A study of EMAT operation on ferromagnetic materials*. PhD thesis, University of Warwick, 1999.

[25] R. Ribichini, F. Cegla, P.B. Nagy, and P. Cawley. Evaluation of electromagnetic acoustic transducer performance on steel materials. *Draft*, pages 1–12, 2010.

[26] R. Ribichini, F. Cegla, P.B. Nagy, and P. Cawley. Quantitative modeling of the transduction of electromagnetic acoustic transducers operating on ferromagnetic media. *IEEE Transactions on Ultrasonics, Ferroelectrics and Frequency Control*, 57(12):2808–2817, 2010.

[27] R. Ribichini, F. Cegla, P.B. Nagy, and P. Cawley. Modelling of electromagnetic acoustic transducers operating on ferromagnetic materials. In D.O. Thompson and D.E. Chimenti, editors, *Review of progress in quantitative nondestructive evaluation, Vol. 29*, pages 964–971, 2010.

[28] S.B. Palmer and S. Dixon. Industrially viable non-contact ultrasound. *Insight*, 45(3):211–217, 2003.

[29] S. Dixon, C. Edwards, and S.B. Palmer. High-accuracy non-contact ultrasonic thickness gauging of aluminium sheet using electromagnetic acoustic transducer. *Ultrasonics*, 39:445–453, 2001.

[30] K. Mirkhani, C. Chaggares, C. Materson, M. Jastrzebski, T. Dusatko, A. Sinclair, R. Jafari-Shapoorabadi, A. Konrad, and M. Papini. Optimal design of EMAT transmitters. *NDT&E International*, 37:181–193, 2004.

[31] C.F. Vasile and R.B. Thompson. Excitation of horizontally polarized shear elastic waves by electromagnetic transducers with periodic permanent magnets. *Journal of Applied Physics*, 50(4):2583–2588, 1979.

[32] Tufnol. Tufnol composites limited. Engineering plastics and composites, 2010. URL `tufnol.com/tufnol/default.asp?id=66`.

[33] X. Jian, S. Dixon, R.S. Edwards, and J. Reed. Coupling mechanism of electromagnetic acoustical transducers for ultrasonic generation. *Journal of the Acoustical Society of America*, 119(5):2693–2701, 2006.

[34] J. Morrison, S. Dixon, M.D.G. Potter, and X. Jian. Lift-off compensation for improved accuracy in ultrasonic lamb wave velocity measurements using electromagnetic acoustic transducers (EMATs). *Ultrasonics*, 44:e1401–e1404, 2006.

[35] X. Jian, S. Dixon, R.S. Edwards, and J. Morrison. Coupling mechanism of an EMAT. *Ultrasonics*, 44:e653–e656, 2006.

[36] Supermagnete. Physical magnet data, 2010. URL `supermagnete.de/eng/data_table.php`.

[37] F. Herrault, D.P. Arnold, L. Zana, P. Galle, and M.G. Allen. High temperature operation of multi-watt, axial-flux, permanent-magnet microgenerators. *Sensors and Actuators A-physical*, 148(1):299–305, 2008.

[38] T. Yamasaki, S. Tamai, and M. Hirao. Arrayed-Coil EMAT for Longitudinal Wave in Steel Wires. In S. C. Schneider, M. Levy, and B. R. McAvoy, editors, *Ultrasonics symposium*, volume 2, pages 789–792, 1998.

Chapter 4

Review of techniques for high temperature applications

The demand for high temperature ultrasonic measurement systems in industrial environments has increased progressively, and a growing awareness within the NDT community for improvement of these systems is reflected by the large body of work published throughout the years. Below is a review of progress of the most representative techniques employed in high temperature applications.

4.1 Piezoelectric transducers

An important parameter of piezoelectric materials for high temperature applications is the Curie temperature (Tc) at which a structural transformation takes place and the piezoelectric properties are lost. A popular solution to avoid the piezoelectric material reaching this temperature is to use a waveguide, as reported by Jen *et al.*[1,2], in the form of a buffer rod. The rod has a variable temperature profile along its length, so that at the "cool" end a normal piezoelectric element can be operated well below its Tc. Another approach is based on the transmission of

ultrasound through thin waveguides, as was shown by Atkinson *et al.*[3], and since heat conduction is minimal along such thin elements, new applications are being developed such as the waveguide array presented by Cegla *et al.*[4] very recently. These solutions, although attractive, suffer from the fact that the waveguide must be strongly coupled to the test component, limiting their applicability to just one region of the component under test.

To achieve sufficient sensitivity and spatial resolution for NDT procedures, high temperature testing requires a piezoelectric material that can withstand heating to the temperature of the test component. Thus, suitable piezoelectric materials with elevated Tc have received attention in recent years. For instance, lead metaniobate (Tc $\approx$ 540 ^{o}C), modified sodium bismuth titanate (Tc $\approx$ 600 ^{o}C), lithium niobate (Tc $\approx$ 1210 ^{o}C), and aluminium nitride (has no known Tc, but is capable of operation at temperatures exceeding $\approx$ 1100 ^{o}C). Kazys *et al.*[5,6] have reported on the use of several of the aforementioned materials for measurements on the properties of a nuclear reactor coolant (liquid Pb/Bi alloy) at temperatures up to 450 ^{o}C.

The transducer design is not only dependent on the selection of the piezoelectric material, as coupling to the test specimen must also be considered. Most high temperature NDT applications fall into two different regimes that would have different requirements regarding couplant materials. Firstly, where only short term contact with the hot specimen is necessary and long term stability of the couplant is not a particularly important consideration. Secondly, where it is required to fix the transducer to the hot specimen permanently, and the long term stability of the couplant becomes crucial.

Couplants for short term usage, which are predominantly concerned with spot measurements (thickness gauging), are generally made using couplants such as those produced by Sonotech[7], and Pyrogel (maximum operation temperature up to 426 ^{o}C). However its use is limited and measurements must be carried out quickly since

they tend to dry out and no longer transmit the ultrasonic energy. In a higher temperature range, the Panametrics-NDT Couplant E is employed[8], since it is a semi-solid paste that liquefies at high temperature and has a maximum operation temperature up to 520 °C.

References on coupling materials for long term use with high temperature probes include fused salts, liquid metals, soft metal gaskets, solder glasses, solders, brazes and welds[9]. In addressing coupling for high temperature probes intended for long term deployment there are some particularly important considerations: thermal stability, high ultrasonic transmission, safety, and ability to withstand thermal cycling and the resultant thermal expansion of the materials without large degradation in the integrity of the junction.

Interest in brazes and solders, as a method of permanent attachment, arises from the possibility of achieving good acoustic transmission, relieving certain strain against thermal expansion of the materials that were bonded together, and reducing the number of interfaces that the ultrasound must pass through. However, there may be some concern that the degree of heating necessary to attach the probe may be beyond the maximum operating temperature of the piezoelement. Reports on the use of brazing and welding can be found in the work done by Arakawa[10] and Fothergill[11].

Interest in glasses arises from the wide range of physical and mechanical properties they encompass. For instance, very high adhesive bond strengths can be made between metals and glasses; nonetheless, in the course of experiments with glass solders[12], such as NaPoLi (sodium oxide, phosphor oxide, and lithium oxide), revealed that at higher temperatures the glass solder reacts chemically producing corrosion of the test component, medium term degradation and solidification of the glass layer when the test component is cooled[13].

As there is no definitive solution for high temperature ultrasonic couplants, other

technologies are being evaluated. For instance, the sol-gel[14] and chemical deposition[15] technologies are approaches to deposit high temperature piezoelectric transducers directly on metallic substrates. However, these technologies are far from a final solution[16].

4.2 Electromagnetic acoustic transducers (EMATs)

Electromagnetic acoustic transducers provide an excellent option for NDT applications and material characterization of conductive samples[17,18]. Although ultrasound transduction by EMATs is relatively inefficient compared to piezoelectric probes, its non-contact nature has advantages at elevated temperatures, the obvious one being that they do not suffer from couplant problems, and that they are able to scan moving samples.

Different approaches have been used in order to face the challenges that hostile environments represent. In essence, as EMATs comprise two main components (coil and magnet); these approaches depend firstly on the limitations of any of those components, and secondly on the proposed application. A brief outline on the design evolution and applications of EMATs intended for high temperatures is presented here.

Early EMAT designs for elevated temperature applications employed water-cooled DC electromagnets to provide the magnetic field needed for operation. For instance, experiments conducted on mild steel to study the effect of temperature upon generation and detection of surface waves, from room temperature up to 1000 ^{o}C, were reported by Cole[19]. The transducer comprised an E-core dc electromagnet with transmitting and receiving coils arranged between the central and outermost legs. The coils were identical and consisted of four elements in the form of grids, each having 3 turns of 0.5 mm diameter platinum wire, mounted on a former electrically

screened by a water-cooled copper surround.

Another arrangement capable of detecting a silicate inclusion in a mild steel bar at 650 °C, was reported by Whittington[20]. In this case the author employed an oil-cooled dc electromagnet, with two removable pole-pieces inserted through the centre leg to carry separate transmitting and receiving coils; which were wound as flat spirals protected by a ceramic facing.

Some years later, relatively small rare-earth magnets capable of producing magnetic field densities comparable to those produced by dc electromagnets became available; enabling compact permanent magnet EMATs to be fabricated. Neodymium-Iron-Boron (NdFeB) or Samarium-Cobalt (SmCo) magnets are usually the preferred choice, because they can be manufactured to have the highest magnetic energy product compared to other permanent magnets. However, for high temperature applications they are limited by the Curie temperature (Tc). In realistic operation conditions, the temperature of these magnets must be kept below their maximum operation temperature (80 °C for NdFeB[18], and 300 °C for SmCo[21]); otherwise a nearly complete remanence loss could be faced.

Consequently, water-cooled permanent magnet EMATs were incorporated to high temperature applications. EMAT pulser and receiver systems were usually employed in through-transmission mode for the inspection on hot steel tubes and pipes, as shown by Yamaguchi *et al.*[22]; and for thickness measurements on steel billets at temperatures below 600 °C, as demonstrated by Boyd *et al.*[23].

More recently, EMAT pulser and receiver systems capable of operating in pulse-echo mode were developed. Dixon *et al.*[24] demonstrated that a small NdFeB permanent magnet and a single-wound spiral coil (protected by a ceramic facing) held in a water-cooled brass housing, can be used to measure the wall thickness of steel galvanising kettle at their normal operating temperatures, which are in excess of 450 °C.

The combination of laser and permanent magnet EMATs for high temperature applications are presented in section 4.3.

4.3 Laser methods

The use of lasers to generate ultrasound has been well established for various years[25,26] as has also been the application of laser interferometry[27]. Its combination has been a powerful tool for flaw detection and materials characterization[28]. Due to its non-contact nature, laser generation and reception offered the possibility of testing materials at hostile environments (lasers with the associated optical components can be located well away from the specimen). For instance, a combination of high-energy Nd-glass laser as generator of ultrasound and a continuous wave laser interferometer as detector was probably first employed by Calder *et al.*[29,30], in order to determine the elastic constants of a stabilized plutonium alloy (from room temperature to 500 °C). Some years later, Dewhurst *et al.*[31] measured the temperature dependence of the longitudinal ultrasonic velocity in different media (iron and dural), at temperatures in excess of 1000 °C, using a Q-switched Nd:YAG laser to generate and a reference beam laser interferometer to detect. More recently, Scruby *et al.*[32] reported an extensive study to determine the temperature dependence of the ultrasonic velocity and attenuation, generation and reception sensitivity of the system in mild and stainless steel samples at temperatures up to 1200 °C.

There are potential disadvantages for laser reception systems as those used in the aforementioned references. Their sensitivity is at its maximum when the sample surface is highly polished. They rapidly lose sensitivity as the surface becomes roughened or dirty and absorbs the light. Such polished surfaces are hardly encountered in industrial environments, in particular at elevated temperatures where the sample tends to oxidise and the surface becomes tarnished. Scruby and Moss[32]

noted that in an oxidising atmosphere the surface deteriorated rapidly at 1000 °C, causing an estimated sensitivity loss of the order of 20 dB, and suggested that an alternative design of interferometer, such as the confocal Fabry-Perot system, might be a better solution because it is less sensitive to surface roughness, motion and convection. Dewhurst[33] and Cand[34], amongst others, have proved that confocal Fabry-Perot receivers are speckle insensitive; which means that they do not require precise focusing onto the surface, making such receivers suitable for use in optically rough surfaces. Monchalin and other authors[35–37] have demonstrated that these systems are applicable to real industrial conditions; for instance, measuring the wall thickness of tubes at 1000 °C in a steel mill.

The application of laser-EMAT combinations have also been studied and probably first presented by Alers *et al.*[38,39], who developed a system capable of operating on stainless steel samples at temperatures up to 500 °C. Ultrasound was generated by a Nd:YAG laser capable of producing energy about 850 mJ, and the magnetic field required for EMAT operation was provided by a magnetising coil housed in a water-cooled chamber.

More recently, the advent of stronger rare-earth magnets, such as Neodymium-Iron-Boron (NdFeB) or Samarium-Cobalt (Sm-Co), changed EMAT design. Accordingly, water-cooled permanent magnet EMATs were incorporated as ultrasound detectors in the laser-EMAT combinations, as it is shown by the vast amount of work reported by Idris, Edwards, Rohani and Baillie[40–44], amongst others.

Laser-EMAT combinations are relatively insensitive to the surface finish or roughness, which is an advantage over the laser detection systems. According to Baillie *et al.*[44], although the prototype system has been developed to detect defects in steel at 800 °C on a pilot scale rolling mill, significant work has to be done to perfect the system that could be used in steel plants and marketed for customers.

4.4 Other techniques

Thermal. The discontinuities in solid materials can change the heat flow condition; which can result in the fluctuation of the temperature on the surface of the materials. Both infrared testing[45] and thermal imaging[46] use this principle to measure the change of the surface temperature and then to deduce the discontinuity condition in the materials. Maldague has performed infrared thermography testing in small pipes to detect the wall thinning on an elbow when the part is loaded with transient thermal gradients, induced inside the pipe by changing the temperature of the circulating fluid or, alternatively, by applying a uniform heat source. More recently, Shen *et al.* showed that a thermal video system, using an infrared camera, was able to reveal defects in stainless steel and carbon steel pipes at temperatures up to 150 °C.

Probably the major weaknesses of this technique for applications at higher temperatures than those achieved in the experiments mentioned above, are: difficult data interpretation if the surface of an object has variable surface emissivities, frequent calibration may be required, and sensitivity can be affected by reflected or background radiation. Additionally, the initial cost of sensors and associated instrumentation is relatively high.

Eddy current. Eddy current testing (ECT) is arguably the most widely used electromagnetic technique for NDT purposes; its main applications range from thickness measurements of metallic plates to the inspection of heat-exchanger tubes in steam generators of nuclear power plants[47,48]. Although ECT systems are predominantly used for room temperature applications, there are references of their use at higher temperatures. For instance, Kasuya *et al.*[49] designed and constructed an ECT system for assessing the crack growth behaviour of welded pipes in a boiling water reactor environment (up to 300 °C). More recently, Urayama *et al.*[50] reported

the application of dual probe with simple structure combining an EMAT and Eddy current probe; which is employed to monitor wall thinning in a high temperature environment (300 ^{o}C).

Factors affecting EC probe response at room temperature measurements, are: material conductivity, permeability, lift-off, depth of penetration and trials frequency[51]; all become critical when temperature is increased. Thus, more work has to be done in ECT systems to overcome these limitations.

4.5 Summary

In this chapter a review of progress of the most representative techniques/transducers employed in high temperature applications was presented. Regarding piezoelectric transducers, it was shown that their design is not only dependent on the selection of the piezoelectric material, as coupling to the test component must be considered. References to short term and long term coupling materials were included. Additionally, since there is no definitive solution for high temperature couplants, references to other technologies were also included (see section 4.1).

Regarding EMATs, details of various water-cooled versions of DC electromagnet and permanent magnet EMATs were included. Different configurations for generation-reception were also presented, for instance: EMAT-EMAT configurations (pitch-catch or pulse echo), or Laser-EMAT configurations. It was acknowledged that the latter has attracted interest recently and a prototype system has been even developed to detect defects in steel on a pilot scale rolling mill, however some work has to be done to refine the system (see section 4.2).

Regarding laser methods, details of various configurations were presented: such as a combination of high-energy Nd:glass laser as generator and a continuous wave laser interferometer as detector, or using a Q-switched Nd:YAG to generate and a refer-

ence beam laser interferometer to detect. Also included is the solution to certain disadvantages for laser reception systems that need polished surfaces to enhance sensitivity (see section 4.3). Finally, two techniques that are also used for high temperature applications were included in this chapter: Thermal (infrared testing and thermal imaging) and Eddy current testing. Advantages and factors affecting its response, together with some other weaknesses for both cases, are presented (see section 4.4).

References

[1] C.-K Jen, B. Cao, K.T. Nguyen, C.A. Loong, and J.-G. Legoux. On-line ultrasonic monitoring of a die-casting process using buffer rods. *Ultrasonics*, 35(5): 335–344, 1997.

[2] C.-K. Jen, K.T. Nguyen, J.-G. Legoux, I. Ihara, and H. Hbert. Novel clad ultrasonic buffer rods for the monitoring of industrial materials processing. *NDTnet*, 4(4):16–20, 1999.

[3] D. Atkinson and G. Hayward. Fibre waveguide transducers for Lamb wave NDE. *IEE proceedings-science measurement and technology*, 145(5):260–268, 1998.

[4] F.B. Cegla and J.O. Davies. Ultrasonic crack monitoring at high temperatures using sh waves. In D.O. Thompson and D.E. Chimenti, editors, *Review of progress in Quantitative Nondestructive Evaluation Vol. 29*, pages 980–987, 2010.

[5] R. Kazys, A. Voleisis, R. Sliteris, L. Mazeika, R. Van Nieuwenhove, P. Kupschus, and H.A. Abderrahim. High temperature ultrasonic transducers for imaging and measurements in a liquid Pb/Bi eutectic alloy. *IEEE Transactions on Ultrasonics, Ferroelectrics and Frequency control*, 52(4):525–537, 2005.

[6] R. Kazys, A. Voleisis, R. Sliteris, B. Voleisiene, L. Mazeika, P.H. Kupschus,

and H.A. Abderrahim. Development of ultrasonic sensors for operation in a heavy liquid metal. *IEEE Sensors Journal*, 6(5):1134, 2006.

[7] Sonotech. High temperature couplants, 2010. URL `sonotech-inc.com/catalog/index.php?cPath=22_24`.

[8] Olympus. Ultrasonic couplants, 2010. URL `olympus-ims.com/en/ndt-application/183-id.209715236.html`.

[9] I. Atkinson, C. Gregory, S.P. Kelly, and K.J. Kirk. Ultrasmart: Developments in ultrasonic flaw detection and monitoring for high temperature plant applications. In *Proceedings of CREEP8*, pages 1–13, 2007.

[10] T. Arakawa, M. Tanosaki, and K. Yoshikawa. On-line monitoring techniques of crack propagation using brazed-type ultrasonic sensors for high temperature use. In *NDE in the nuclear and pressure vessel industries*, pages 217–221, 1995.

[11] J.R. Fothergill, P. Willis, and S. Waywell. Development of high-temperature ultrasonic transducers for under-sodium viewing applications. *British journal of non-destructive testing*, 31(5):259–264, 1989.

[12] H. Mrasek, D. Gohlke, K. Matthies, and E. Neumann. High temperature ultrasonic transducers. *NDTnet*, 1(9):6pp, 1996.

[13] A. McNab, K.J. Kirk, and A. Cochran. Ultrasonic transducers for high temperature applications. In *IEE Proceedings-Science, Measurement & Technology*, volume 145, pages 229–236, 1998.

[14] M. Kobayashi, T. R. Olding, M. Sayer, and C. K. Jen. Piezoelectric thick film ultrasonic transducers fabricated by a sol-gel spray technique. *Ultrasonics*, 39 (10):675–680, 2002.

[15] D.A. Stubbs and R.E. Dutton. An ultrasonic sensor for high temperature materials processing. *JOM-Journal of the minerals metals & materials society*, 48(9):29–31, 1996.

[16] R. Kazys, A. Voleisis, and B. Voleisiene. High temperature ultrasonic transducers: review. *Ultragarsas*, 63(2):7–17, 2008.

[17] B.W. Maxfield and C.M. Fortunko. The design and use of Electromagnetic Acoustic Wave Transducers (EMATs). *Materials Evaluation*, 41:1399–1408, 1983.

[18] M. Hirao and H. Ogi. *EMATs for Science and Industry. Noncontacting Ultrasonic Measurements.* Kluwer Academic Publishers, 2003.

[19] P.T. Cole. The generation and reception of ultrasonic surface waves in mild steel at high temperatures. *Ultrasonics*, 16(4):151–155, 1978.

[20] K.R. Whittington. Ultrasonic testing at high-temperatures. *Physics in technology*, 9(2):62–67, 1978.

[21] F. Herrault, D.P. Arnold, L. Zana, P. Galle, and M.G. Allen. High temperature operation of multi-watt, axial-flux, permanent-magnet microgenerators. *Sensors and Actuators A-physical*, 148(1):299–305, 2008.

[22] H. Yamaguchi, K. Hashimoto, and T. Kadowaki. Development of the wall-thickness measuring system using the electromagnetic-acoustic transducer for hot seamless steel tubes and pipes. *Materials Evaluation*, 43(10):1302–1303, 1985.

[23] D.M. Boyd and P.D. Sperline. In-plant demonstration of high-temperature EMAT system on continuous caster strand. In D.O. Thompson and D.E. Chi-

menti, editors, *Review of progress in quantitative nondestructive evaluation, Volume 8*, pages 1091–1097, 1989.

[24] S. Dixon, C. Edwards, J. Reed, and S.B. Palmer. Using EMATs to measure the wall thickness of hot galvanizing kettles. *Insight*, 37(5):368–370, 1995.

[25] R.M. White. Generation of elastic waves by transient surface heating. *Journal of Applied Physics*, 34(12):3559–3567, 1963.

[26] C.B. Scruby, R.J. Dewhurst, D.A. Hutchins, and S.B. Palmer. Quantitative studies of thermally generated elastic-waves in laser-irradiated metals. *Journal of Applied Physics*, 51(12):6210–6216, 1980.

[27] C.H. Palmer and R.E. Green. Optical detection of acoustic emission waves. *Applied optics*, 16(9):2333–2334, 1977.

[28] C.B. Scruby and L.E. Drain. *Laser ultrasonics. Techniques and applications.* Adam Hilger, 1990.

[29] C.A. Calder and W.W. Wilcox. Noncontact material testing using laser energy deposition and interferometry. *Materials Evaluation*, 38(1):86, 1980.

[30] C.A. Calder, E.C. Draney, and W.W. Wilcox. Noncontact measurement of the elastic-constants of plutonium at elevated-temperatures. *Journal of nuclear materials*, 97(1-2):126–136, 1981.

[31] R.J. Dewhurst, C. Edwards, A.D.W. McKie, and S.B. Palmer. A remote laser system for ultrasonic velocity measurement at high temperatures. *Journal of Applied Physics*, 63(4):1225–1227, 1988.

[32] C.B. Scruby and B.C. Moss. Non-contact ultrasonic measurements on steel at elevated temperatures. *NDT&E International*, 26(4):177–188, 1993.

[33] R.J. Dewhurst and Q. Shan. Modelling of confocal Fabry-Perot interferometers for the measurement of ultrasound. *Measurement Science and Technology*, 5 (6):655, 1994.

[34] A. Cand, J.P. Monchalin, and X. Jia. Detection of in-plane and out-of-plane ultrasonic displacements by a 2-channel confocal Fabry-Perot interferometer. *Applied Physics Letters*, 64(4):414–416, 1994.

[35] J.P. Monchalin, C. Nron, J.F. Bussire, P. Bouchard, C. Padioleau, R. Hon, M. Choquet, J.D. Aussel, G. Durou, and J.A. Nilson. Laser-Ultrasonics: From the Laboratory to the Shop Floor. *Advanced Performance Materials*, 5:7–23, 1998.

[36] B. Hutchinson, B. Moss, A. Smith, A. Astill, C. Scruby, G. Engberg, and J. Bjorklund. Online characterisation of steel structures in hot strip mill using laser ultrasonic measurements. *Ironmaking & steelmaking*, 29(1):77–80, 2002.

[37] D. Lvesque, S.E. Kruger, G. Lamouche, R. Kolarik II, G. Jeskey, M. Choquet, and J.-P. Monchalin. Thickness and grain size monitoring in seamless tube-making process using laser ultrasonics. *NDT&E International*, 39(8):622 – 626, 2006.

[38] G.A. Alers and H.N.G. Wadley. Pulsed laser/electromagnetic acoustic transducer approach to ultrasonic sensor needs for steel processing. In D.O. Thompson and D.E. Chimenti, editors, *Review of progress in quantitative nondestructive evaluation, Volume 6A*, pages 627–638, 1987.

[39] L.R. Burns, G.A. Alers, and D.T. MacLauchlan. A compact EMAT receiver for ultrasonic testing at elevated temperatures. In D.O. Thompson and D.E. Chimenti, editors, *Review of progress in quantitative nondestructive evaluation, Volume 7B*, pages 1677–1683, 1988.

[40] A. Idris. *Non-contact ultrasonic study on thixotropic alloys.* PhD thesis, University of Warwick, 1995.

[41] C. Edwards, S. Dixon, A. Idris, J. Reed, and S.B. Palmer. Applications of non contact ultrasonic evaluation. In D.O. Thompson and D.E. Chimenti, editors, *Review of progress in quantitative nondestructive evaluation, Volume 14B*, pages 2253–2260, 1995.

[42] Md.S. Rohani. *The development of non-contact laser and EMAT ultrasound measurement systems for hot steel.* PhD thesis, University of Warwick, 1996.

[43] I. Baillie, P. Griffith, X. Jian, and S. Dixon. Implementing an ultrasonic inspection system to find surface and internal defects in hot, moving steel using EMATs. *Insight*, 49(2):87–92, 2007.

[44] I. Baillie. *The development of a laser-EMAT system suitable for on-line inspection in the continuous casting plant-Innovation report.* PhD thesis, University of Warwick, 2008.

[45] X. Maldague. Pipe inspection by infrared thermography. *Materials Evaluation*, 57(9):899–902, 1999.

[46] G. Shen and T. Liebeaux. Infrared thermography for high-temperature pressure pipe. *Insight*, 49(3):151–153, 2007.

[47] J. Hansen. The eddy current inspection method - Part 4. Applications, practical testing and advanced concepts. *Insight*, 46(8):480–483, 2004.

[48] J. Hansen. The eddy current inspection method - Part 3. Instrumentation and applications. *Insight*, 46(7):414–416, 2004.

[49] T. Kasuya, T. Okuyama, N. Sakurai, H. Huang, T. Uchimoto, T. Takagi, Y. Lu, and T. Shoji. In-situ eddy current monitoring under high temperature environ-

ment. *International Journal of Applied Electromagnetics and Mechanics*, 20: 163–170, 2004.

[50] R. Urayama, T. Uchimoto, and T. Takagi. Application of EMAT/EC dual probe to monitoring of wall thinning in high temperature environment. *International Journal of Applied Electromagnetics and Mechanics*, 33(3-4):1317–1327, 2010.

[51] G. Van Drunen and V.S. Cecco. Recognizing limitations in eddy-current testing. *NDT International*, 17(1):9–17, 1984.

Chapter 5

PE-EMAT design evolution. Room temperature

5.1 Pulsed electromagnet and EMAT coil

For the purpose of this thesis, a pulsed electromagnet (PE) approach was selected in order to generate the magnetic field necessary for EMAT operation. As was mentioned earlier in chapter 3, this approach not only allows the generation of a high and controllable magnetic field, but also represents an alternative solution to the limitations of permanent magnets regarding their maximum temperature of operation.

For the electromagnet core it was decided that the best option was to use a ferromagnetic material known as Magnesil (3% Si, 97% Fe[1]); which is a widely used material in transformer and inductor designs, because it offers a relatively good permeability at high flux density and high saturation flux density[2], as can be seen in the hysteresis loop shown in figure 5.1.

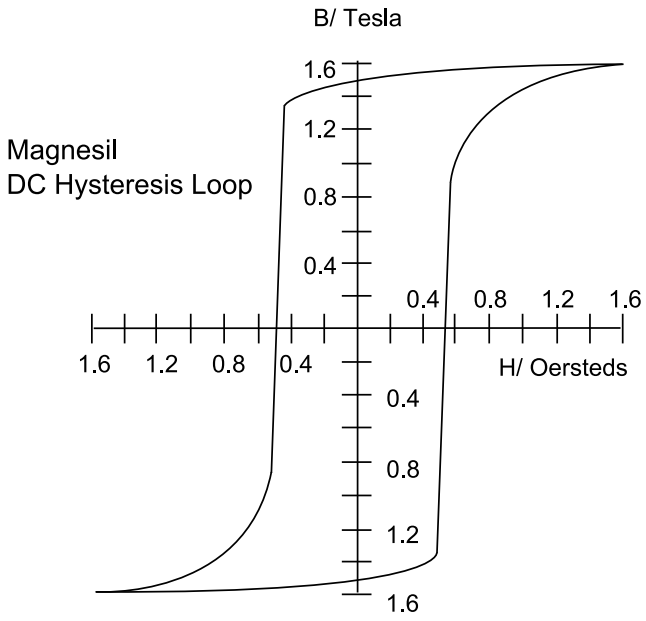

Figure 5.1: Hysteresis loop for the ferromagnetic material employed in the electromagnet core: Magnesil (after McLymam[2]).

An E-shaped laminated core obtained from a 100 VA transformer, was chosen to confine and guide the magnetic field produced by the energising coil. The core dimensions are 86 mm (length) x 57 mm (height) x 28 mm (width). The centre pole has an effective cross section area (A_c) of $\approx$ 784 mm^2, and was shortened to accommodate the EMAT coil by 3 mm. Two different views of the electromagnet core are shown in figure 5.2. The Volt-Ampere capability (or apparent power) of this core is 100 VA; which means that it is designed to operate with a maximum continuous current of $\approx$ 0.5 A from a 240 V supply. This would not be enough current to generate a DC magnetic field of 1.25 T in the air gap between the centre pole and a mild steel sample. To generate this amplitude of field, it would be necessary to have a magnetesiging current of about 9,600 A-turn; which is equivalent to a current of 12 A in an energising coil of 800 turns. Therefore, to enable the electromagnet to handle higher currents, it was decided to implement a driver circuit that delivers

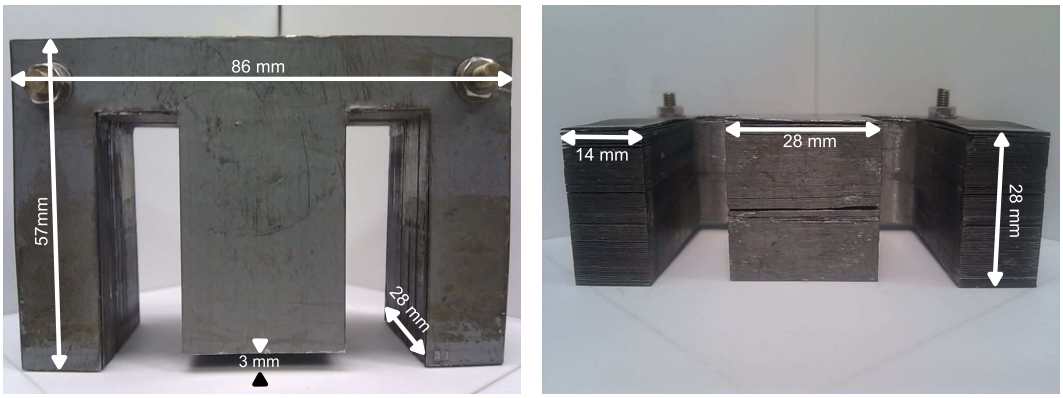

(a) Side view.

(b) Bottom view.

Figure 5.2: Photograph of the E-shaped core of laminated iron.

a current pulse with a regulated duty cycle (ratio between the pulse duration and pulse period); whose characteristics are presented in section 5.2.

The energising coil of the electromagnet consists of four coils connected in parallel (equivalent resistance $\approx 2.6\ \Omega$), each one of them with 200 turns of a polymer film insulated copper wire (outer diameter = 0.36 mm), and mounted on a plastic coil former on the centre pole as shown in figure 5.3. In this manner, the electromagnet generates a magnetic field from the centre pole with the other poles providing a return path closing the magnetic circuit.

The EMAT coil design was determined by consideration of the fact that it would be used in a pulse-echo configuration (acting as both as generator and detector of ultrasound). This is a constraint that needs further explanation in terms of electronics. The coil is essentially an inductive component with a resistive element, and a small parasitic capacitance. As generator of ultrasound, it is desirable that the total impedance of the coil is low, so that higher currents can be driven through the coil for a given current driver at MHz frequencies. The coil should also induce large image currents within the surface of a metallic sample, because this gives rise to a higher eddy current density and a larger signal amplitude. Therefore, on the one

Figure 5.3: Photograph of the electromagnet used for the preliminary trials.

hand the coil should have a small number of turns to maintain a low inductance, but on the other hand, the coil should have sufficient number of turns to induce a larger image current. In addition, when the coil is to be used as a detector, the impedance of the coil should be preferably high, as the induced signal is proportional to the number of turns in the coil.

With these compromising factors in mind various coils with different number of turns were tested and the best option regarding the signal amplitude resulted to be a wire wound spiral coil (diameter = 12.2 mm), consisting of 18 turns of a polymer film insulated copper wire (outer diameter = 0.36 mm), with an inductance of 1.6 μH and resistance of 0.1 Ω (measured with a Philips RCL meter, model PM6303 at 1kHz). The EMAT coil is mounted on a single-sided copper clad board to provide an electromagnetic screen and reduce unwanted ultrasonic generation in the core, and it is encapsulated in an epoxy resin to ensure durability of the coil (see figure 5.4). The board is bonded to the centre pole of the eletromagnet by a thin layer of cyanoacrylate adhesive, so that the EMAT coil and the other poles lie in the same plane.

The electromagnet and the EMAT coil are housed in a diecast aluminium case,

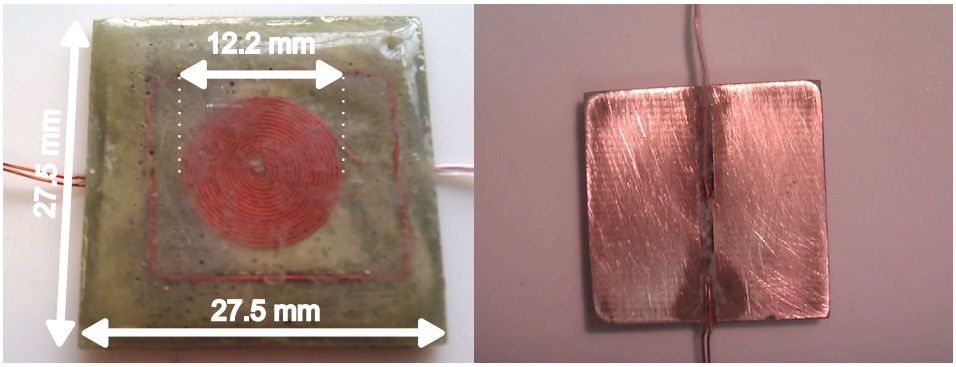

Figure 5.4: Photographs of the spiral coil employed for room temperature trials. Front and back views.

137 mm (length) x 60 mm (height) x 38 mm (width), as it is shown in figure 5.5.

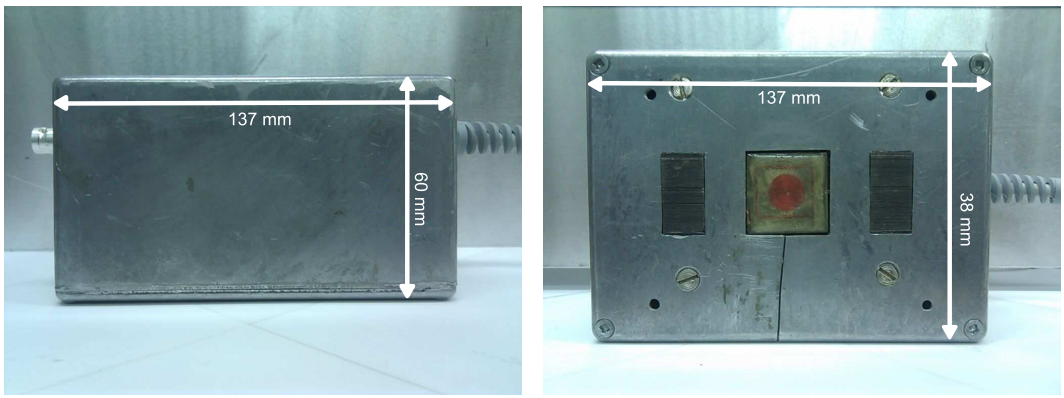

(a) Side view.

(b) Bottom view.

Figure 5.5: Photographs of the PE-EMAT case.

5.2 Current pulser for the electromagnet energising coil

As was mentioned in the previous section, the electromagnet coil, core and power supply can handle a higher current so long as the current is delivered in a pulsed mode rather than in a continuous mode. This can be done by discharging a bank of capacitors using a fast switching device capable of withstanding high voltages and high currents, such as a power MOSFET.

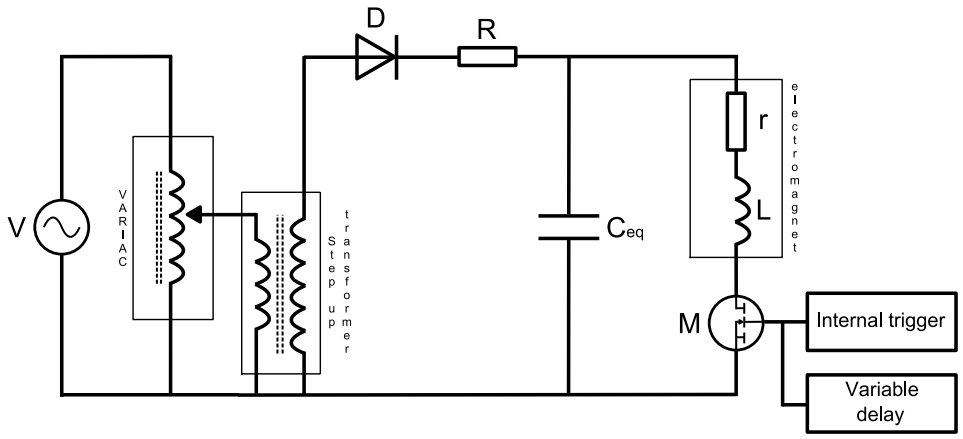

Figure 5.6: Basic schematic diagram of the electromagnet driver circuit; which consists of a variable autotransformer (VARIAC), a step up transformer, a rectifier diode (D), a current limiting resistor (R), a bank of capacitors (C_{eq}), a power MOSFET (M), and an internal/external trigger circuits.

A basic, schematic diagram of the electromagnet driver circuit designed for this project is shown in figure 5.6. Its operation is as follows: the bank of capacitors (represented in the schematic circuit by C_{eq}), is charged through the rectifier diode (D) and the current limiting resistor (R) to a high voltage (maximum of 700 V) by a step up transformer; which in turn is controlled by a variable autotransformer (VARIAC, 0-240 V). The power MOSFET (M) is turned on by a square wave with a pulse width of 3 ms, and repetition rate of 1 Hz, generated by the internal trigger circuit. When the power MOSFET is in the on-state, the bank of capacitors is discharged delivering a magnetising current to the electromagnet coil. A current monitor resistor in the discharge path of the bank of capacitors was included in order to monitor this magnetising current.

Since the electromagnet driver must be synchronised with the pulser/receiver system that drives the EMAT coil (see section 5.6) in order to obtain the maximum ultrasonic signal amplitude, then this circuit is complemented by a variable delay circuit that generates a square wave with a variable pulse width (from 1 to 5 ms), with the same repetition rate as the internal trigger.

The magnetising current was monitored by measuring the voltage across the aforementioned monitor resistor when the electromagnet is pulsed and placed over two different metallic samples: low carbon steel and aluminium (see figure 5.7). An interesting feature to note in figure 5.7(a) is that when the electromagnet is placed over the steel sample, the magnetising current saturates the electromagnet core, therefore the inductance of the energising coil changes and so does the rate of change of the current; which is clearly observed at ≈ 2.5 ms. This is not the case when the electromagnet is placed on the aluminium sample (see figure 5.7(b)).

It is worth noting that the measurement in the ferromagnetic sample was motivated because a wide range of steel materials with different physical properties are employed in plants operating at high temperature (e.g. low chromium carbon steel, and carbon steel with alloy cladding), and therefore it is relevant to the work presented here. Whereas, the measurement in the paramagnetic sample was in part motivated by the fact that it is a very common engineering material for industry, particularly the aerospace industry, and also because ferromagnet materials become paramagnetic when heated above their Curie temperature.

Thus, in order to get an idea of the overall performance of the PE-EMAT system, the flux density and the ultrasonic signal amplitude were measured for both low carbon steel and aluminium.

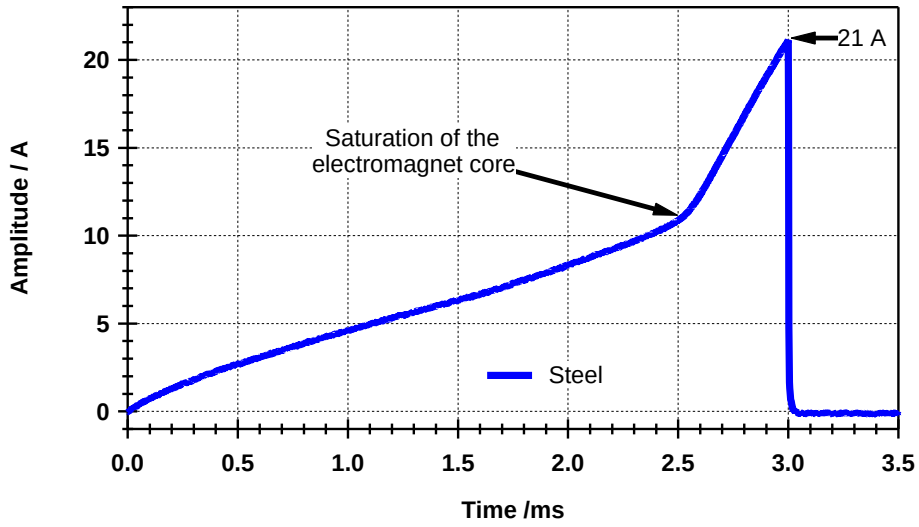

(a) Steel

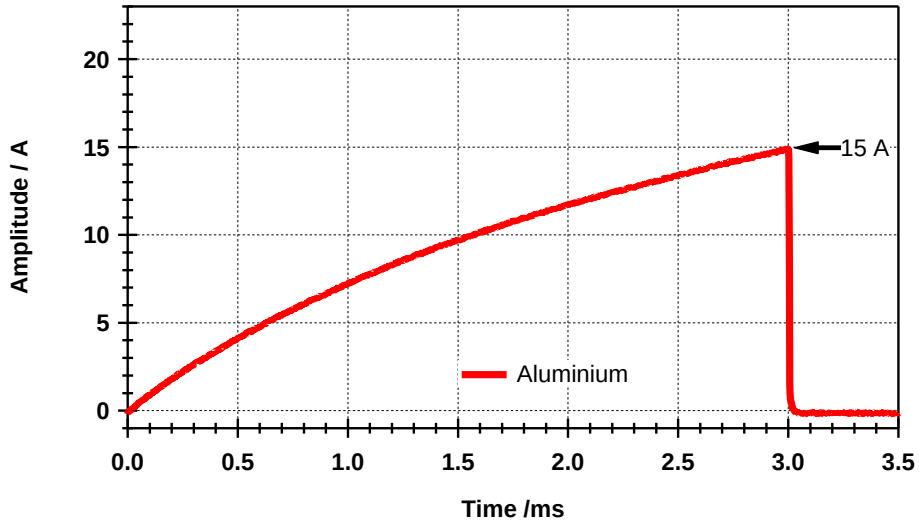

(b) Aluminium

Figure 5.7: The above graphs show the magnetising current as measured in the monitor resistor when the electromagnet is placed on two different samples: (a) low carbon steel and (b) aluminium. Note that the change in gradient of the magnetising current in the steel sample (a) at $\approx$ 2.5 ms, is due to the electromagnet core saturation.

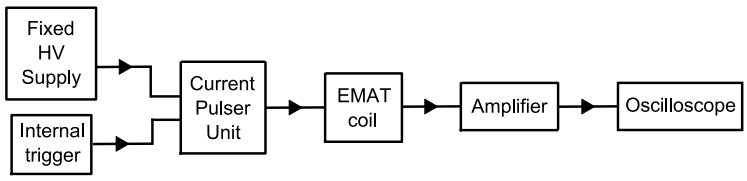

Figure 5.8: Block diagram of the pulser/receiver system for driving the EMAT coil.

5.3 Pulser/receiver system for EMAT coil

A block diagram of the pulser/receiver system designed for this project to drive the EMAT coil is presented in figure 5.8. The system consists of a current pulser unit to drive the EMAT coil in generation and a built-in amplifier to give the necessary wide band, low noise amplification required in the detection of ultrasonic waves, and its operation can be described as follows: the fixed high voltage power supply (500 V) charges a bank of capacitors in the current pulser unit in a similar fashion as in the electromagnet driver circuit presented in the previous section. A power MOSFET is turned on by a square wave (pulse width $\approx$ 300 ns), generated by the internal trigger circuit. When the power MOSFET is in the on-state, the bank of capacitors is discharged generating a broadband current pulse; which is delivered to the EMAT coil through a 50 Ω coaxial cable, usually no longer than a few metres in length. The current pulse through the EMAT coil was measured by placing a resistor (0.1 Ω) in the discharge current path and monitoring the voltage across this resistor as the coil was pulsed. The wide band current pulse has a magnitude of 21 A (see figure 5.9(a)), with significant frequency content between 0.5-20 MHz, but centred around 4.5 MHz (see figure 5.9(b)). As a receiver, the typical voltages induced in the EMAT coil are in the order of 10 μV. This received voltage pulse, is amplified by a pre-amplifier and is output for display and capture on a digital oscilloscope for signal processing. The shape of the observed ultrasonic signals for an EMAT system operating in pulse-echo mode (as is the case of the system presented here) is expected to be similar

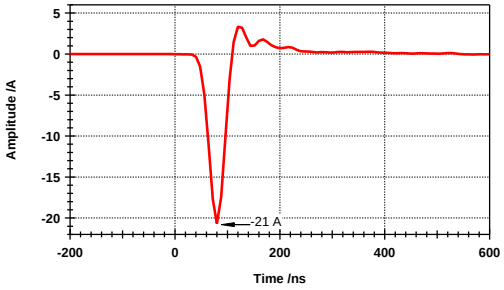

(a) Driving current pulse for EMAT coil

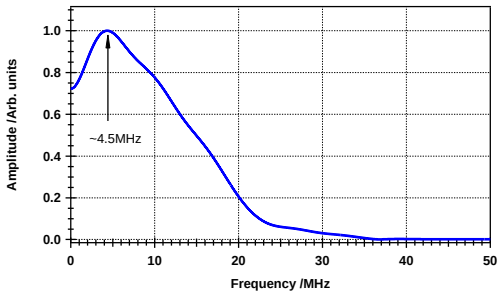

(b) Current pulse frequency spectrum

Figure 5.9: Current pulse generated to drive the EMAT coil and its frequency spectrum. Note that the frequency content is centred around 4.5 MHz.

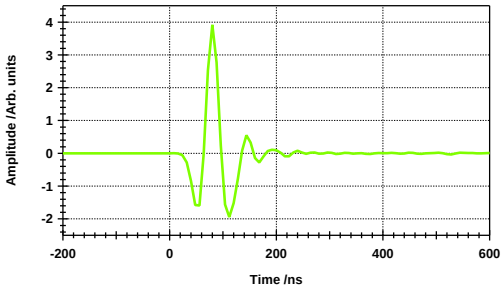

(a) Double differentiated current pulse

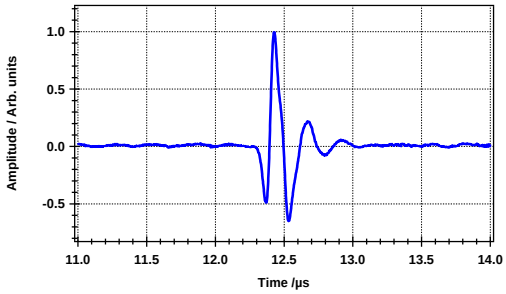

(b) Typical 1st back-wall echo

Figure 5.10: The double differential of the driving current pulse for the EMAT coil is similar to the typical 1st back-wall echo in the ultrasonic signal detected by the PE-EMAT system operating in a metallic sample.

to the double differential of the generation current pulse[3], which is confirmed by the comparison presented in figures 5.10(a) and 5.10(b). The double differential of the current pulse is very similar to the typical ultrasonic signal obtained with the PE-EMAT system operating on the steel sample that was mentioned in the previous section (a comparable waveform is obtained in the aluminium sample as can be seen in section 5.7, figure 5.19). Finally, it is important to mention that the generation current pulse discharged through the EMAT coil will paralyze the detection pre-amplifier for a finite time ($\approx 2\ \mu$s).

5.4 Hall-effect sensor

A driver circuit for a Hall-effect sensor (P15A, Advanced Hall sensors LTD) was designed and implemented in order to measure the pulsed magnetic field produced by the electromagnet. The driver circuit (shown in figure 5.11), requires a precision low voltage reference (MC1403, 2.5 V $\pm$ 0.25 mV) in order to set a constant voltage on the inverting input of an operational amplifier (OP-07), which is configured to act as a current source. The constant current (1.0 mA $\pm$ 1 μA) from the source is fed to the Hall sensor, which in the presence of a magnetic field perpendicular to its surface will produce an output voltage proportional to the magnetic field strength. The voltage output is small and requires additional amplification to achieve more useful voltage levels. For this purpose, a high accuracy instrumentation amplifier (AD620) is used, and configured to provide a fixed gain (G = 10). This element also provides a direct means of injecting a precise offset to its output, which in this case is a negative voltage (-64 mV) provided by another operational amplifier (OP-07) configured as an inverting amplifier, in order to nullify the positive offset voltage generated by the Hall sensor.

To ensure that the Hall sensor provided a linear output voltage proportional to the flux density in the range of interest, a field comparison check was carried out using a portable, calibrated Gauss meter (Model 705, Omitec Instrumentation) as a reference standard unit, and a NdFeB permanent magnet with well known characteristics (Grade N52, Remanent flux density (B_r) = 1.42 T).

The measurements were conducted by varying the distance between the magnet and the sensor; which was rigidly mounted facing to the geometric centre of the face of the magnet. The first measurement was carried out with contact between the sensor and magnet, afterwards with controllable increments of 0.5 mm $\pm$ 0.01 mm. As can be seen in figure 5.12, the fitted line has the slope equal to the correlation

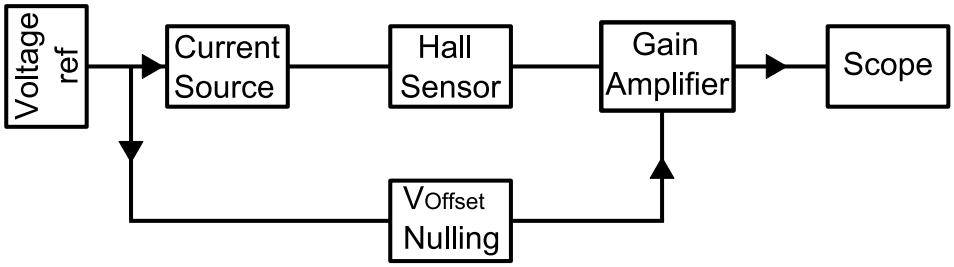

(a) Block diagram.

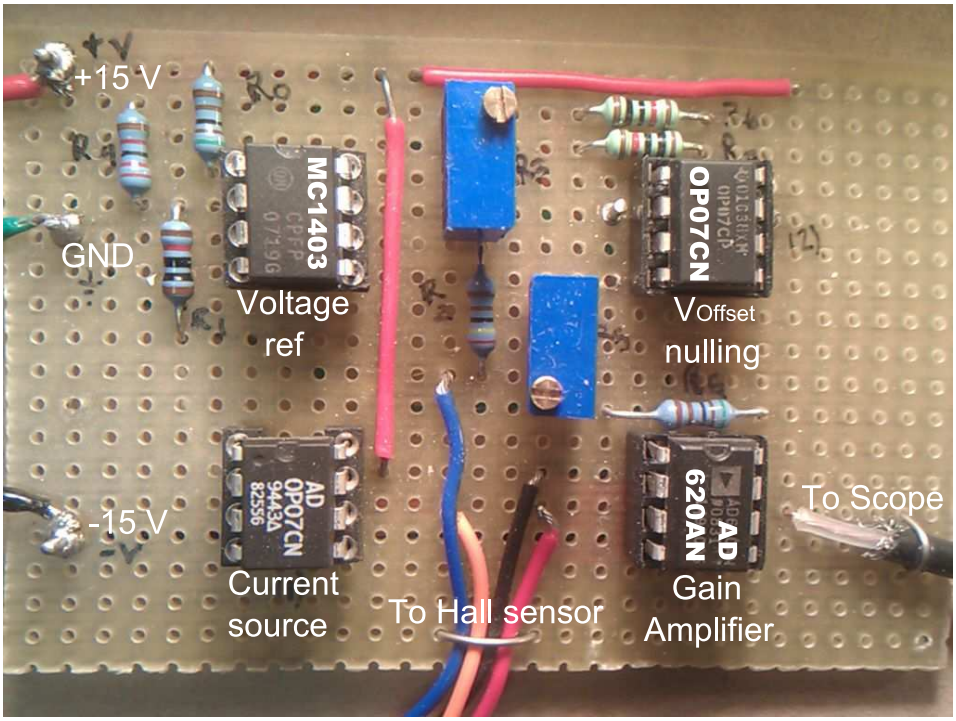

(b) Photograph.

Figure 5.11: Driving circuit for the Hall-effect sensor.

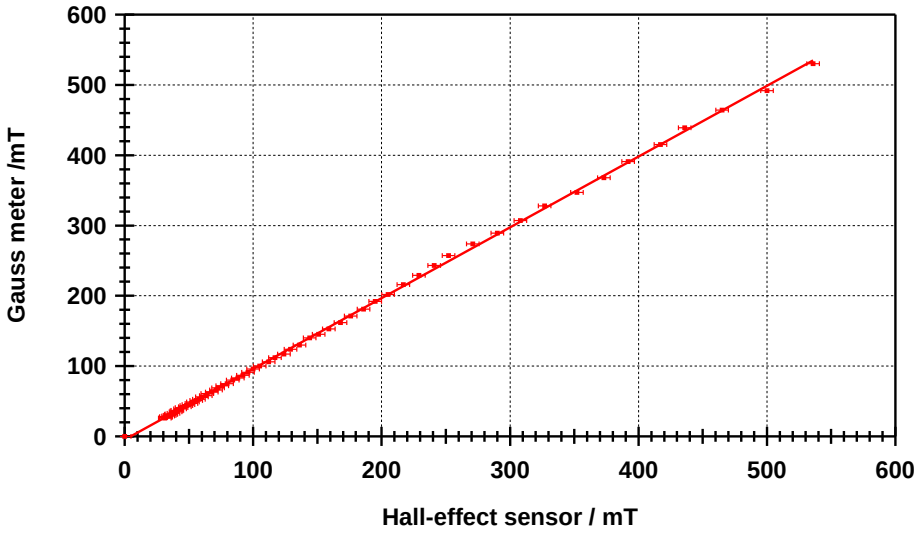

Figure 5.12: Field comparison check between a reference standard unit (Gauss meter, model 705, Omitec Instrumentation) and the Hall-effect sensor designed for this project.

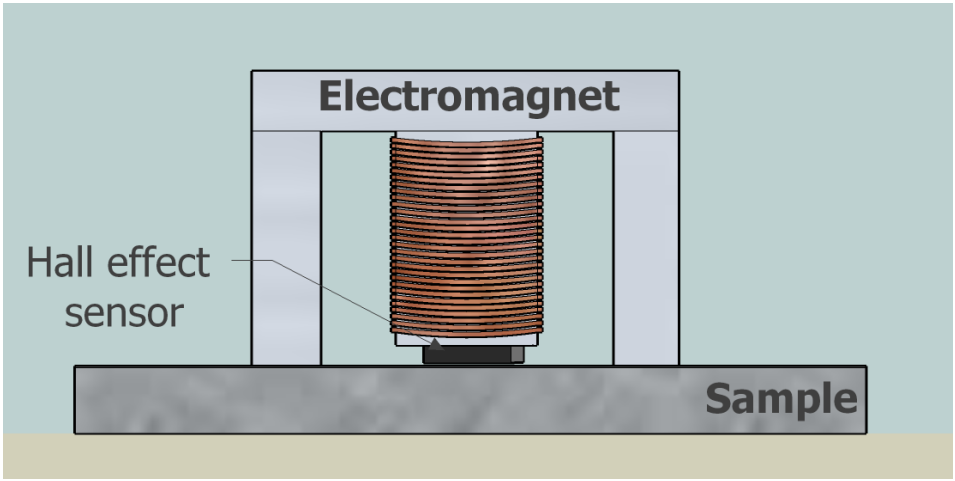

Figure 5.13: Experimental setup used to measure the flux density when the PE is placed on a metallic sample. Note that the EMAT coil was removed in order to perform these measurements.

between the measurements with the reference standard unit and the sensor designed for this project; which is 1.007 ± 0.002.

In order to measure the flux density produced by the PE, the EMAT coil was removed and the Hall sensor was located underneath the electromagnet central core leg. Measurements using the experimental setup shown in figure 5.13, were carried out on low carbon steel and aluminium. Figure 5.14(a) shows the flux density when the PE is placed on the steel sample, while figure 5.14(b) shows the one measured when the PE is placed on the aluminium sample. As can be seen, the flux density measured by the Hall sensor is more than three times stronger in low carbon steel compared to aluminium; which is explained by the fact that when the PE is working into a low reluctance magnetic circuit, the flux density increases considerably. The magnetic circuit has a return path through the steel sample; which is not the case with the aluminium sample, that is similar to having a magnetic open circuit (≈ infinite reluctance) at the frequencies present in the electromagnet driving pulse. The experimental results are confirmed by the finite element simulations carried out in Comsol Multiphysics 3.5a; which are shown in section 5.10.

5.5 Operation of the PE-EMAT system for ultrasonic measurements

In previous sections, all the elements that comprise the pulsed electromagnet (PE) EMAT system were shown separately with their respective design considerations and operation description. These elements are interconnected as illustrated in the schematic diagram of the experimental setup employed to perform ultrasonic measurements (see figure 5.15). The interaction between each element can be explained as follows: at the rising edge of the variable delay pulse generated by the electromagnet driver, a current pulse begins to flow in the energising coil of the

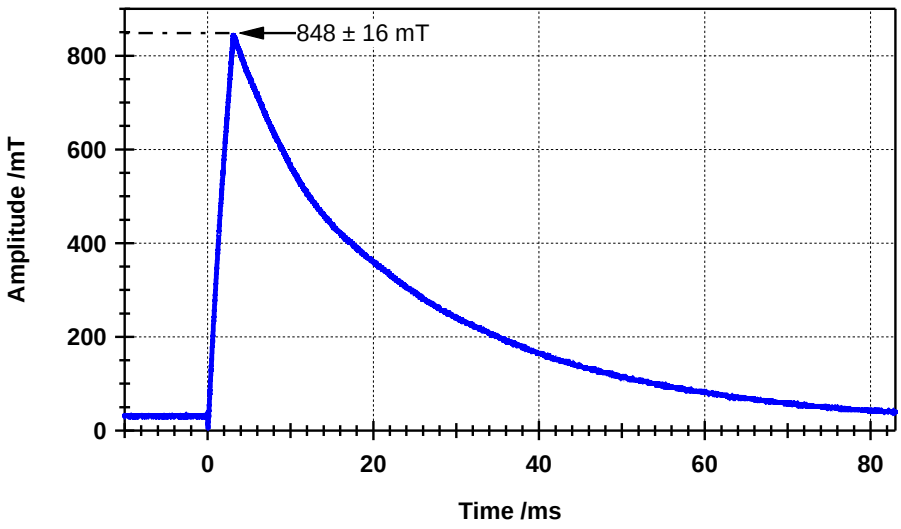

(a) Steel.

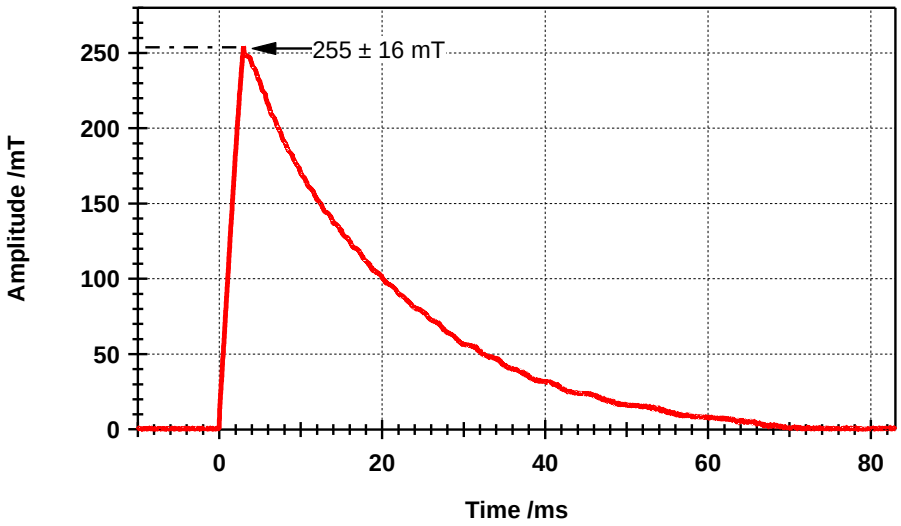

(b) Aluminium.

Figure 5.14: The above waveforms show the flux density measured by the Hall-effect sensor in two different samples. The sensor was located in the air gap, underneath the electromagnet central core leg as shown in figure 5.13.

electromagnet producing a pulsed magnetic field. Subsequently, at the falling edge of the trigger pulse, the system that drives a current pulse through the EMAT coil is fired to generate ultrasound.

This sequence of events is captured in a digital oscilloscope (Tektronix DPO2014). The signals are post-processed (normalised and shifted), and presented in the graph shown in figure 5.16. The graph corresponds to the optimum case for which the maximum ultrasonic signal amplitude is obtained. The pulse width of the variable trigger delay (red solid line) is 3.0 ms, at this specific time the current pulse through the electromagnet energising coil and the pulsed field below the EMAT coil (blue and orange solid lines, respectively), are at their maximum peak values. The system that drives the current through the EMAT coil is triggered exactly at this time.

It is worth mentioning that the ultrasound generation/detection occurs in the microseconds range, thus it will always take place when the pulsed field is still around the maximum peak value because the time constant of the pulsed field decay is in the milisecond range (after 500μs of having reached the maximum flux density, this has reduced only $\approx 3\%$).

The discussion regarding the optimisation process of the ultrasonic signal amplitude is presented in the following section.

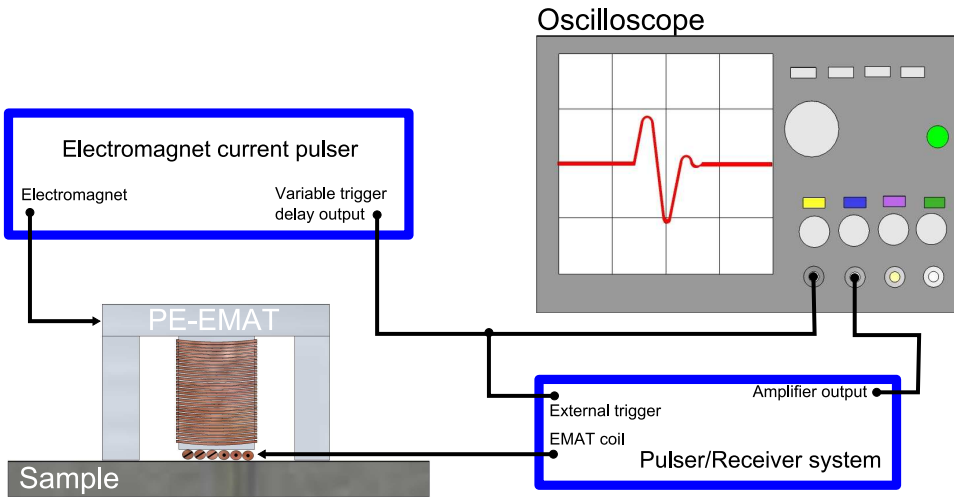

Figure 5.15: Schematic diagram of the experimental setup for ultrasonic measurements using the PE-EMAT system.

5.6 Ultrasonic signal amplitude optimisation

The ultrasonic signal amplitude depends inversely upon the material density and the skin depth, and is proportional to the bias magnetic field and the dynamic magnetic field produced by the EMAT coil[4–6]. The bias magnetic field is dominant over the dynamic field in the EMAT configuration employed in this work (see section 5.9, for a comparison of the estimated magnitude of these values). Thus it is important to ensure that the ultrasonic generation occurs when the bias field is at its maximum value; which means, in terms of the experimental setup presented here, to synchronise precisely the triggering time of the current pulser that drives the EMAT coil, with the time at which the bias field provided by the electromagnet has reached its maximum value.

Varying the time at which the current is discharged through the electromagnet energising coil, allows one to control the time at which the flux density is at its maximum value. Thus, different values for the pulse width of the variable trigger delay were

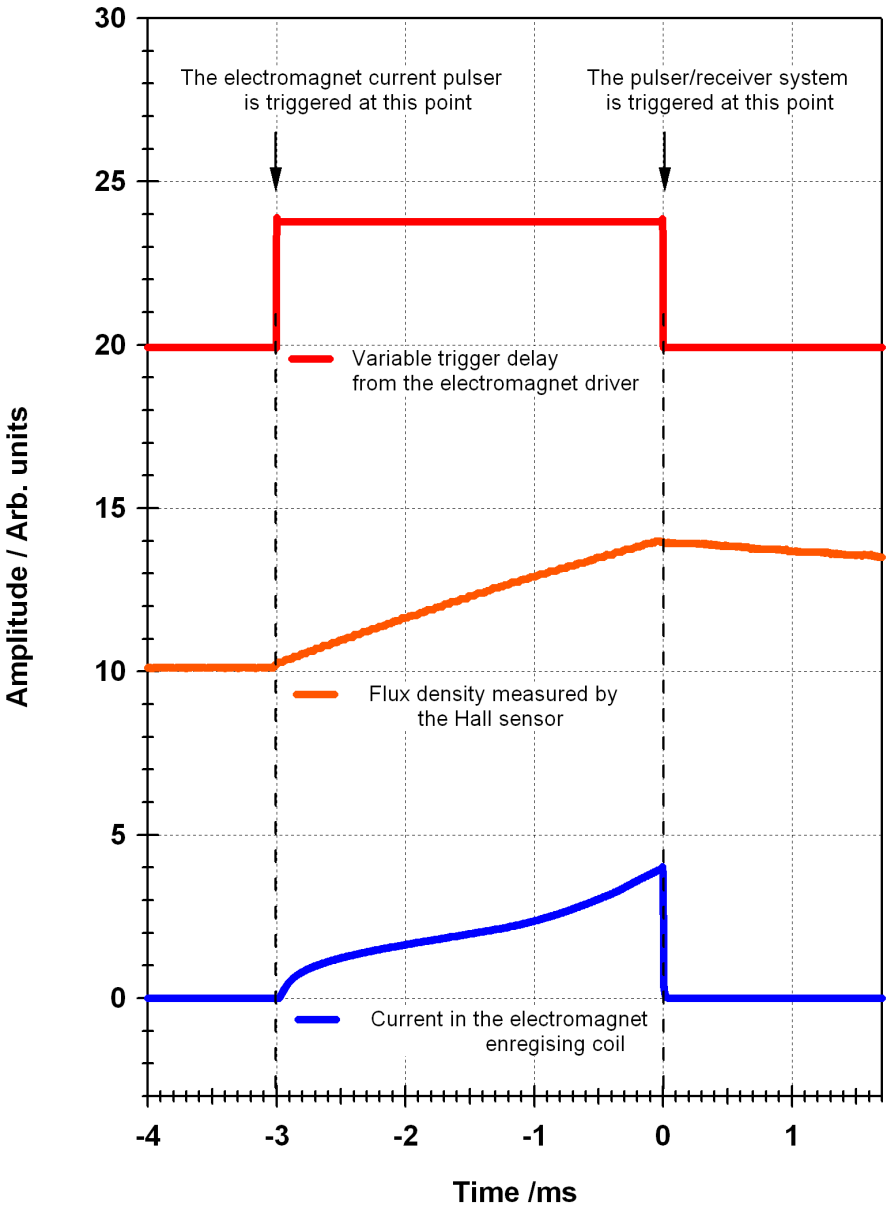

Figure 5.16: Triggering sequence for the electromagnet current pulser and the EMAT pulser/receiver system. In this case the variable trigger delay pulse width is 3.0 ms; which corresponds to the time at which the current in the energising coil and the flux density have reached their peak values, and the time at which the generation of ultrasound occurs.

tested, starting at 3.6 ms and then reducing it down to 2.4 ms, with steps of 0.2 ms. For every pulse width tested, the measurement was repeated five times, and for each measurement the ultrasonic signal was averaged (16x) and recorded in the oscilloscope. The peak to peak amplitude of the first back-wall echo was measured as shown in figure 5.17, and the arithmetic mean was calculated for every set of experiments. The signals were normalised with respect to the maximum amplitude obtained and the optimum time delay for triggering the EMAT pulser/receiver system was determined.

As can be seen in figure 5.18, it was found that the maximum signal amplitude was obtained when the time delay was 3 ms; which corresponds to the pulse width of the current through the electromagnet energising coil (see section 5.2) and, therefore, to the time at which the flux density is at its maximum value, as would be expected.

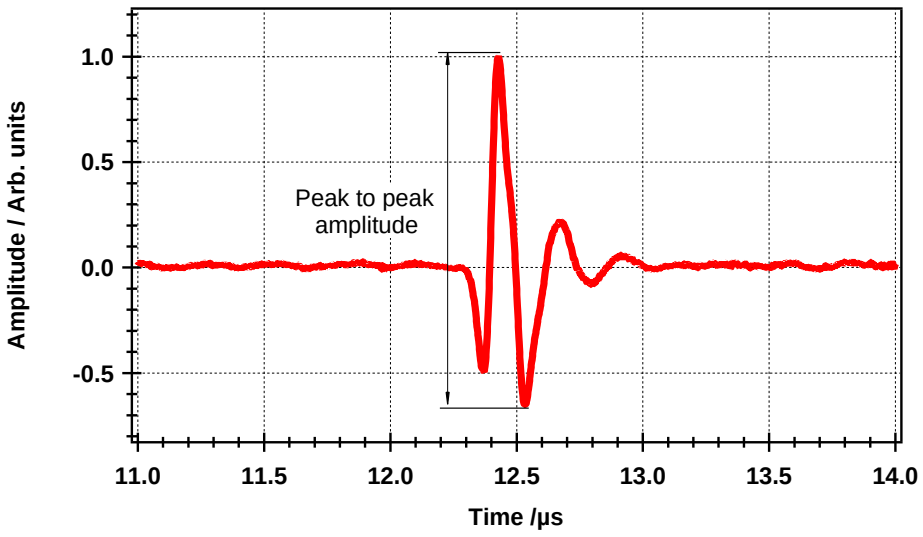

Figure 5.17: Peak to peak amplitude measurement of a typical first back-wall echo obtained when the PE-EMAT system is operating in a low carbon steel sample. Part of the ultrasonic signal amplitude optimisation process.

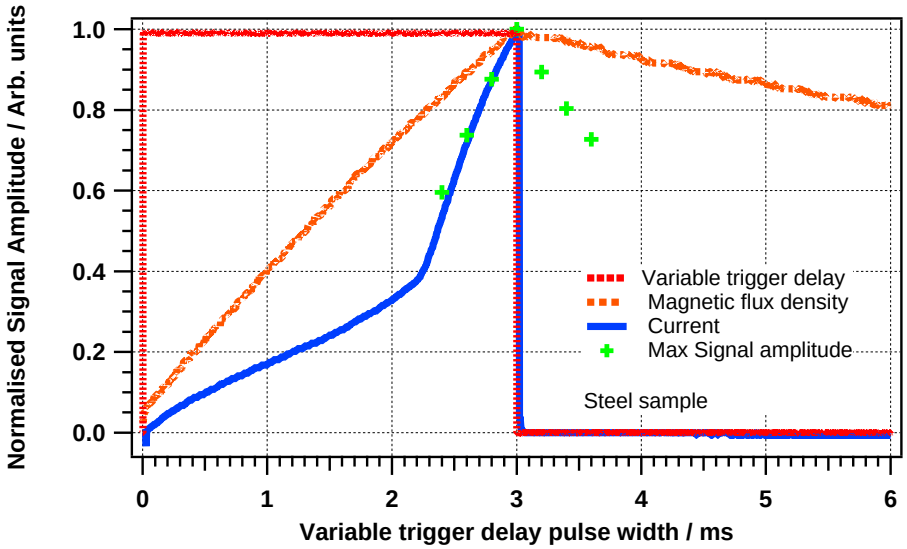

Figure 5.18: Optimising the ultrasonic signal for maximum amplitude of the first back-wall echo when the PE-EMAT system is operating in a low carbon steel sample. Note that the maximum signal amplitude coincides with the maximum flux density.

5.7 Shear wave generation in different media

A comparison of the performance of the PE-EMAT system on low carbon steel (thickness = 19.7 ± 0.1 mm) and aluminium (thickness = 16.5 ± 0.1 mm) was carried out using the experimental setup described in section 5.5, and presented in figure 5.15. The PE-EMAT was positioned over a sample, and the ultrasonic signal measured on the oscilloscope using signal averaging (16x) to obtain an improved signal-to-noise ratio. This was especially necessary with the aluminium sample, because the single shot signal-to-noise ratio (SNR) was 5.6 dB. However, this is generally not required for operation on the steel sample, where the single shot SNR is 12.2 dB.

For the steel sample (see figure 5.19(a)), consecutive back-wall echoes with a temporal separation of 12.144 ± 0.001 μs, correspond to shear waves, having a velocity

of 3244 ± 33 m/s; which is in accordance with the typical shear wave velocity in mild steel 3235 m/s[7]. For the aluminium sample (see figure 5.19(b)), consecutive back-wall echoes with a temporal separation of 10.412 ± 0.001 μs, correspond to shear waves having a velocity of 3169 ± 38 m/s; which again is in accordance with the typical shear wave velocity in aluminium 3111 m/s[7].

From the comparison of these measurements, it is evident that the PE-EMAT system has better performance on low carbon steel to that obtained on aluminium samples. In fact, the first back-wall echo is approximately ten times bigger in steel than in aluminium (see comparison in figure 5.19). This result is explained in terms of the significantly higher bias magnetic field that is obtained when the PE-EMAT system is operating in a ferromagnetic sample such as low carbon steel, as was shown by experimental measurements in section 5.4 and confirmed by finite element simulations carried out in Comsol Multiphysics 3.5a shown in section 5.10.

Another interesting feature that is worth mentioning in this comparison is that regarding to the attenuation of the ultrasonic wave in the aforementioned samples. It is well known that in polycrystalline metals and alloys the ultrasonic attenuation is mainly determined by the grain structure[8]. Because steel has very complicated microstructures depending on alloying elements, heat-treatment, and rolling process, it is expected to have higher attenuation than aluminium. In order to verify this, the attenuation in both samples was estimated by observing the amplitude decay in two consecutive back-wall echoes (first and second in this case), and using the following equation:

$$\alpha_{dB/m} = (\frac{1}{x})(20log\frac{A_1}{A_2}) \tag{5.1}$$

where x is the distance travelled; which in this case is twice the sample thickness since the PE-EMAT system is operating in pulse-echo mode, thus it is 39.4 mm

and 33 mm for the steel and aluminium samples, respectively. A_1 and A_2 are the amplitudes of the first and second back-wall echoes, respectively (both measured as shown in figure 5.17. The results of the calculation show that the attenuation is 138.8 ± 0.7 dB/m for the steel sample, and 115.5 ± 0.7 dB/m for the aluminium sample. Based on these results, it is then important to note that even with higher attenuation in the steel sample, the first back wall echo is still bigger than the one obtained in the aluminium sample, as can be seen in figure 5.20.

5.8 Effect of an oxide layer

As stated in section 3.4, for a normal bias field EMAT operating on steel samples such as low tensile carbon steel, mild steel and cast irons, the Lorentz force contribution is the dominant transduction mechanism over magnetostriction [3]; which would never be larger than 5-10% [9]. The magnetostrictive contribution to the efficiency of the EMAT system would be higher only in the presence of a highly magnetostrictive layer adhered to the steel sample surface.

Oxide layers, such as magnetite (Fe_3O_4, one of several iron oxides grown in a reducing high temperature environment), enhance the signal amplitude when compared to that obtained in a "clean", bare metal surface. The enhancement depends on the degree of adhesion of the layer upon the surface, its thickness and its temperature. In fact, if the layer is poorly adhered to the metal surface, any acoustic energy will remain trapped in the layer and will not be transmitted to the metal, and if the magnetite scale is above its Curie point (550 °C), the amplitude enhancement will cease to exist [10]. In addition, it has been reported that there is an optimum thickness of this oxide layer to enhance the ultrasound transduction, typically up to 1 mm thick [11].

Figure 5.21 shows two ultrasound waveforms obtained using the PE-EMAT in the

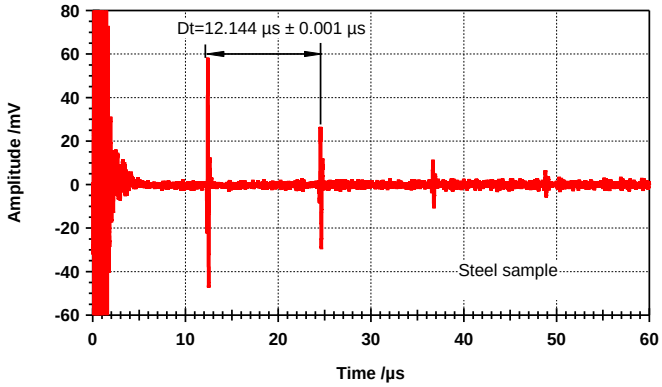

(a) Steel.

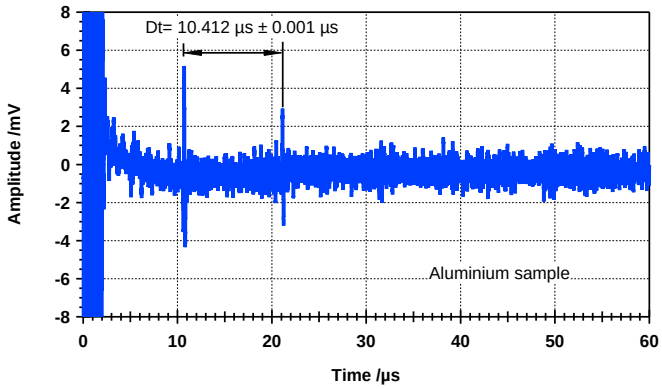

(b) Aluminium.

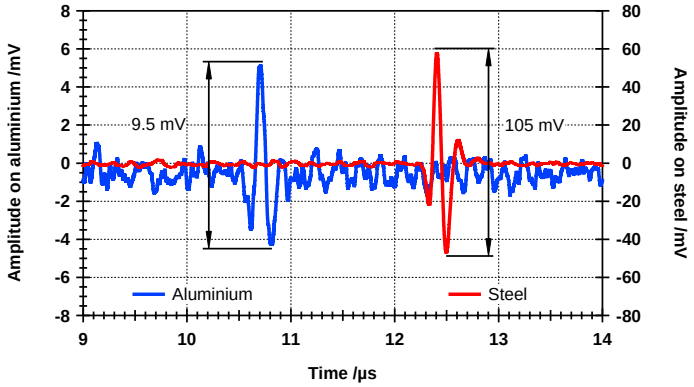

(c) First back-wall echo obtained for each sample.

Figure 5.19: Performance of the PE-EMAT system on (a) steel, and (b) aluminium; showing in each case a series of back-wall echoes of the ultrasonic signal. In the comparison (c) it should be noted that the signal amplitude is approximately ten times bigger in steel than in aluminium.

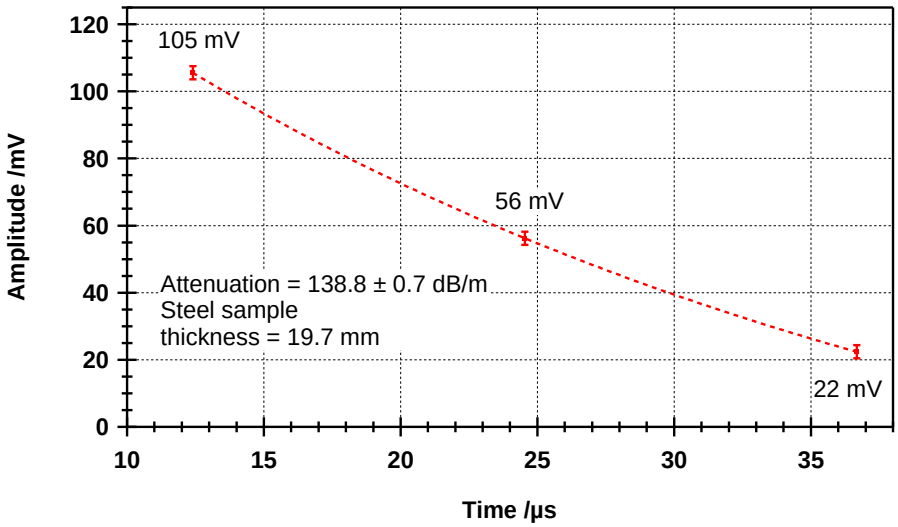

(a) Attenuation on steel.

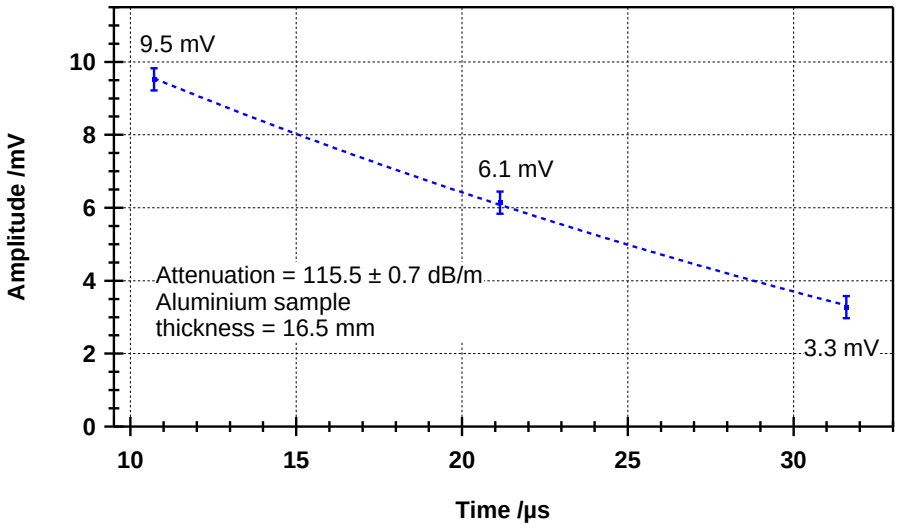

(b) Attenuation on aluminium.

Figure 5.20: Ultrasonic signal attenuation in (a) steel and (b) aluminium; showing in each case the amplitude reduction of three consecutive back-wall echoes. From this comparison it should be noted that even with higher attenuation in the steel sample, the first back-wall echo is still bigger than the one obtained in the aluminium sample.

same low carbon steel sample. The waveform in the top of the graph (red solid line), shows the first back-wall echo in a region of the sample which is free of magnetite; whereas the waveform in the bottom (blue solid line), shows the effect of a well adhered magnetite layer ($\approx$ few microns) on the sample surface. As can be seen, the amplitude of the ultrasonic signal in the presence of the magnetite layer increases considerably, and a 7.5 dB improvement in the amplitude of the first back-wall echo is achieved in this particular case.

5.9 Lift-off performance

The lift-off dependence is an important practical characteristic of EMATs, and depending on whether the transducer is operating as generator or detector of ultrasound, the factors that contribute to the lift-off dependence are different. On generation, there are two factors to take into account: a reduction of the bias magnetic field as the gap is increased, and a lower current density induction into the sample as the coil is further from the surface. On detection, again the reduction of the bias magnetic field has an effect, and since the coil is further away from the eddy current in the sample surface, there is a reduction of the induced e.m.f. in the coil, due to the decrease in magnetic field from the eddy current.

In order to demonstrate the lift-off performance of the PE-EMAT system a set of measurements were carried out on a low carbon steel sample using the experimental setup described in section 5.5, and presented in figure 5.15, except for the variation of the EMAT/sample separation (see figure 5.22(a)). The first part of this experiment was performed with the transducer in direct contact with the sample surface (lift-off equal to "zero"). The second part was carried out at four different EMAT/sample separations: 0.5, 1.0, 1.5 and 2.0 $\pm$ 0.01 mm. For each condition, the ultrasonic signal was recorded in the oscilloscope using signal averaging (16x)

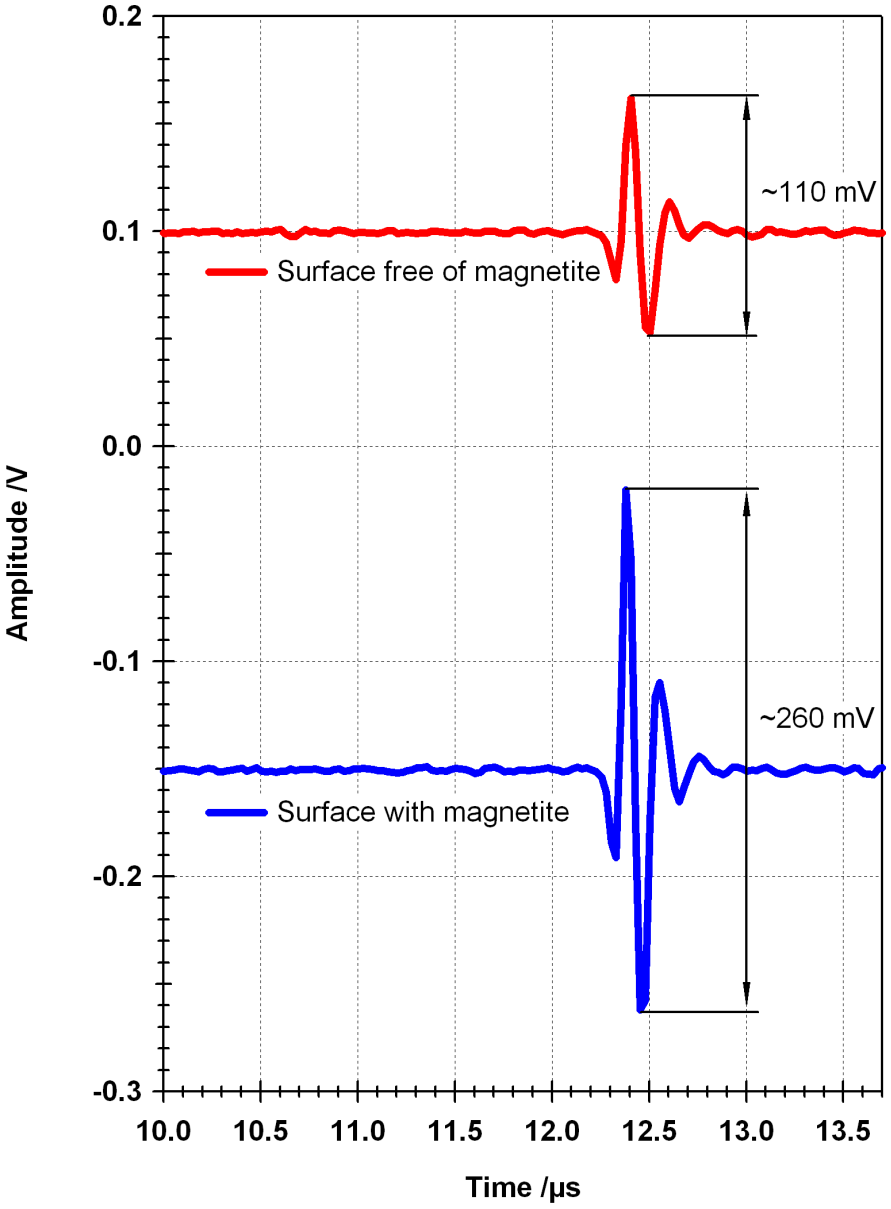

Figure 5.21: The graph above shows the effect in the ultrasonic signal amplitude when the PE-EMAT system is operating on a low carbon steel sample: free of magnetite (top), and with a magnetite layer adhered to the sample surface (bottom).

to improve signal-to-noise ratio; which was especially necessary for larger lift-offs. Figure 5.22(b) shows the results of these experiments on the steel sample and, consequently, the effect of lift-off on the ultrasonic signal output. As can be seen, small changes in lift-off distance can greatly affect the signal amplitude. The drop in amplitude with an increase in the EMAT/sample separation is exponential, as theory predicts (see section 3.2). The experimental points were fitted empirically to an exponential function of the form: $y = y_0 + A * exp^{(-b*x)}$, where x is the peak amplitude, b (1.41 $\pm$ 0.07) the decay factor , y_0 (0.005 $\pm$ 0.002) and A (0.101 $\pm$ 0.002) are constants. The measured decay for this PE-EMAT system is about $\approx$ 10 dB/mm.

In order to give a point of comparison and a perspective of the lift-off performance of the PE-EMAT system presented here, a similar experiment was carried out but using a permanent magnet (PM) EMAT of comparable characteristics concerning the coil (number of turns and wire diameter). The PM-EMAT used for this comparison is shown in figure 5.23, it is contained in a brass housing, it utilises a NdFeB magnet, producing a normal static magnetic field (512 mT when operating in the same steel sample) and a wire wound spiral coil (diameter = 13 mm, 18 turns, polymer film insulated copper wire (outer diameter = 0.36 mm)). In this configuration, the PM-EMAT generates and detects shear waves that are polarised in the radial direction, in the same manner as the PE-EMAT.

The results of the measurements show that, in a similar fashion as with the PE-EMAT system, the drop in amplitude with an increase in the EMAT/sample separation is exponential. The values for the empirical exponential fitted curve ($y = y_0 + A * exp^{(-b*x)}$), are: $y_0 = 0.002 \pm 0.001$, $A = 0.031 \pm 0.001$, and $b = 0.96 \pm 0.09$. The measured decay in this case is about $\approx$ 9 dB/mm.

A comparison on the lift-off performance of both transducers can be seen in figure 5.24. With similar amplitude decay factors per millimeter lift-off, the better per-

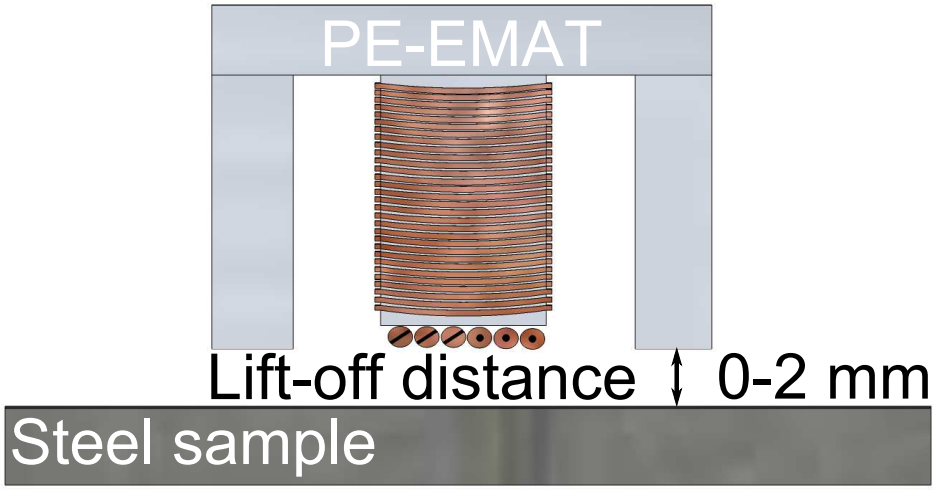

(a) The distance between the PE-EMAT and the sample was varied from 0 to 2 mm, with increments of 0.5 mm

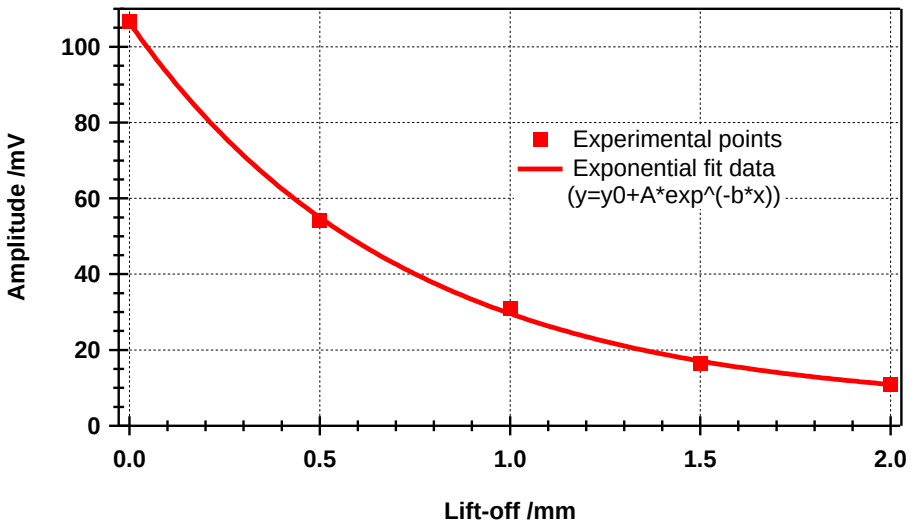

(b) Lift-off performance (PE-EMAT)

Figure 5.22: Lift-off dependence of the shear wave generated in a low carbon steel sample by the PE-EMAT. Fit to exponential function: $(y = y_0 + A * exp^{(-b*x)})$, where x is the lift-off, b (1.41 $\pm$ 0.07) the decay factor , and y_0 (0.005 $\pm$ 0.002) and A (0.101 $\pm$ 0.002) are constants.

formance of the PE-EMAT system is clear. The signal amplitude for the range of lift-off distances used is on average a factor of three larger for the PE-EMAT. This is especially important for "on-line" inspections, or situations in which is preferable not to have the transducer in direct contact with the sample, for instance, in high temperature applications since the transducer could avoid direct contact with the hot sample.

It should be noted that these measurements have been done maintaining the EMAT to sample separation constant. However, this is not always possible, and the separation between the transducer and the sample may not remain constant. This condition can be accounted for by measuring the inductance of the EMAT coil and using it to normalise any signal amplitude measurement. This requires calibration for the particular metal sample (inductance in the coil changes with the sample conductivity), and it is advantageous because it yields a measure of the lift-off which is independent of the acoustic measurement[12,13].

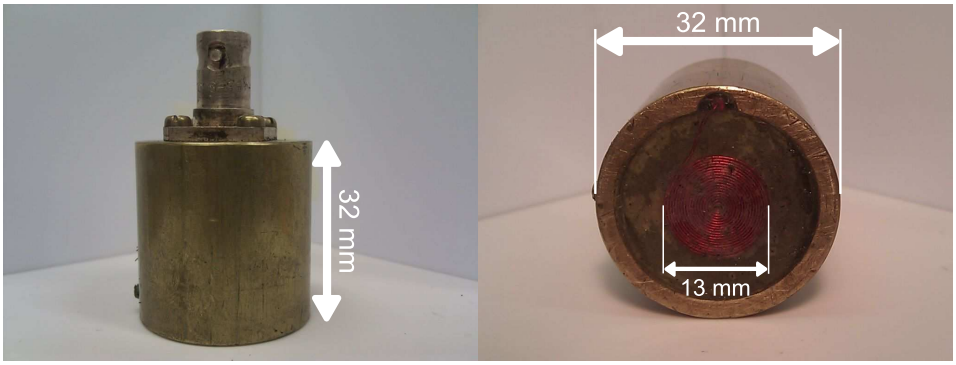

Figure 5.23: Photograph of the PM-EMAT used to have a point of comparison of the lift-off performance of the PE-EMAT system. Presented here are the lateral and bottom views with its correspondent dimensions.

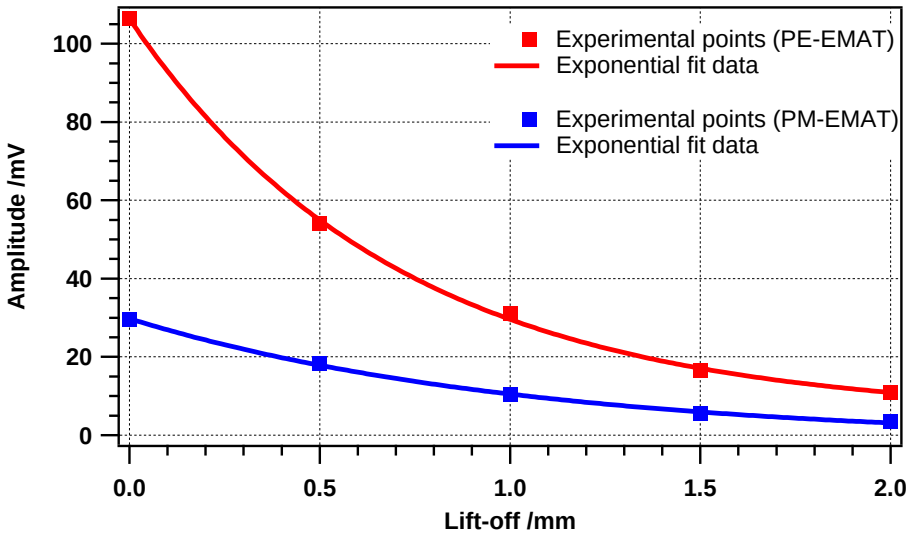

Figure 5.24: The above graph shows the lift-off dependence of the shear wave generated in a low carbon steel sample by the PE-EMAT and the PM-EMAT. The better performance of the PE-EMAT system is clear even at 2 mm away from the sample; where the signal amplitude is almost two times bigger than that obtained with the PM-EMAT. Note that the variable x in the equation represents the lift-off.

5.10 Magnetic field modelling

To compute and plot the magnetic behaviour of the electromagnet that provides the bias magnetic field for EMAT operation, a model was implemented in Comsol Multiphysics 3.5a. To make the computation viable on the hardware available, the approximation of just modelling the central leg of the electromagnet and the energising coil was undertaken. This takes advantage of the 2D-Axial symmetry mode available in the AC/DC module of the aforementioned software. It is acknowledged that this assumption limits the model in the sense that it takes no account of the return magnetic path that provides the original E-shape of the core. However, it is a good representation of the flux density in the region where the EMAT coil is located.

The modelling plane is the rz-plane; the horizontal axis represents the r-axis, and the vertical axis represents the z axis. The schematic diagram used in the simula-

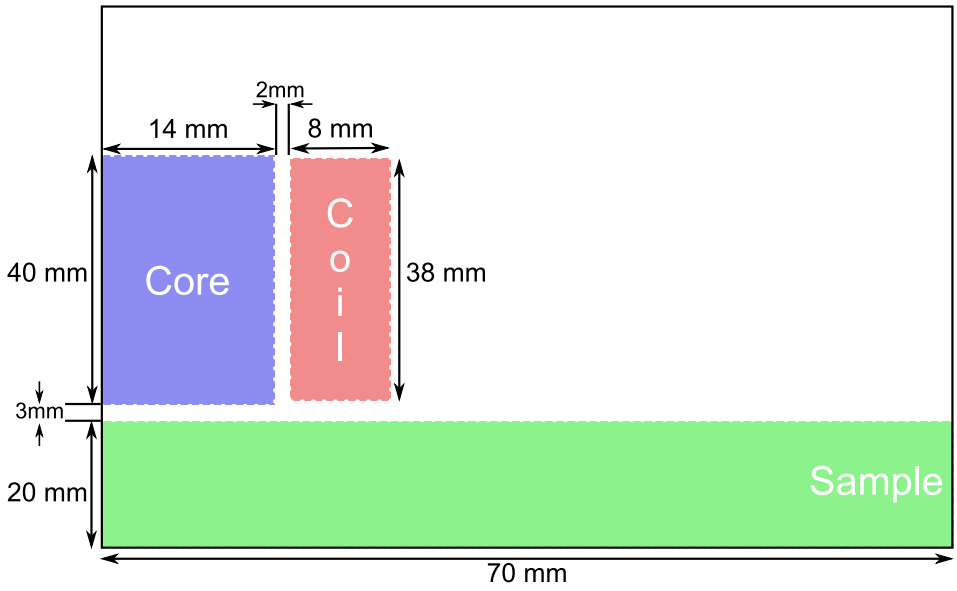

(a) 2D-axial geometry

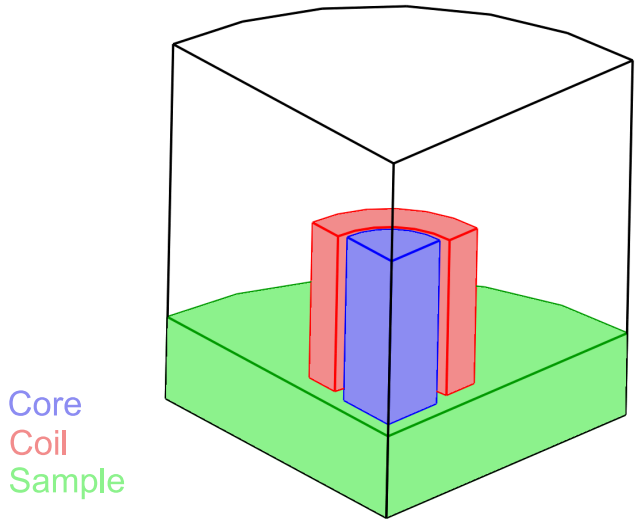

(b) 3D geometry

Figure 5.25: Schematic diagram of the model used in the simulation, and the 3D geometry, obtained by revolving (90°) the 2D geometry about the z-axis.

tion, and the 3D geometry obtained by revolving (90°) the 2D geometry about the z-axis, are shown in figure 5.25.

The model represents the central leg as a cylinder (14 mm radius x 40 mm height). The magnetic material employed for the core was soft iron, which is available from the material properties library in the software. Since the energising coil has a large number of turns, it would be not efficient to model each turn as a separate wire. Instead, the model treats the coil as a single turn (8 mm width x 38 mm height) with a constant external current density; which is defined by the number of turns in the coil, and the peak current measured experimentally from the current monitor resistor in the electromagnet driver circuit (15 A for the aluminium sample, and 21 A for the steel sample, see section 5.2 for details on these measurements).

The electromagnet is placed over a metallic sample represented as a cylinder (70 mm radius x 20 mm height), which can be either aluminium or steel. The electrical conductivity and relative magnetic permeability in the case of the aluminium sample were set to be: 3.802×10^7 S/m and 1, respectively. For the steel sample, the electrical conductivity was 5.882×10^6 S/m, and the magnetic relative permeability, being dependent on factors such as: composition, structure, frequency and applied magnetic field strength; it was decided to use an arbitrary and constant value of 100. All the elements are surrounded by air, and the magnetic insulation condition was considered for all outer boundaries of the simulation region; which is required to represent an infinite simulation volume.

A surface plot representing the z component of the flux density when the electromagnet is placed over steel and aluminium samples, is shown in figures 5.26(a) and 5.26(b), respectively. Examining these figures, it is clear that the flux density in the region in which the EMAT coil would be located (radial position from 0 to 6.1 mm) is lower in the case of the aluminium sample, as it would be expected because of its paramagnetic nature. A line plot along the radial position (0 to 20 mm) for each

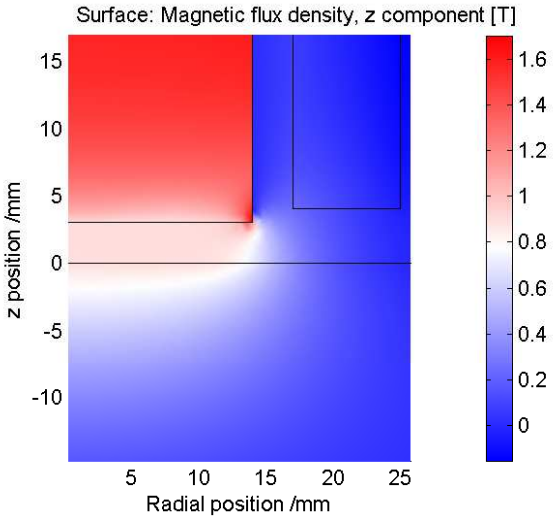

(a) Steel sample

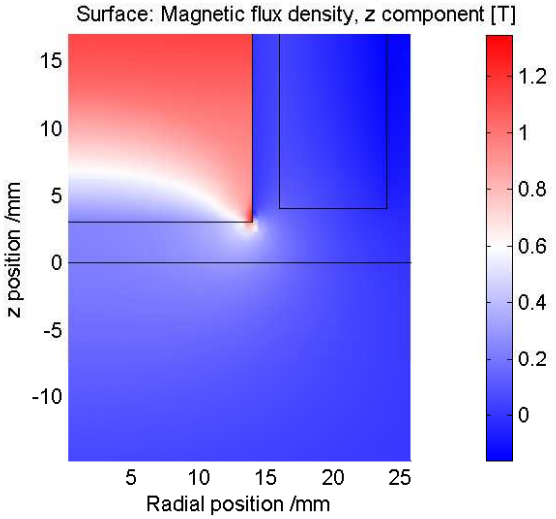

(b) Aluminium sample

Figure 5.26: Results from the simulations in Comsol, showing in each case a surface plot representing the flux density (z component) when the electromagnet is placed over: steel (top) and aluminium (bottom).

sample, representing the profile of the magnetic flux in the z direction can be seen in figure 5.27. In the results from the simulations, the flux density was higher in the steel sample when compared to that obtained in the aluminium sample (891 mT vs 218 mT), as was shown experimentally for the E-shaped core in section 5.4.

Considering the same geometry for the model and characteristics of the elements mentioned earlier, a set of simulations were done in order to investigate the variation of the flux density with increasing the distance between the electromagnet and the steel sample. A set of line plots along the radial position (0 to 20 mm), representing the profile of the magnetic flux in the z direction for different lift-off positions (0-2 mm, with 0.5 mm increments), is shown in figure 5.28. As can be seen in this figure, there is a reduction in the magnitude of the flux density as the lift-off is increased. This reduction, together with the decrease in current density at the sample surface induced by the EMAT coil (see section 5.11), will contribute to the decay in the ultrasonic signal amplitude (≈10 dB/mm) as shown in section 5.9.

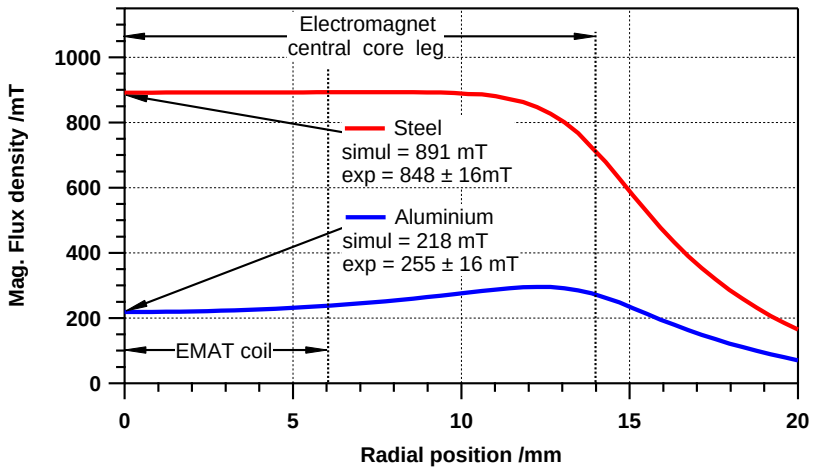

Figure 5.27: The above graph shows the results from the simulation in Comsol, showing a line plot of the flux density (z component) measured on the surface of each sample (z=0 mm, r=0 - 20 mm), and displaying the extent of the EMAT coil and electromagnet central core leg.

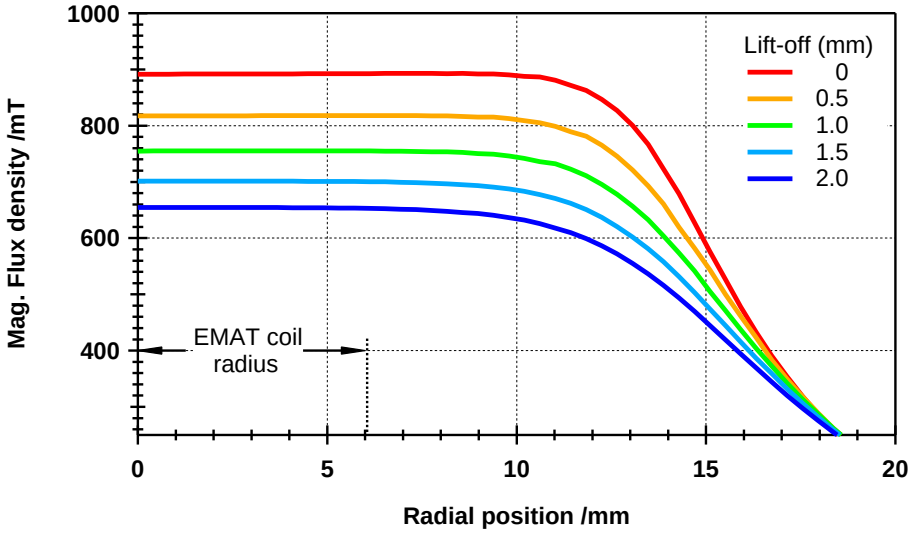

Figure 5.28: The above graph shows the results from the simulation in Comsol, showing flux density (z component) profiles across the EMAT coil radius for a number of different lift-off positions (0-2 mm).

5.11 Image current modelling

As was mentioned in section 3.2, the first step to couple electromagnetically an EMAT to a conducting sample is injecting an alternating current through its coil. The current density induced in the sample is concentrated in the upper surface and decreases exponentially with depth. The skin depth or depth of penetration, by definition is the depth at which the current density is attenuated by $1/e$ ($\approx 37\%$ or -8.7 dB)[14], and depends on the frequency of the current, the properties of the conducting sample, its conductivity or resistivity and its permeability, and coil geometry and lift-off.

In order to compute and plot this effect, and to quantify the current density induced by the spiral coil of the PE-EMAT system presented in this body of work, a model was implemented in Comsol Multiphysics 3.5a, using the 2D-Axial symmetry mode available in the AC/DC module with the time-harmonic formulation; which assumes that all variations in time occur as sinusoidal signals.

Material	Conductivity (σ [S/m])	Relative permeability (μ_r)
Aluminium	3.802x10^7	1
Steel	5.882x10^6	100
Copper	5.998x10^7	1

Table 5.1: Properties of the materials employed in the model implemented in Comsol to compute and plot the current density induced by the spiral coil of the PE-EMAT system.

Due to the symmetry of the situation, just half of the coil is necessary in the model. Therefore, the coil has a 6.1 mm radius, each turn in the coil (18 turns in total) has a 0.3 mm diameter, and is separated from the sample by 0.25 mm (lift-off due to the protective face of the coil). The sample is represented as a cylinder of radius 7 mm and height 0.18 mm. The depth was selected to ensure that the current density has attenuated completely, thus is more than three times the maximum skin depth to model; which corresponds to the aluminium sample (3*d= 0.114 mm).

The sample is either aluminium or steel, and the coil is considered to be copper; their material properties are presented in table 5.1. The current in the coil was considered to have a magnitude of 45 A and it is assumed a single frequency of 4.5 MHz; which is selected because the frequency spectrum of the generation current measured experimentally is centred around that frequency (see section 5.3). The schematic diagram of the model used in the simulation, and the 3D geometry obtained by revolving (90°) the 2D geometry about the z-axis, are shown in figure 5.29.

The results obtained from the simulation in both samples are shown in figure 5.30. As can be seen, in both cases the current density decreases exponentially, as theory predicts. For the steel sample, the magnitude of the current density at the surface is 4.66x10^7 Am^{-2}, and at a depth equal to the skin depth (d= 0.98x10^{-5} m) has decreased to 1.66x10^7 Am^{-2}; which represents a reduction of $\approx$ 36.8%. Whereas for

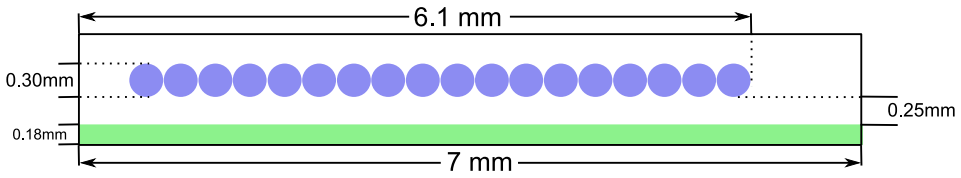

(a) 2D-axial geometry

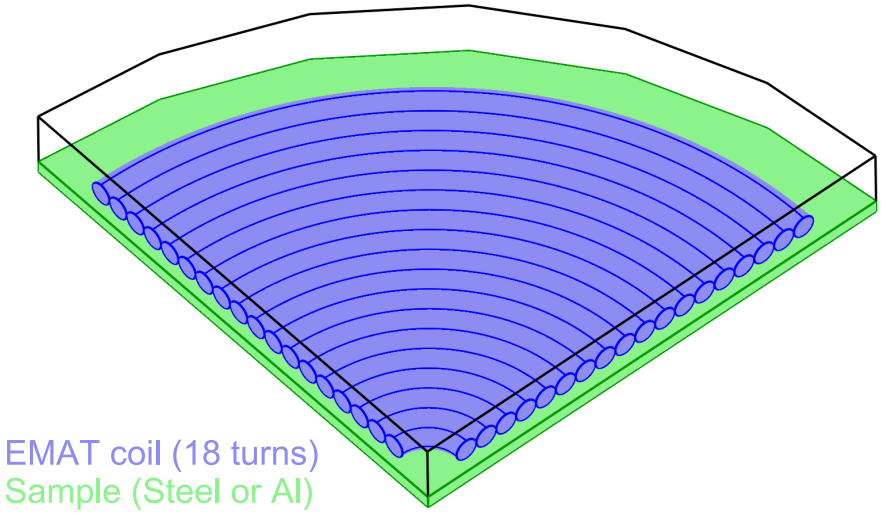

(b) 3D geometry

Figure 5.29: Schematic diagram of the model used in the simulation of the induced current density by the EMAT coil in different samples, and the 3D geometry obtained by revolving 90° the 2D geometry about the z-axis.

the aluminium sample the current density at the surface is 3.57x10^7 Am^{-2}, and at a depth equal to the skin depth (d= 0.38x10^{-4} m), has decreased to 1.26x10^7 Am^{-2}; which represents a reduction of 35.7%.

Another interesting feature that can be obtained from the simulation is the variation of the dynamic field when the gap between the coil and the sample is increased. As was mentioned in section 5.9, the ultrasonic signal amplitude will decrease with increased lift-off, as both the bias and dynamic fields at the surface of the sample will decrease. In the previous section it was shown how the bias field would decrease when the gap between the sample and the electromagnet has been increased (891 mT at z=0 mm, 655 mT at 2.0 mm, see figure 5.28). In figure 5.31, the variation of

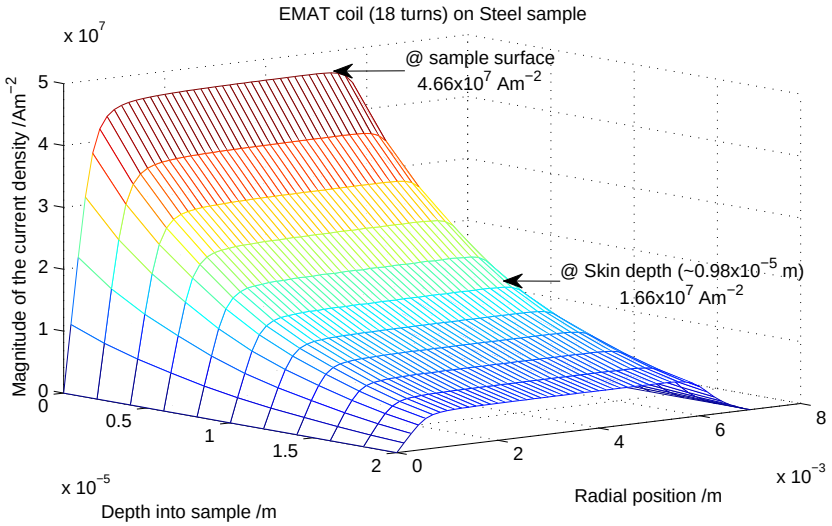

(a) Steel

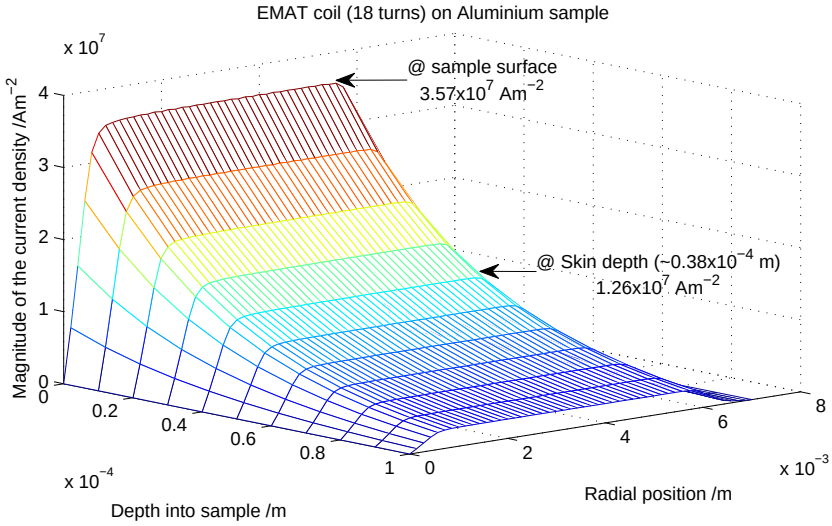

(b) Aluminium

Figure 5.30: Induced current density decay in steel and aluminium samples by the generation current flowing in the EMAT coil; which were obtained from the simulation in Comsol. Note the order of magnitude difference on the "Depth into sample" axes on the above plots.

the dynamic field obtained from the simulations in Comsol is presented. In a similar fashion as with the bias field, the magnitude of the dynamic field decreases with lift-off. Another interesting feature that is shown in figure 5.31, is that increasing the lift-off would have the effect of making a point in the coil more sensitive between the centre and the edge. For instance, the profile of the dynamic field for a lift-off of 2 mm shows that the coil would be more sensitive between a radial position of 3-4 mm.

In absolute terms, the coil will be less sensitive for increased lift-off, and it is worth noting that the coil will always have some degree of lif-off via a protection face; which can be an epoxy resin layer for EMAT coils working at room temperature, or a ceramic plate for those working at higher temperatures.

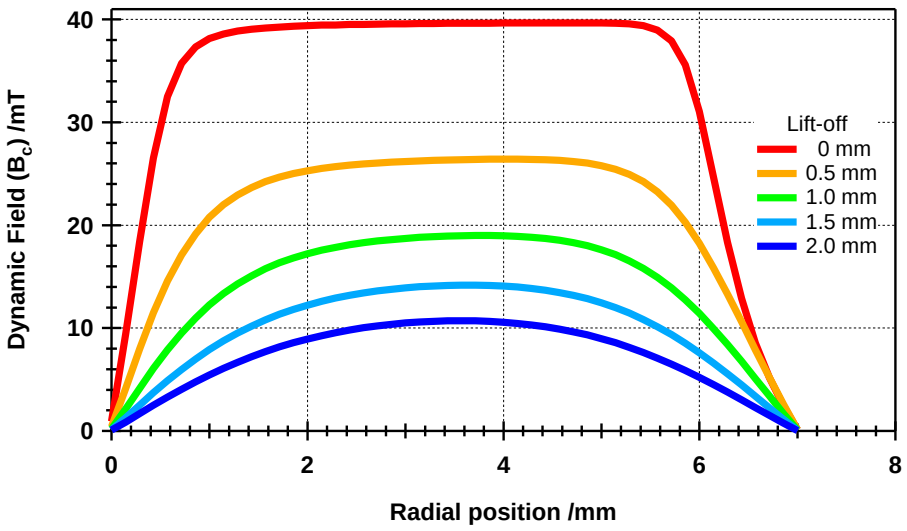

Figure 5.31: Dynamic magnetic field profiles across the EMAT coil radius for a number of different lift-off positions, when considering the steel sample. The results were obtained from the FE simulation in Comsol.

5.12 Ultrasonic propagation modelling

A commercial software package (PZFlex) is used to produce the transient, finite element model to analyse and validate the propagation of the ultrasonic waves generated/detected by the PE-EMAT system presented in this body of work.

The first step to construct the model in this software is to define the conditions that have to be taken into account in the simulation, such as: geometry and material properties of the sample, element size, a suitable pressure load to generate the ultrasound, and boundary conditions.

In line with the experimental geometry, the sample used in the model is 100 mm wide and 20 mm deep, and is considered to be steel with the following material properties: a density of 7900 kg/m^3, a longitudinal wave velocity of 5960 m/s that has an attenuation of 0.3 dB/cm at 1 MHz, and a shear wave velocity of 3235 m/s that has an attenuation of 1.2 dB/cm at 1 MHz.

Once the geometry of the model and the relevant material properties have been defined, it is necessary to determine the pressure load that will generate the ultrasound in the model. The frequency content of the generation current in the coil of the PE-EMAT system is centred around 4.5 MHz as was shown in section 5.3. The simulated pressure load is designed to have similar characteristics and consists of two complete cycles of a 4.5 MHz cosine wave multiplied by a symmetric Hann window. The pressure load and its frequency spectrum are shown in figure 5.32(a) and 5.32(b), respectively.

PZFlex works by breaking the model up into smaller blocks (or elements). Defining the frequency and velocity of interest (9 MHz and 3235 m/s), one can determine the minimum wavelength (360 μm) and therefore set the size of the element (10 μm, calculated using 20 elements per wavelength) that ensures the model converges to an accurate solution. This was verified by increasing the number of elements per

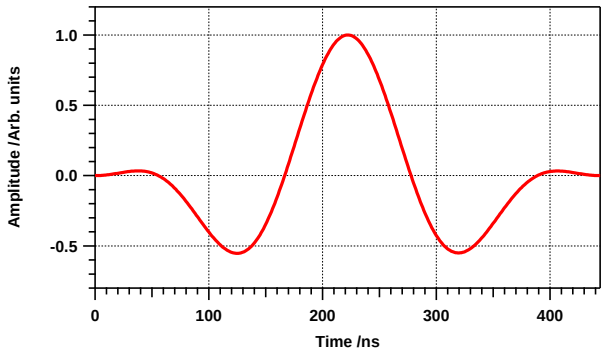

(a) Pressure load

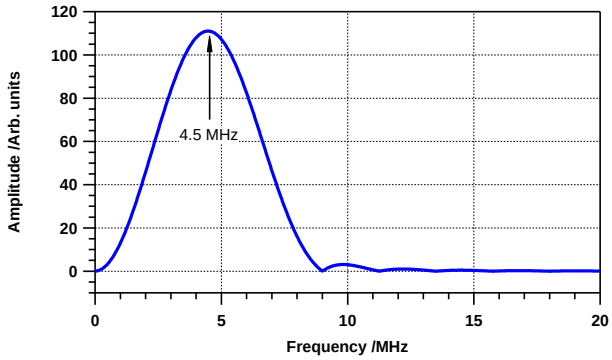

(b) Frequency spectrum

Figure 5.32: The above graphs show the simulated pressure load which was used as input in the model implemented in PZFlex, and its frequency spectrum. Note that the maximum frequency of interest in the simulation was defined as 9 MHz.

wavelength by 50% and observing no significant differences in the simulated waveforms.

The pressure load is applied in the x direction (parallel to the sample surface) in the form of a line segment, over the region equivalent to 611 elements; which in turn corresponds to the radius of the actual EMAT coil (6.1 mm). Applying this pressure load to the surface results in the generation of mainly shear waves, but longitudinal waves will also be generated at the edges of the applied pressure load.

The upper and bottom sides of the model are set to be free boundaries. The right hand side of the model is set to be an absorbing boundary; which is needed to elim-

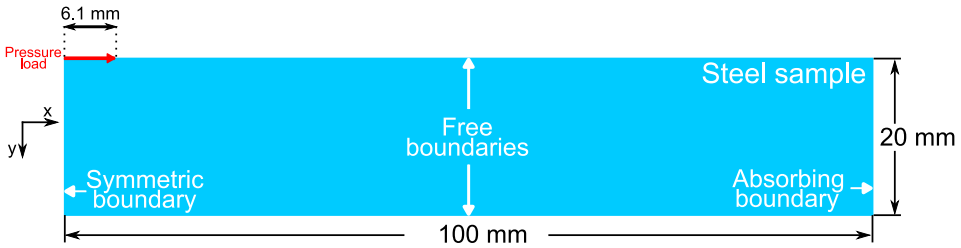

Figure 5.33: Schematic diagram of the model used in PZFlex to simulate the propagation of the ultrasonic waves generated/detected by the PE-EMAT system. Note that the region in which the transient pressure load is applied is marked in red and its dimension corresponds to the radius of the actual EMAT coil.

inate any reflections so that the initial, generated ultrasonic waves are observed. Finally, the left hand side of the model is set to be a symmetrical boundary. Figure 5.33 shows a schematic diagram of the model used in the simulation.

PZFlex is a time-domain solver, and as such generates its results as a set of time histories. The element velocity is the default output for the software; which is in itself an advantage, because EMATs are in fact velocity sensors (as was shown in 3.5). Thus the simulation is not slowed with extra calculations.

A series of images showing the element x-velocity in the steel sample is shown in figure 5.34 for different times (2, 4 and 6 μs) after the generating shear force is applied. In this figure, the shear wave travelling through the sample thickness can be observed, together with longitudinal and mode converted waves. The complete image sequence (from 1 to 14μs, time-step= 1μs) is available as a video file in Appendix A.1. Additionally, an A-scan obtained from the simulation is shown in figure 5.35(a); which compares favourably with the A-scan found experimentally when the PE-EMAT system is operating on a steel sample 5.35(b). Note that in the simulated A-scan the first back-wall echo of the longitudinal, mode-converted and shear waves are also present. This is not the case in the experimental A-scan, because even other wave modes are present in the sample, the configuration of the PE-EMAT system is mainly sensitive to shear waves.

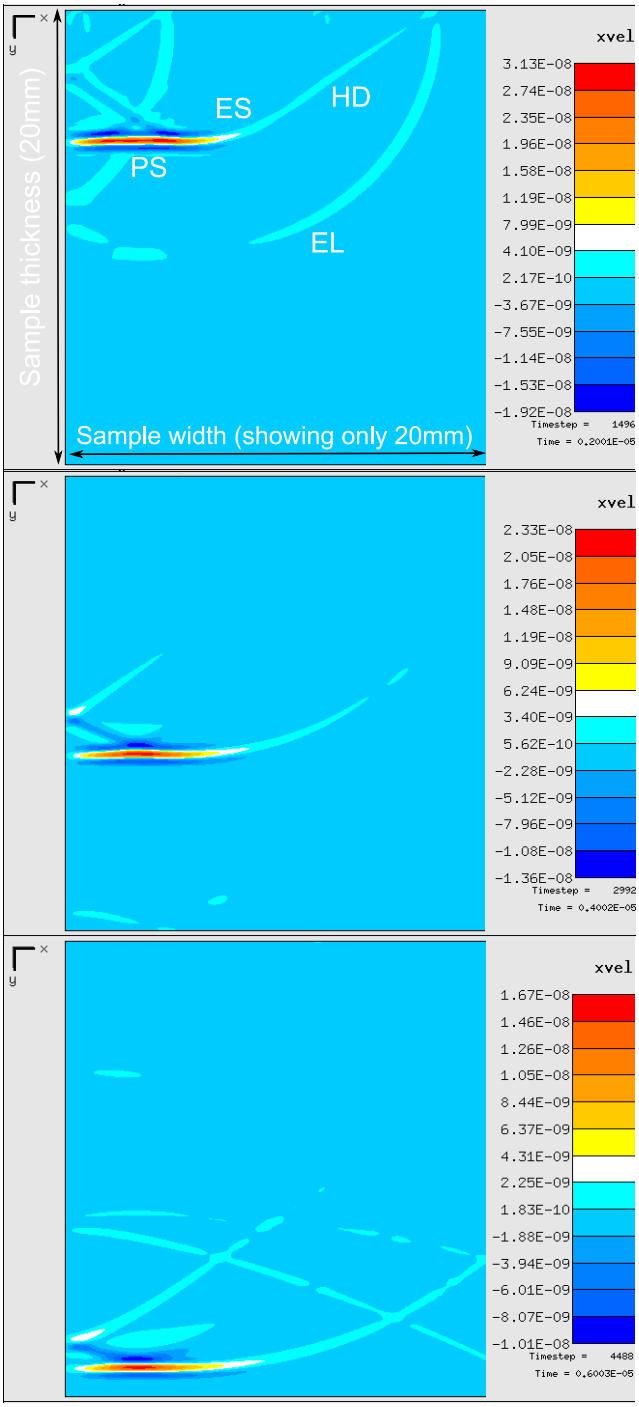

Figure 5.34: The above graphs show the element x-velocity taken at three different times: 2, 4 and 6 μs (top, centre, bottom, respectively). The plane shear wave (PS), edge shear wave (ES), head wave (HD), and edge longitudinal wave (EL), can be seen travelling through the sample thickness.

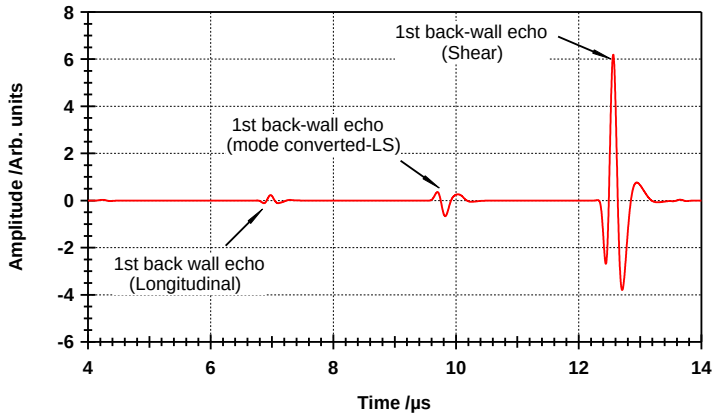

(a) Simulated A-scan

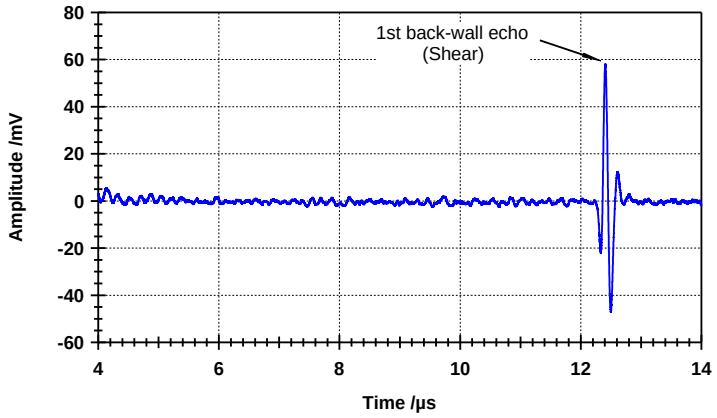

(b) Experimental A-scan

Figure 5.35: The upper graph (a) corresponds to the A-scan obtained from the simulation carried out in PZFlex; which shows the first back-wall echo of the longitudinal, mode-converted and shear waves. The lower graph (b) corresponds to the experimentally measured A-scan. Note that the configuration of the PE-EMAT system is mainly sensitive to shear waves, and that the generation current pulse discharged through the EMAT coil paralyses the detection circuitry for a finite time (≈ 2 μs).

5.13 Summary

The steps taken towards the development of the pulsed electromagnet (PE)-EMAT and the supporting electronics designed specifically to meet the requirements of the system at room temperature were presented in this chapter. Design considerations and operation description of all the elements that comprise the PE-EMAT system were shown.

Since it was important to ensure that the ultrasonic signal generated/detected by the PE-EMAT system is maximised, the precise synchronisation of the triggering time of the current pulser that drives the EMAT coil, with the time at which the bias field provided by the electromagnet has reached its maximum value, was determined and presented in the ultrasonic signal amplitude optimisation(see section 5.6). The performance of the PE-EMAT sytem was tested and reported in different sections of this chapter: generation/detection of shear waves in different media (aluminium and low carbon steel, see section 5.7); effect of an oxide layer adhered to the sample surface (see section 5.8); and lift-off dependence (see section 5.9).

From the comparison presented in 5.7, it was evident that the PE-EMAT system has better performance on low carbon steel to that obtained on aluminium samples. In fact, the first back-wall echo in the ultrasonic signal was approximately ten times bigger in steel than in aluminium (see comparison in figure 5.19). This result was explained in terms of the significantly higher bias magnetic field that was obtained when the PE-EMAT system was operating in the ferromagnetic sample, as was shown by experimental measurements in section 5.4 and confirmed by finite element simulations carried out in Comsol shown in section 5.10. Another interesting feature that is worth mentioning in this comparison is that even with higher attenuation in the steel sample, the first back wall echo is still bigger than the one obtained in the aluminium sample (see comparison in figure 5.20). Regarding the results presented

in section 5.8, it was clear that oxide layers, such as magnetite, enhance the signal amplitude when compared to that obtained in a "clean", bare metal surface. The presence of a magnetite layer lead to an enhancement of 7.5 dB in the amplitude of the first back-wall echo in the ultrasonic signal, for the particular case considered here (see comparison in figure 5.21).

Regarding the comparison presented in section 5.9, it was demonstrated that the PE-EMAT system has better lift-off performance when compare to that obtained using a permanent magnet EMAT of comparable characteristics (see comparison in figure 5.24). With similar decay factors per millimeter lift-off, the signal amplitude for the tested range of lift-off distances, was on average a factor of three larger with the PE-EMAT.

On a different note, the finite element simulations performed for the electromagnetic and ultrasonic analysis were reported in sections 5.10, 5.11, and 5.12. These included: the computation of the flux density produced by the electromagnet and its variation with lift-off (see section 5.10), the calculation and visualisation of the magnitude of the current density induced by an alternating current flowing in two different EMAT coil designs in non-magnetic and magnetic samples (see section 5.11); as well as the validation of the propagation of the ultrasonic wave generated/detected by the PE-EMAT (see section 5.12).

It is worth noting that the knowledge acquired in this chapter is essential and that it was employed to design and build a PE-EMAT system capable of withstanding high temperatures without the necessity of water cooling; which is presented in the following chapter.

References

[1] D. Jiles. *Introduction to magnetism and magnetic materials*. Chapman & Hall, 1991.

[2] W.T. McLyman. *Transformer and inductor design handbook*. Electrical and computer engineering. CRC Press, 2004.

[3] I.D. Kiteley. *A study of EMAT operation on ferromagnetic materials*. PhD thesis, University of Warwick, 1999.

[4] R.C. Alig. Direct electromagnetic generation of transverse acoustic waves in metals. *Physical Review*, 178(3):1050–1058, 1969.

[5] E.R. Dobbs. Electromagnetic generation of ultrasonic waves in metals. *Journal of Physics and Chemistry of Solids*, 31(8):1657–1667, 1970.

[6] H.L. Grubin. Direct electromagnetic generation of compressional waves in metals in static magnetic fields. *IEEE Transactions on sonics and ultrasonics*, 17 (4):227–228, 1970.

[7] G.W.C. Kaye and T.H. Laby. *Tables of physical and chemical constants*. Harlow-Longman, 16th edition, 1995.

[8] B. Ahn and S.S. Lee. Effect of microstructure of low carbon steels on ultrasonic

attenuation. *IEEE Transactions on Ultrasonics, Ferroelectrics and Frequency Control*, 47(3):620–629, 2000.

[9] R. Ribichini, F. Cegla, P.B. Nagy, and P. Cawley. Evaluation of electromagnetic acoustic transducer performance on steel materials. *Draft*, pages 1–12, 2010.

[10] I. Baillie. *The development of a laser-EMAT system suitable for on-line inspection in the continuous casting plant-Innovation report.* PhD thesis, University of Warwick, 2008.

[11] Md.S. Rohani. *The development of non-contact laser and EMAT ultrasound measurement systems for hot steel.* PhD thesis, University of Warwick, 1996.

[12] S. Dixon. *The analysis of aerospace adhesively bonded aluminium plates using electromagnetic acoustic transducers (EMATs).* PhD thesis, University of Warwick, 1994.

[13] J. Morrison, S. Dixon, M.D.G. Potter, and X. Jian. Lift-off compensation for improved accuracy in ultrasonic lamb wave velocity measurements using electromagnetic acoustic transducers (EMATs). *Ultrasonics*, 44:e1401–e1404, 2006.

[14] H.A. Wheeler. Formulas for the Skin Effect. *Proceedings of the IRE*, 30(30): 412–424, 1942.

Chapter 6

PE-EMAT design evolution. High temperature

6.1 EMAT coil for preliminary high temperature trials

The first trials above ambient temperature were performed using the EMAT coil mentioned in the previous chapter (see section 5.1 for more details). However, there were limitations on its use above specific temperatures, mainly because of the epoxy resin encapsulation and because of the polymer film insulation of the wire. Specifically, prolonged contact between the encapsulated EMAT coil and the sample at temperatures above ≈ 150 °C would result in irreparable damage to the epoxy encapsulation, because it would reach the glass transition temperature; which is often referred to as the temperature region in which a polymer goes from a glassy state to a rubbery state due to a change in the expansion coefficient and heat capacity [1]. Then, if the temperature goes above 200 °C, the damage would be irreversible to the EMAT coil because the polymer film insulation would melt [2].

Thus, with this in mind, the first target to accomplish was to have an EMAT coil capable of withstanding temperatures around 200 °C, without altering the original

coil design; which is worth bearing in mind was a wire wound spiral coil (diameter = 12.2 mm), consisting of 18 turns of a polymer film insulated copper wire (outer diameter = 0.36 mm), with an inductance of 1.6 μH and resistance of 0.1 Ω (measured with a Philips RCL meter, model PM6303 at 1kHz).

Previous work[3–5] in the ultrasonics group demonstrated that when working at elevated temperatures with water-cooled EMATs, a ceramic substrate is the best option to protect the EMAT coil and, at the same time, the front face of the magnet without significantly impairing the proper functioning of the transducer. Obviously, this protection should be kept as thin as possible to reduce the separation between the coil and the sample, since the EMAT efficiency diminishes exponentially with lift-off, as shown in sections 5.9 and 5.11.

Different types and thicknesses of ceramic substrates were tested by Baillie[6] to find the optimal to be used, and concluded that the best option was a 0.5 mm thick alumina sheet that could be machined to the required diameter. A similar ceramic substrate (ADS-96R, Coorstek Inc.) was utilised in this thesis, and some of its relevant material characteristics are shown in table 6.1. For more details the reader is referred to the thick film substrates design guide in[7].

The design of the water-cooled EMATs mentioned earlier, involved using non-flammable Kapton tape (polyimide film developed by Dupont^{TM}[8]) to protect the coil from heat and minor damage, and also involved using a high temperature epoxy adhesive for fixing the magnet, the protected EMAT coil and the alumina substrate together. The use of the Kapton tape and the epoxy adhesive was possible because the maximum temperature of the whole assembly was controlled by the water flow rate, always ensuring that the components' temperature does not exceed the maximum operating temperature. However, since the EMAT system proposed in this work does not have an active cooling system, an alternative method for fixing these elements to the electromagnet's central core leg was explored.

ADS-96R		
Characteristic	Unit	Value
Alumina content	Weigth %	96
Color	-	White
Density	g/cm^3	3.72
Average Grain Size	μm	4-7
Water absorption	%	NIL
Gas permeability	%	NIL
Coefficient of linear thermal expansion	$10^{-6}/^oC$	
25 - 200 ^oC		6.4
25 - 500 ^oC		7.3
25 - 800 ^oC		8.0
25 - 1000 ^oC		8.4

Table 6.1: Material characteristics of the alumina substrate used to protect the EMAT coil for high temperature applications.

High temperature ceramic adhesives are inorganic formulations for bonding ceramics, metals, quartz, graphites, textiles and composite materials used in processes and maintenance applications at harsh conditions. These adhesives exhibit high thermal and electrical resistance, and are an alternative to epoxies and other organic-based products.

Amongst a wide variety of options, Aremco's Ceramabond 835M was selected because it is an alumina-based high temperature adhesive which is non-flammable, contains no organic compounds, and is capable of bonding ceramic-to-ceramic and ceramic-to-metal. Some relevant characteristics of this ceramic adhesive such as: major constituent, temperature resistance, time for air set and heat cure, and color can be found in table 6.2. For more details on this ceramic adhesive the reader is referred to the technical bulletin available in [9].

Once the alumina ceramic substrate and the ceramic adhesive were selected, the assembly of the components was carried out, as follows: an alumina disc with diam-

Ceramabond 835M		
Characteristic	Unit	Value
Major constituent	-	Alumina
Maximum temperature	^{o}C	1650
Air set	hours	2
Heat cure	^{o}C - hours	93.3 - 2
Color	-	White

Table 6.2: Material characteristics of the ceramic adhesive used to fix the EMAT coil and the alumina ceramic substrate, to the electromagnet's central core leg.

eter of 25 mm is obtained by laser-cutting the alumina substrate sheet (50 mm x 50 mm x 0.5 mm), and bonded to the EMAT coil applying a layer of the alumina-based ceramic adhesive between them and covering the outer edges of the coil (allowing to air-dry and heat-cure as stated in table 6.2). Subsequently, these elements are placed into a mould in which is poured the required amount of ceramic adhesive to ensure a uniform encapsulation thickness of 2.9 mm. The ceramic encapsulated coil is removed from the mould after the correspondent air-drying process, and then placed on a hot plate heater for the heat-curing process; during which the ceramic encapsulated coil is flipped over from time to time so that both surfaces experience the heat treatment. Finally, the ceramic encapsulation is bonded to the centre pole of the electromagnet (using a similar procedure as described before with the ceramic adhesive), leaving the ceramic encapsulation and the other electromagnet poles lying in the same plane, and ready to be used. Photographs of three different steps in the ceramic encapsulation process of the EMAT coil for the preliminary high temperature trials, are shown in figure 6.1.

As would be expected, the main constraint in this version of ceramic encapsulated EMAT coil is the maximum temperature of operation of the wire polymer film insulation; which can melt if it is subjected continuously to a temperature above 200

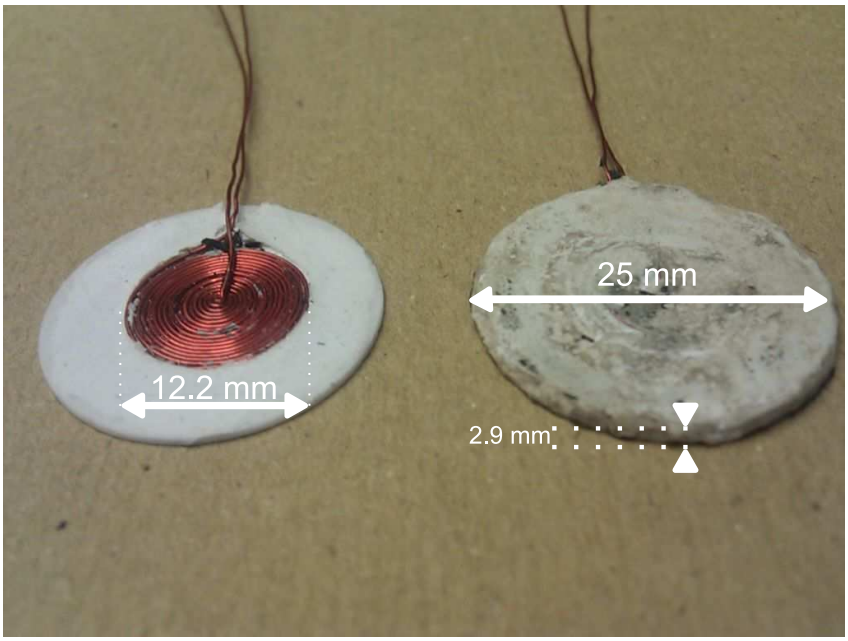

(a) On the left: Spiral coil bonded to the alumina ceramic substrate. On the right: Ceramic encapsulated spiral coil (upper view).

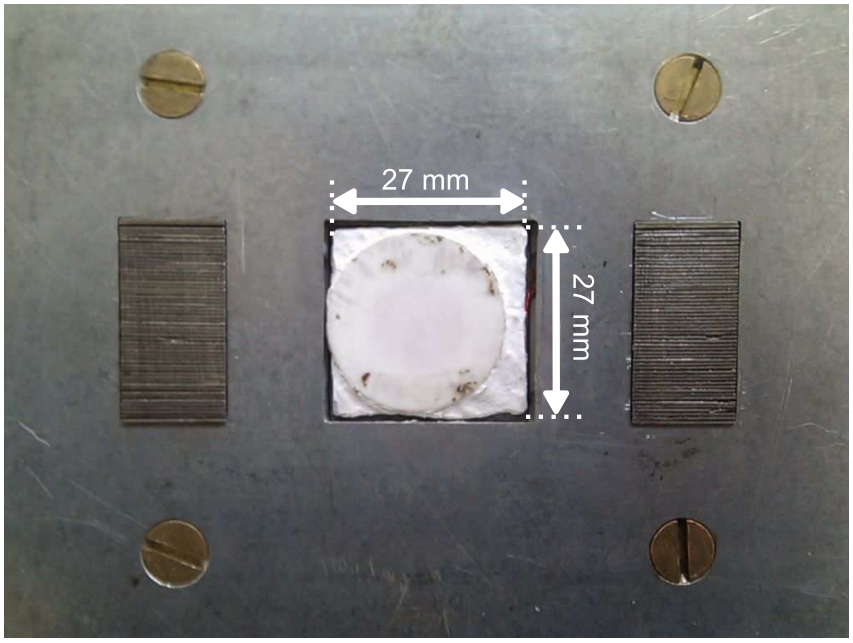

(b) Ceramic encapsulated coil bonded to the electromagnet core.

Figure 6.1: Photographs showing the steps taken to encapsulate the EMAT coil for high temperature trials.

Figure 6.2: Prolonged contact between the EMAT coil and the sample would result in irreparable damage to the coil, even when it is ceramically encapsulated and protected by an alumina ceramic plate. This is because the maximum operating temperature for the polymer film wire insulation is 200 °C.

°C, as it is shown in figure 6.2.

The experimental results of the PE-EMAT system composed by the first electromagnet used in the room temperature trials and this version of the ceramic encapsulated coil, operating on a low carbon steel sample are shown in subsection 6.4.1, and were already published in [10].

6.2 EMAT coil for final high temperature trials

An alternative design for the spiral coil was developed with the purpose of overcoming the coil's insulation constraint. The main idea behind the new design is that in order to avoid the use of a single insulated wire wound around itself in very tight turns, two bare copper wires can be tightly wound forming two concentric spiral coils with the same number of turns next to each other. Then, one of these wires is removed leaving behind a uniform gap that can be filled with the alumina-based high temperature ceramic adhesive; which would be acting as the wire insulator. Accordingly, it was decided that the diameter of the main wire was kept similar to

that from the previous coil, thus it is 0.315 mm; which is the closest diameter to the polymer film insulated copper wire. It is worth noting that the diameter of the wire that is to be removed should be smaller in order to reduce the gap between turns, and also to induce a larger image current within the sample surface; which in turn would give rise to a higher eddy current density and a larger signal amplitude. Thus, different wire diameters were tested and for practical reasons regarding the uniformity of the gap between turns, a feasible combination resulted in using a bare copper wire with a diameter of 0.27 mm.

As a consequence of having changed the EMAT coil design, a new optimisation process to determine the number of turns for this coil was carried out. For this purpose, various coils with different number of turns were tested and the best option regarding the signal amplitude resulted to be 18 turns. Additionally, it was necessary to implement a model in Comsol to quantify the induced current density within the sample surface and the dynamic magnetic field profile across the EMAT coil radius, in order to have a point of comparison with the previous design. The results from these simulations are shown in subsection 6.2.1 together with some comments on the comparison to the results obtained from the simulations in previous chapter.

The most important characteristics of the newer coil design can be summarised as follows: it consists of 18 turns of bare copper wire (diameter = 0.315 mm), with a uniform gap between turns of 0.27 mm. It has a diameter of 22 mm, with an inductance of 3.4 μH and resistance of 0.2 Ω (measured with a Philips RCL meter, model PM6303 at 1kHz).

The procedure of encapsulating the coil is exactly that described in the previous section, and as such is not pertinent to reproduce it here. However, a cross sectional diagram and a photograph of a ceramic encapsulated spaced spiral coil fabricated by such procedure can be seen in figure 6.3.

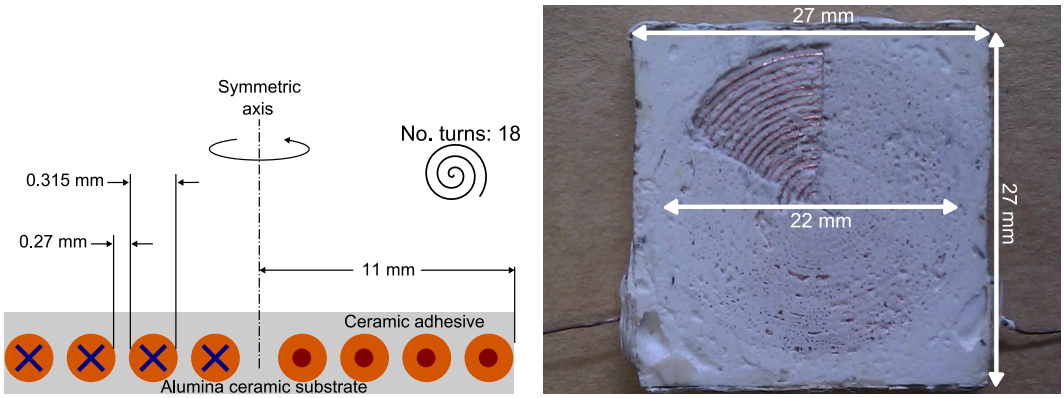

(a) Cross sectional diagram of the ceramic encapsulated spaced spiral coil.

(b) Photograph of the ceramic encapsulated spaced spiral coil (bottom view).

Figure 6.3: Details of the ceramic encapsulated spaced spiral coil. Note that in (b) the alumina ceramic substrate and part of the ceramic adhesive have been removed in order to observe the spaced spiral coil.

The experimental results of the PE-EMAT system composed by the electromagnet described in section 6.3 and this version of the ceramic encapsulated coil are shown in subsection 6.4.2, and were already published in[11].

6.2.1 Image current modelling

In order to quantify the current density induced by the spaced spiral coil, a model was implemented in Comsol Multiphysics 3.5a using the 2D-Axial symmetry mode available in the AC/DC module with the time-harmonic formulation; which assumes that all variations in time occur as sinusoidal signals. In a similar fashion as for the model employed for the previous coil design, due to the symmetry of the situation just half of the coil is necessary in the model. Therefore, the coil has a radius of 11 mm, each turn in the coil (18 turns in total) is 0.3 mm diameter, 0.27 mm gap in between turns, and 0.25 mm separation from the sample; which is an identical lift-off to that used in the simulation of the previous coil (see section 5.11).

The sample is represented as a cylinder of radius 14 mm and height 0.18 mm. Care was taken on selecting the depth of the sample to ensure that the current density has attenuated completely, thus is more than three times the maximum skin depth to model; which corresponds to 3*d= 0.03 mm.

The sample is considered to be steel, and the coil is considered to be copper; their material properties are those presented in table 5.1. The current in the coil was considered to have a magnitude of 45 A and it is assumed a single frequency of 4.5 MHz; which is selected because the frequency spectrum of the generation current measured experimentally is centred around that frequency (see section 5.3). The schematic diagram of the model used in the simulation, and the 3D geometry obtained by revolving (90^o) the 2D geometry about the z-axis, are shown in figure 6.4. The results obtained from the simulation in Comsol are shown in figure 6.5, and for comparison purposes the corresponding results for the preceding coil design have been included. As can be seen, the magnitude of the current density at the surface for the spaced spiral coil is $4.47\text{x}10^7$ Am^{-2}; which is smaller than the one obtained for the other coil ($4.66\text{x}10^7$ Am^{-2}). This was expected because of the difference in the coil diameter, and because of the fact that the turns in the newer coil are not tightly wound.

Another interesting feature that can be obtained from the simulation is the variation of the dynamic field when the lift-off is increased. As was mentioned in section 5.9 the ultrasonic signal amplitude will decrease with increased lift-off, since both the bias and dynamic fields at the surface of the sample will decrease. In section 5.10 it was shown how the bias field would decrease when the gap between the sample and the electromagnet has been increased from 0 mm to 2 mm (891 mT and 655 mT, respectively. See figure 5.28). With this in mind, a comparison on the variation of the dynamic field for both coils when the lift-off has been increased to 2 mm, was carried out in order to predict the lift-off performance of the newer coil design. The

results obtained from the simulations in Comsol suggest that the spaced spiral coil would have a similar lift-off performance to its predecessor. This is because in both cases one can assume that the bias field would remain the same, and although the dynamic field amplitude for the spaced spiral coil is slightly higher, as can be seen in figure 6.6, the difference is not significant.

As it was shown in section 5.11, in general terms, increasing the lift-off would have the effect of making a region in the coil more sensitive between the centre and the edge. This effect is also evident in figure 6.6, and it is worth noting that the spaced spiral coil has a wider region on which the coil would be sensitive at 2mm than that for the spiral coil.

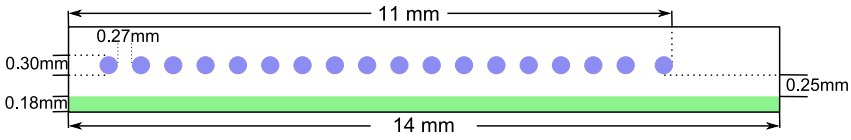

(a) 2D-axial geometry

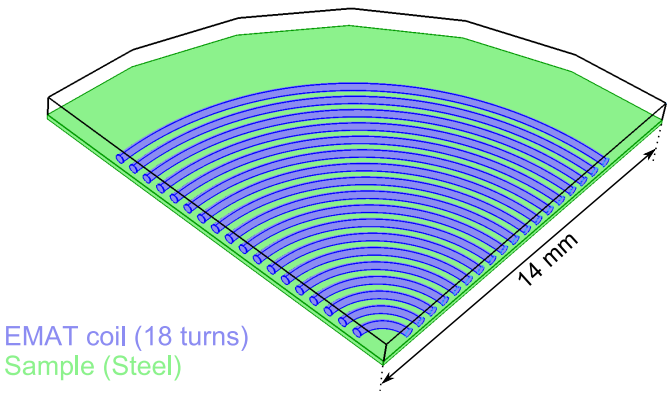

(b) 3D geometry

Figure 6.4: Schematic diagram of the model used in the simulation of the induced current density by the spaced spiral coil in a steel sample, and the 3D geometry obtained by revolving 90° the 2D geometry about the z-axis.

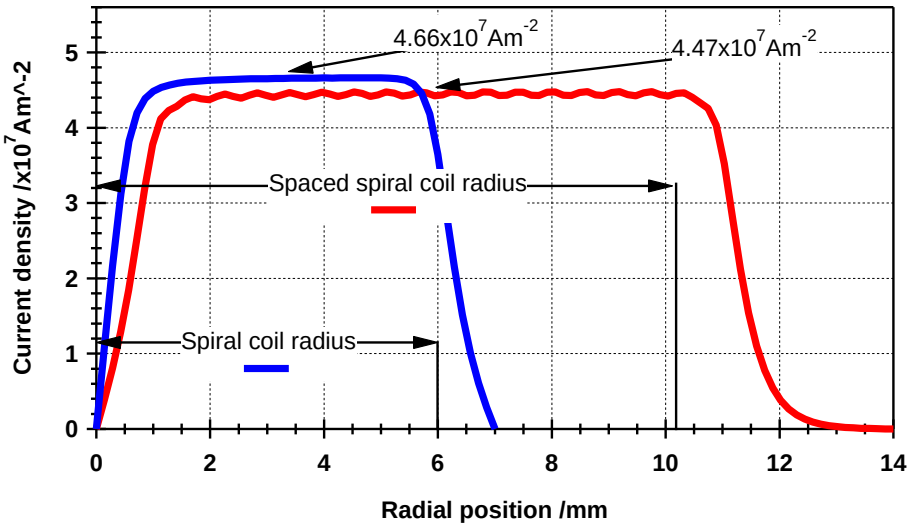

Figure 6.5: Results from the simulations in Comsol showing a comparison of the induced current density at the surface of a steel sample for both spiral coil designs.

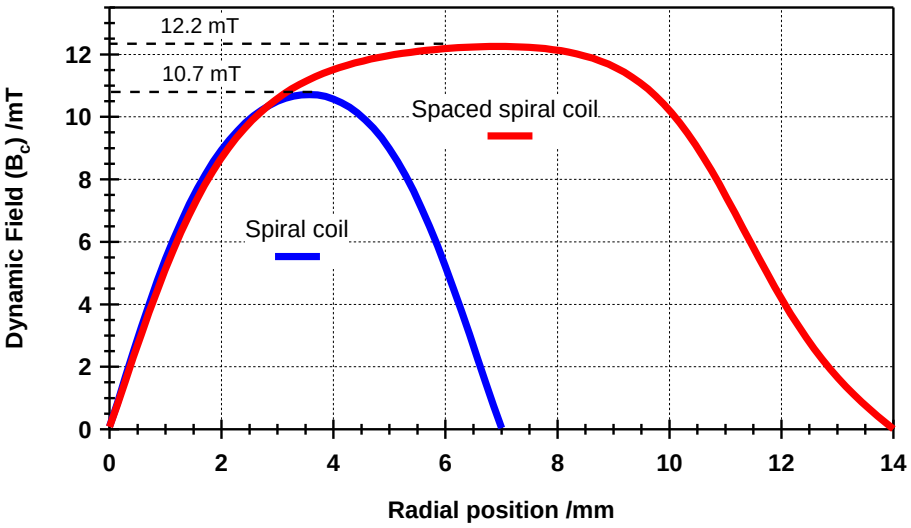

Figure 6.6: Results from the simulations in Comsol showing a comparison of the dynamic magnetic field profile across the EMAT coil radius for both coil designs, when considering a steel sample and a lift-off of 2 mm.

6.3 Pulsed electromagnet for high temperature trials

The first trials above ambient temperature were performed using the electromagnet presented in the previous chapter (see section 5.1 for more details). However, there were some restrictions on its use above specific temperatures. The plastic coil former made of PET polyester has a maximum operation temperature[12] of 200 °C, and the polymer film insulated in the energising coil can not be subjected to temperatures above 200 °C, as it was discussed in section 6.2. Thus, it was evident that alternative materials were needed to build an electromagnet capable of withstanding temperatures above the range of temperatures mentioned earlier.

The first step taken towards building the new electromagnet was to find a suitable material to be used for the coil former. Ceramic formulations were an obvious choice because they are inorganic and non-flammable materials, they can be used at elevated temperatures, and also they can be machined to the required shape. After reviewing commercially available options, it was clear that the glass ceramic MACOR, was an ideal candidate because it has essential attributes for the application, such as: maximum continuous operation temperature of 800 °C, it can be machined with ordinary metal working tools, it does not require post firing after machining process, and it is a useful high temperature insulator. Some other relevant properties of this material, are composition, density, and coefficient of thermal expansion, which are presented in table 6.3. The reader is referred to the technical specifications available in[13] for more details.

The second step taken towards building the new electromagnet was to find a wire with suitable insulation to wind the energising coil. It was found that silver, platinum, nickel and nickel-alloys wires (e.g. alumel, chromel, or kulgrid) are all used for applications at elevated temperatures[14]. Specifically, silver has good conductivity and can be used in the range of 400 to 500 °C in oxygen free environments. How-

MACOR. Machinable glass ceramic		
Characteristic	Unit	Value
Composition	%	
Fluorophlogopite mica		55
Borosilicate glass		45
Maximum temperature (continuous)	°C	800
Color	-	White
Density	g/cm^3	2.52
Coefficient of linear thermal expansion	$10^{-6}/°C$	
-200 - 25 °C		7.4
25 - 300 °C		9.3
25 - 600 °C		11.4
25 - 800 °C		12.6

Table 6.3: Material characteristics of the machinable ceramic used for the ceramic coil former, in which the electromagnet's energising coil is mounted.

ever, at temperatures above 500 °C, there are problems due to migration. Platinum can be used at temperatures above 600 °C, but it lacks general applicability mainly because of its expensiveness and also because of its very high resistivity ($\approx$ 6 times higher than that of annealed copper ($\approx$ 1.72x10^{-8} Ωm)[15]). Nickel resists oxidation and corrosion at elevated temperatures, but its resistivity is $\approx$ 4 times higher than that of annealed copper[15]. A good alternative regarding the nickel-alloys is kulgrid; which is a nickel-clad copper wire that was specifically developed to be used in applications where high temperatures, oxidising, or corrosive atmospheres exist. The cladding is only 27% of the total weight, and the resistivity is closer to that in annealed copper; this is $\approx$ 2.3x10^{-8} Ωm. Emphasis on the resistivity of the materials is made because this property increases with temperature, therefore if the electromagnet's energising coil is operating at elevated temperatures this would result in higher electrical resistance and, as a result, smaller magnetic field because less current would be flowing through the coil.

Ceramawire		
Characteristic	Unit	Value
Insulation	-	Vitreous enamel film
Temperature range Continuous operation Short periods	 °C 	 ≈540 ≈815
Conductor type	-	Kulgrid 27% nickel-clad copper
Conductor diameter	AWG mm	26 0.405
Resistivity	Ωm	$\approx 2.3 \times 10^{-8}$

Table 6.4: Material characteristics of the ceramic insulated wire used to wind the high temperature electromagnet's energising coil.

Regarding the wire insulation it was found that the highest heat resistance, amongst the organic-inorganic insulations, is that of the polyimide-silica insulation developed by Susuki *et al.* for Hitachi Cable (part of the Hitachi group); which is thermally rated as class 280 °C. However, a higher temperature resistance than that is required for the application considered here. Another alternative are inorganic materials, such as ceramic formulations, since they allow higher heat resistance insulations. A standout option amongst the commercially available ceramic insulated wires is Ceramawire HT, which is a kulgrid wire with a ceramic insulation that is firmly bonded to the wire that can operate continuously at ≈ 540 °C, or for short periods at ≈ 800 °C. Additionally, the ceramic insulation can assume the same flexibility as the base wire, thus it is ideal for winding the electromagnet's energising coil. Some relevant properties of this wire are presented in table 6.4, and the reader is referred to the technical specifications available in [16] for more details.

Thus, having chosen the materials to build the new electromagnet and following the design principles of the electromagnet used for the room temperature trials, a

laminated E-shaped iron core obtained from a 100 VA transformer, was chosen to confine and guide the magnetic field produced by the energising coil. The core dimensions are 86 mm length x 57 mm height x 28 mm width. The centre pole has an effective cross section area (A_c) of ≈ 784 mm^2, and was shortened by 3 mm so that the ceramic encapsulated spaced spiral coil can be accommodated.

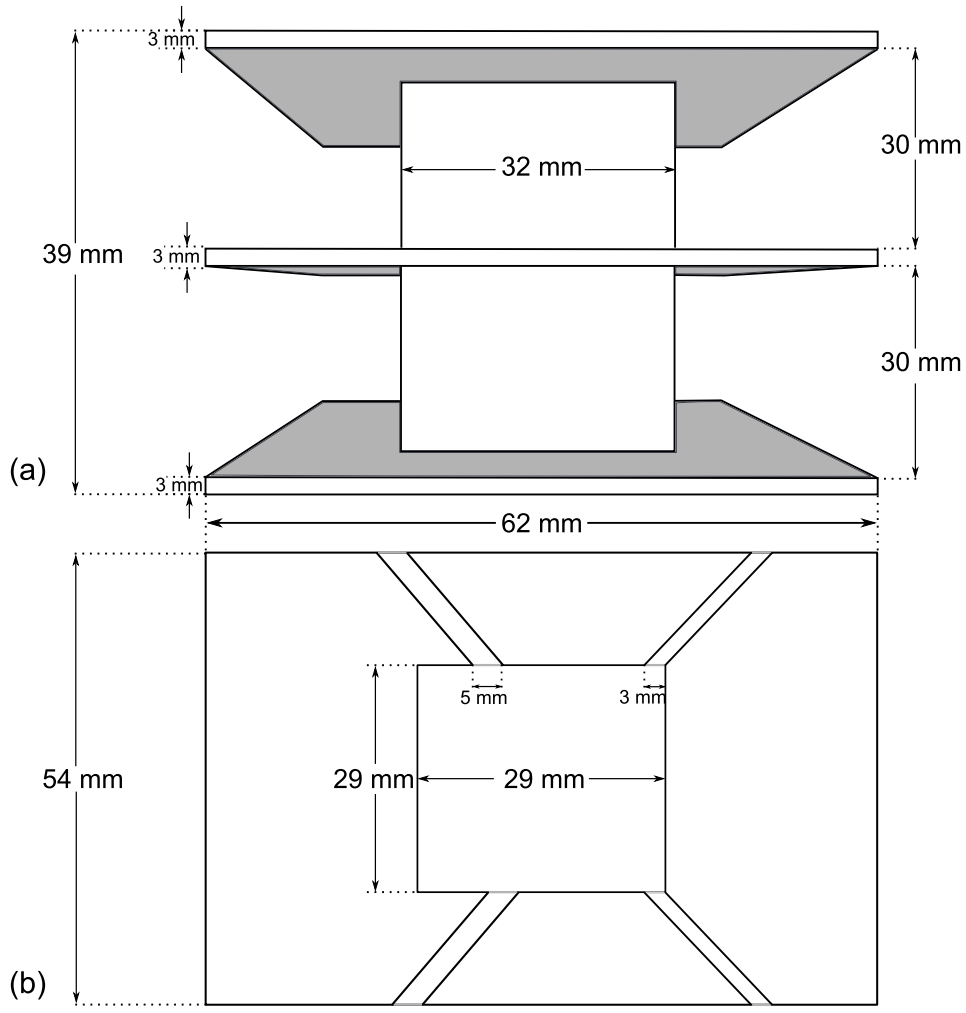

Figure 6.7: Schematic diagram of the ceramic coil MACOR former for high temperature applications: (a) side view and (b) bottom view. Photographs of the actual element can be seen in figure 6.8.

The new energising coil consists of two coils connected in parallel (equivalent resistance $\approx 6.2\ \Omega$), each one of them with ≈ 400 turns of the high temperature ceramic insulated nickel-clad copper wire (OD = 0.405 mm), and mounted on a ceramic former of dimensions shown in figure 6.7. In a similar fashion as with its preceding version, the ceramic former is on the centre pole of the electromagnet's core (see figure 6.8). Consequently, the electromagnet generates a magnetic field from the centre pole with the other poles providing a return path closing the magnetic circuit.

The flux density produced by the new electromagnet when it is operating on low carbon steel, was measured using the calibrated Hall-effect sensor and the experimental setup presented and described in section 5.4. As can be seen in figure 6.9, the measured magnetic flux density was 900 ± 20 mT. In comparison with its preceding version (see figure 5.14(a)), the flux density produced by the new electromagnet is similar in amplitude (within 5-10% difference) and both reach their maximum amplitude at the same time. This is because the pulse width of the current through the energising coil is determined by the electromagnet's driving circuit (see section 5.2), and that part of the system has not changed. An implication of this fact is that the optimisation process of the ultrasonic signal shown in section 5.6, does not have to be performed again, since the time delay used for triggering the EMAT pulser/receiver system is based on the time at which the flux density is at its maximum amplitude, and in both cases is 3 ms.

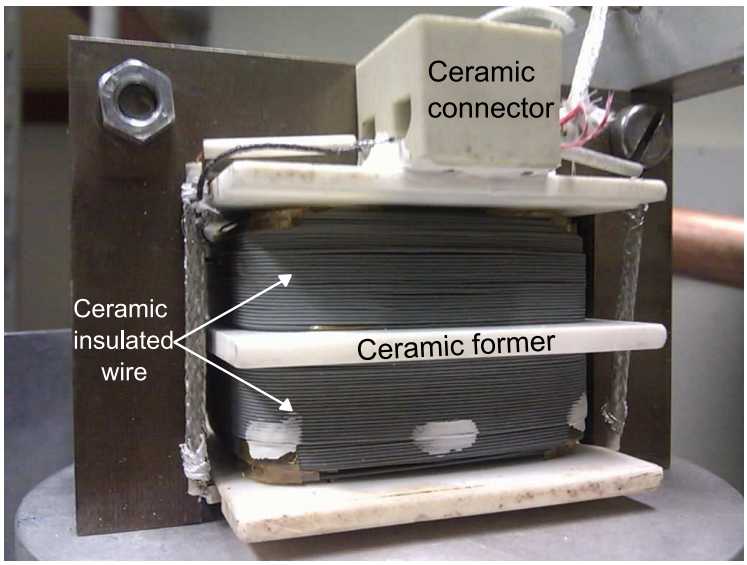

(a) Side view.

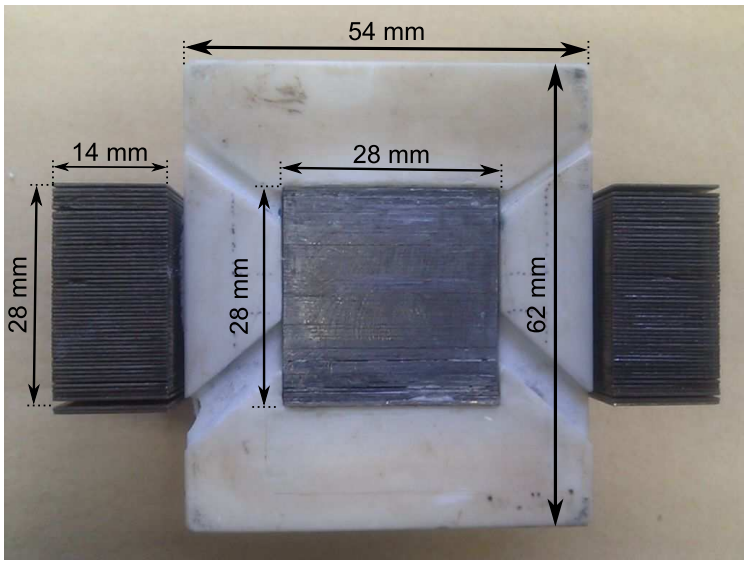

(b) Bottom view.

Figure 6.8: Photographs of the electromagnet used for high temperature trials. In contrast to the previous version, this has an energising coil wound with the ceramic insulated wire, and mounted on a ceramic former.

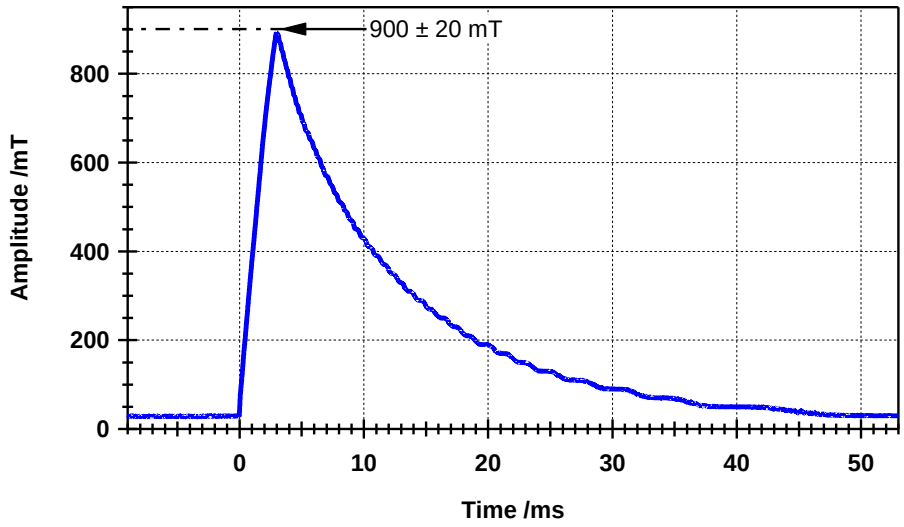

Figure 6.9: The above waveform shows the flux density measured by the Hall-effect sensor when the new electromagnet is operating on low carbon steel. In comparison with the waveform shown in figure 5.14(a) (see section 5.4), the flux density produced by the new electromagnet is similar in amplitude ($\approx$50 $\pm$ 20 mT difference) and both reach their maximum peak at the same time (3ms).

6.4 High temperature measurements

A description of the steps taken to transform the EMAT coil and electromagnet designed for room temperature trials, into elements capable of withstanding elevated temperatures, was presented in previous sections (6.1, 6.2 and 6.3). This section offers a detailed account of the experimental measurements carried out at a range of different temperatures, and is subdivided into two sections in order to present the results from the initial and final designs of the high temperature PE-EMAT.

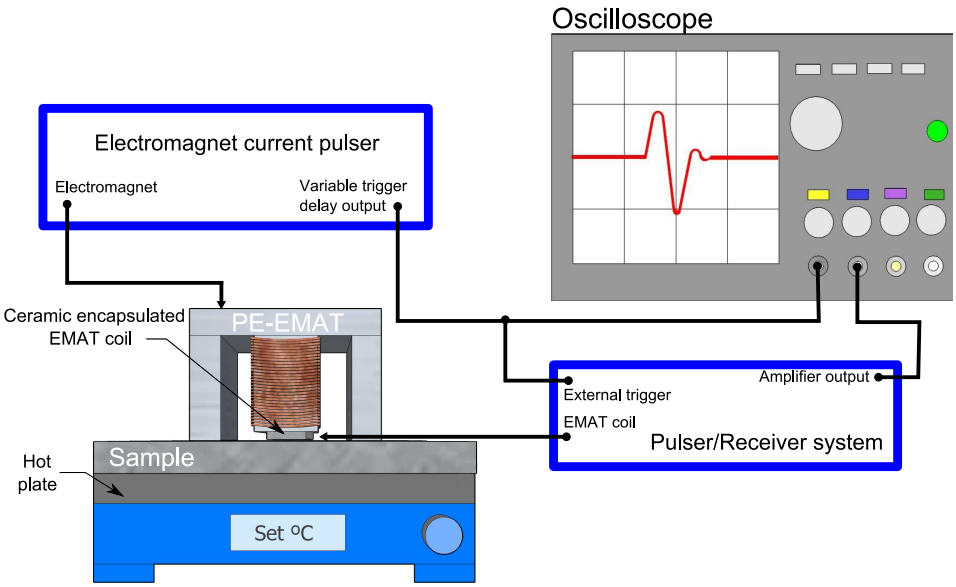

Figure 6.10: Schematic diagram of the experimental setup used to test the performance of the initial PE-EMAT prototype intended for high temperature applications.

6.4.1 Preliminary trials

The preliminary trials were performed using the same equipment that comprises the system presented in chapter 5, this is: the current pulser that drives the electromagnet, and the pulser/receiver system that drives the EMAT coil (see sections 5.2 and 5.3, for a detailed description on each piece of equipment). However, this time the PE-EMAT consisted of the electromagnet used for the room temperature trials and presented in section 5.1, and the ceramic encapsulated spiral coil shown in section 6.1.

The performance of this new PE-EMAT system at a range of different temperatures was investigated using the setup shown in figure 6.10; which only differed from the one presented in section 5.5 in that a hot plate heater was used to elevate and control the sample temperature, and a general purpose thermocouple type K (chromel-alumel) was employed to monitor the temperature of the sample surface. The purpose of the preliminary trials was to establish two key factors in the per-

formance of the PE-EMAT: its suitability to operate at elevated temperatures, and its limitations. Thus, in order to establish the suitability to operate at high temperatures, trials were performed using the following procedure: the low carbon steel sample (thickness = 19.7 ± 0.1 mm) was placed on the hot plate heater in order to reach a target temperature; meanwhile, the temperature in the sample surface was being monitored with the thermocouple. Once the temperature in the sample surface was stable the PE-EMAT was placed on the sample for a short period to take the measurements (typically less than 2 minutes) and it is removed once the signals (a single shot and an averaged signal (16x)) had been captured by the digital oscilloscope. The averaged signal is captured to obtain an improved SNR, although this is not strictly necessary since the SNR for a single-shot is good even at the highest temperature reached in this experiment (e.g. at 250 °C, SNR is 11 dB).

The performance of the PE-EMAT system for these part of the trials is presented in figure 6.11. Two consecutive back-wall echoes of the averaged ultrasonic signals obtained at a range of different temperatures, from room temperature (RT) to 250 °C, were selected to show the temperature dependence of the ultrasonic signal. A close-up of the first back-wall echo in the averaged ultrasonic signals obtained at RT and 250 °C, is presented in figure 6.12, and allows to see clearly the difference in amplitude and time of arrival between these signals. It is worth noting that when performing measurements at high temperatures there are physical changes in the sample that would result in errors if not taken into account. For instance, one of the most significant variation in the signal is the change in velocity as a function of temperature[17]. The gradual decrease in ultrasonic velocity with increasing temperature is well illustrated in figure 6.13, and if accurate thickness measurements are needed then the information obtained from this figure can be used to calibrate the system.

On a different note, in order to determine the limitations of this PE-EMAT, a dif-

ferent approach was utilised. Accordingly, the transducer was allowed to operate for periods of time that exceeded the safety threshold. It was found that for temperatures below 160 °C, the PE-EMAT system can operate even for long periods of time without noticing signs of failure. However, when the temperature goes above 170-180 °C, the insulation starts to deteriorate and, eventually, it melts if the temperature increases even more. The fumes produced by the insulation of the coil while is melting inside the ceramic encapsulation expands causing a damage in the bonding between the EMAT coil and the electromagnet, and a ringing in the signal appears. Figure 6.14 shows a comparison of the "clean" ultrasonic signal obtained at RT and that obtained when the ringing appears at 170 °C. In order to observe this effect, an image sequence was prepared using A-scans as those shown in figure 6.14, but for more temperature steps, and is available as a video file in Appendix A.2.1.

Taking into account the results from this section, and having in mind that high temperature ultrasonic measurements can be categorised in two different regimes according to the time that the transducer needs to be in contact with a hot sample: short-term and permanent contact. Thus, it can be said that this version of the PE-EMAT could perform better in applications as those for the first regime, such as spot-check thickness measurements; or where the ability to scan moving objects is required. In both cases the temperature must not exceed 250 °C, and the transducer must not be in direct contact with the sample for periods longer than two minutes.

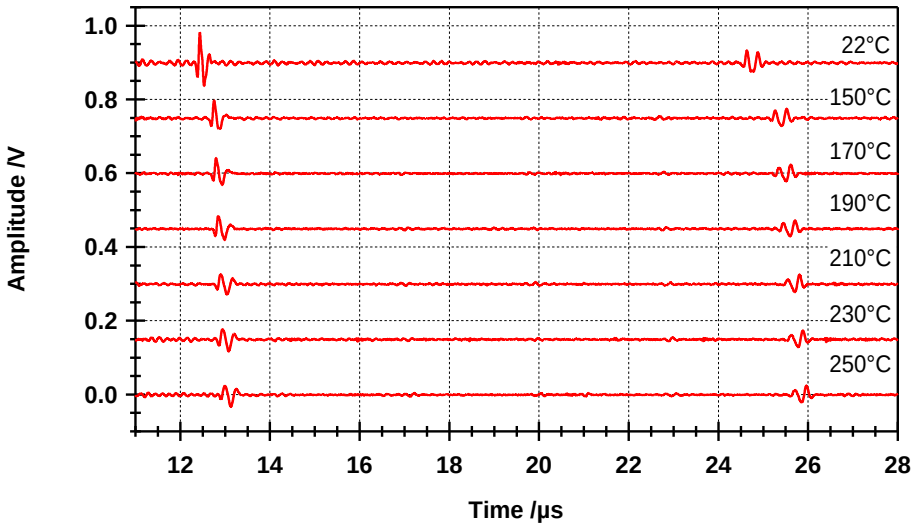

Figure 6.11: The above waveforms show two consecutive back-wall echoes in the averaged ultrasonic signal obtained in the preliminary high temperature trials (RT - 250 °C), when the PE-EMAT is operating on low carbon steel.

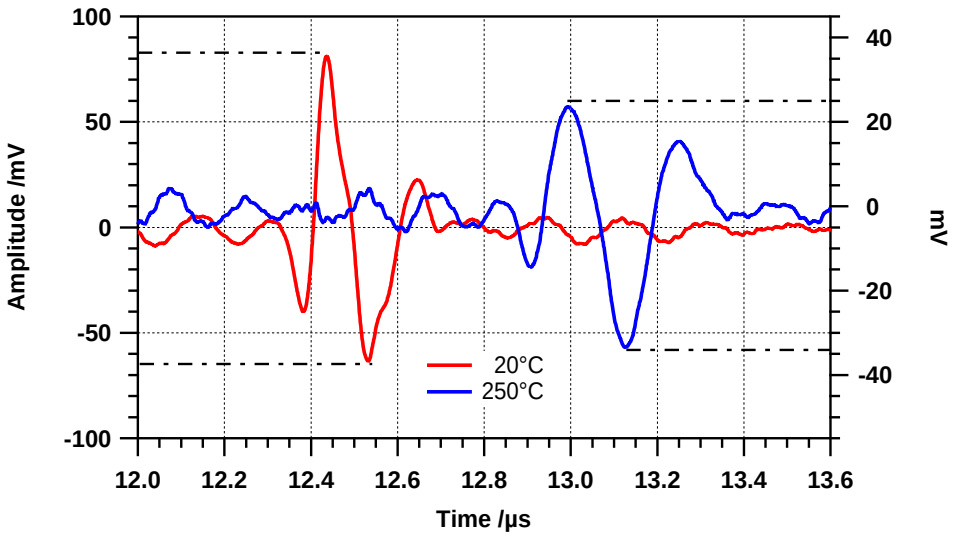

Figure 6.12: The above waveforms show the typical first back-wall echo in the averaged ultrasonic signal obtained in the preliminary high temperature trials, when the PE-EMAT is operating on low carbon steel. Note that the peak to peak amplitude for the ultrasonic signals are: 145 mv (20 °C), and 57 mV (250 °C).

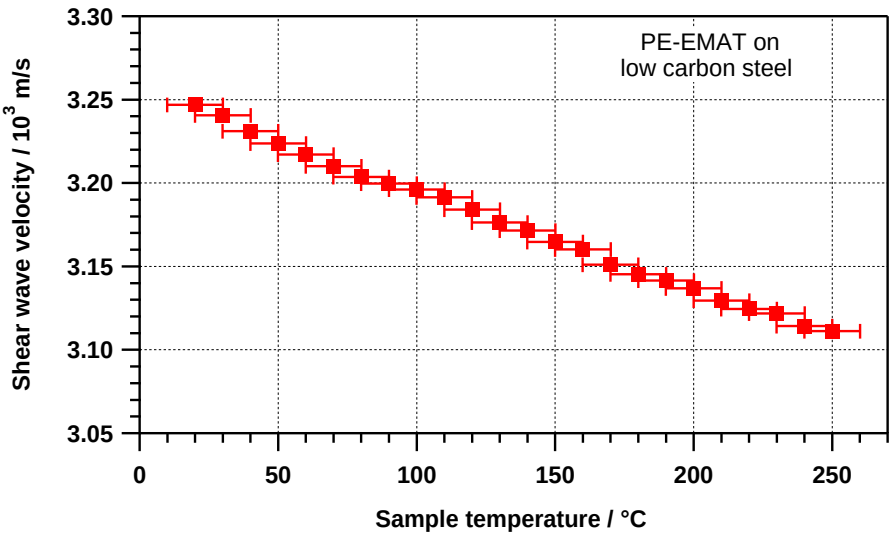

Figure 6.13: Shear wave velocity variation with temperature (RT-250 °C). Preliminary trials.

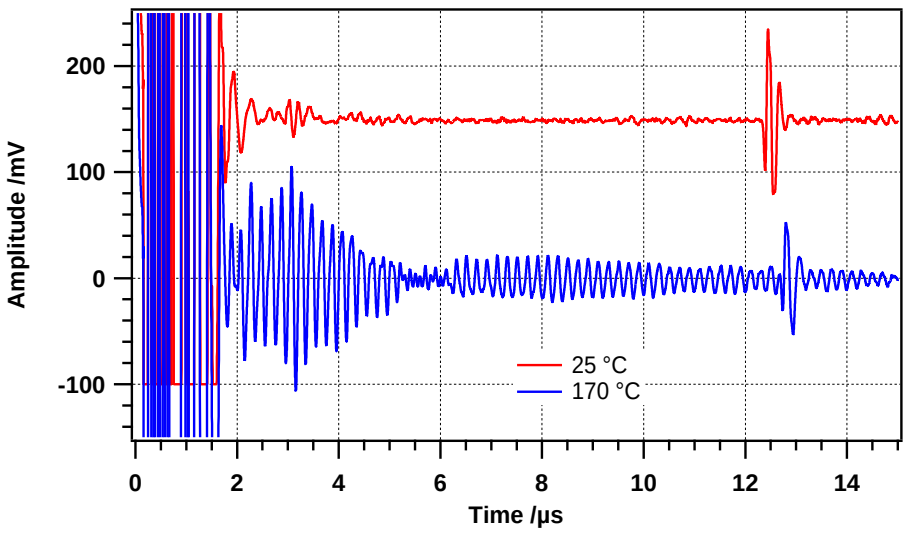

Figure 6.14: The ringing in the ultrasonic signal appears due to the deterioration in the polymer insulation of the coil and the consequent damage in the bonding between the ceramic encapsulated coil and the electromagnet, when the insulation is melting.

6.4.2 Final trials

The final trials were performed again with the current pulser that drives the electromagnet, and the pulser/receiver system that drives the EMAT coil. However, in this occasion, the PE-EMAT consisted of the electromagnet presented in section 6.3, and the spaced spiral coil presented in section 6.2.

In a similar fashion as with the previous version of the PE-EMAT, the purpose of these trials was to establish two key factors: its suitability to operate at elevated temperatures, and its limitations. Thus, in order to establish this suitability, trials were performed using the following procedure: the low carbon steel sample (thickness = 19.7 ± 0.1 mm) was placed inside a furnace and was heated up rapidly to the target temperature, and leaving it there to reach thermal equilibrium. Subsequently, the furnace door was opened and the sample surface temperature was measured in different points using an infrared thermometer (Fluke® 68). Finally, the PE-EMAT was positioned on the sample (as shown in figure 6.15) and the measurements were taken on the digital oscilloscope (a single shot and an averaged signal (16x)).

The reason for heating rapidly the sample from room temperature, was to minimise the degree of sample oxidation occurring during the course of the experiment. Even given this effort to avoid oxidation, there was still noticeable ferrous oxide on the sample surface after the experiment was carried out.

The performance of the PE-EMAT system for the final trials is presented in 6.16. Two consecutive back-wall echoes of the averaged ultrasonic signals obtained at a range of different temperatures, from room temperature (RT) to 600 °C, were selected to show the decrease in shear wave velocity with increasing temperature. A sequence of A-scan images, as those presented in figure 6.16, but for a wider range of temperatures is also available in Appendix A.2.2 to show the the progressive delay in the back-wall echoes and the effect of temperature on the signal amplitude.

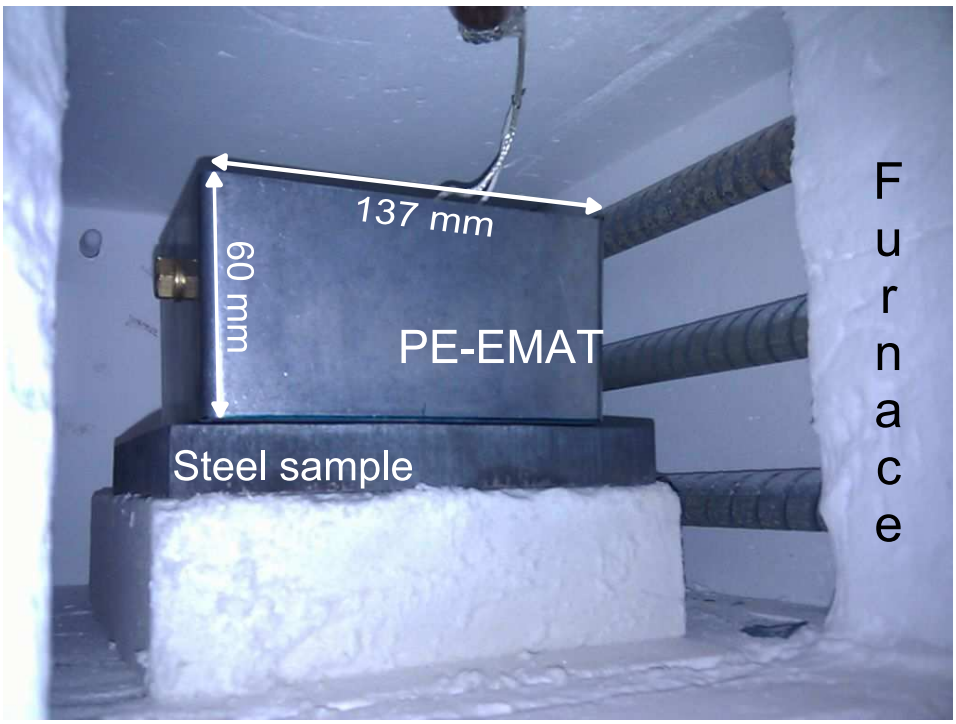

Figure 6.15: Photograph of the PE-EMAT inside the furnace for final trials.

In order to follow the same analysis as that in the previous section, a close-up of the first back-wall echo in the averaged ultrasonic signals obtained at RT and 600 ^{o}C, is presented in figure 6.17, and allows to see clearly the difference in amplitude and time of arrival between these signals. More formal calculations of the variation of shear wave velocity (taking into account thermal expansion), and the attenuation of the signal amplitude for this range of temperatures are presented in the following subsections.

It is worth noting that when the limitations of this PE-EMAT were tested it was found out that the ceramic coating in the wire starts to deteriorate after being constantly subjected to temperatures near 540 ^{o}C; which is the maximum continuous operation temperature of this wire (see table 6.4). When this happens the ceramic insulation breaks down causing a short circuit in the electromagnet's energising coil. During these trials it was determined that the safest time that the transducer can be

seated on the sample surface is approximately less than one minute when operating at temperatures above ≈ 350 °C.

Taking into account the results from this section, this version of the PE-EMAT system could be used in the short-term contact regime mentioned in 6.4.1; or where the ability to scan moving objects is required. In both cases the temperature must not exceed 600 °C. Regarding the suitability of the PE-EMAT system to be used in the permanent contact regime, there are still some tests that need to be done, especially those involving the cyclic exposure to elevated temperatures, and those regarding the aging characterisation of the rest of the elements in the PE-EMAT system: EMAT coil, ceramic encapsulation, alumina substrate, ceramic former, case and all the connections. It is very important to determine which element in the whole assembly is more likely to break when they are constantly subjected to elevated temperatures.

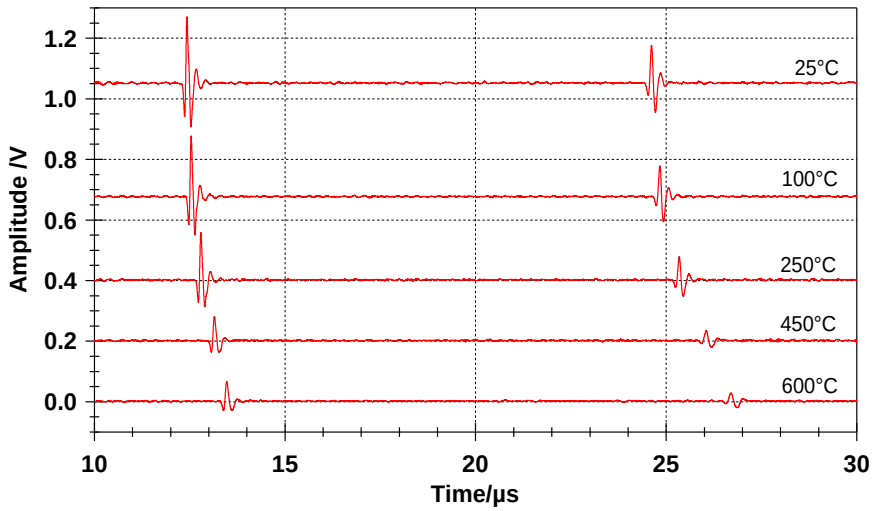

Figure 6.16: The above waveforms show two consecutive back-wall echoes in the averaged ultrasonic signal obtained in the final high temperature trials (RT - 600 °C), when the PE-EMAT is operating on low carbon steel.

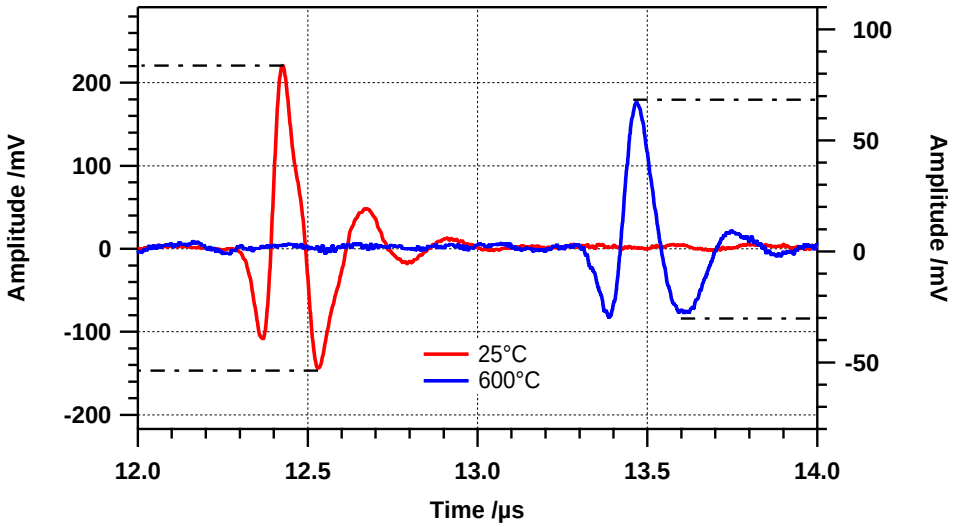

Figure 6.17: The above waveform shows the typical first back-wall echo in the averaged ultrasonic signal obtained in the final high temperature trials, when the PE-EMAT is operating on low carbon steel. Note that the peak to peak amplitude for the ultrasonic signals are: 365 mv (25 °C), and 98 mV (600 °C).

Ultrasonic velocity measurements

The shear wave velocity at room temperature was calculated with two consecutive back-wall echoes, using the well known relationship:

$$v_s = \frac{2L_{RT}}{t_2 - t_1} \tag{6.1}$$

where L_{RT} is the steel sample thickness (19.68 mm) at room temperature, and t_1, t_2 are the transit times for the first and second back-wall echoes (see figure 6.18).

The shear wave velocity for trials at elevated temperatures was calculated according to equation 6.1, with the exception of the sample thickness correction for thermal

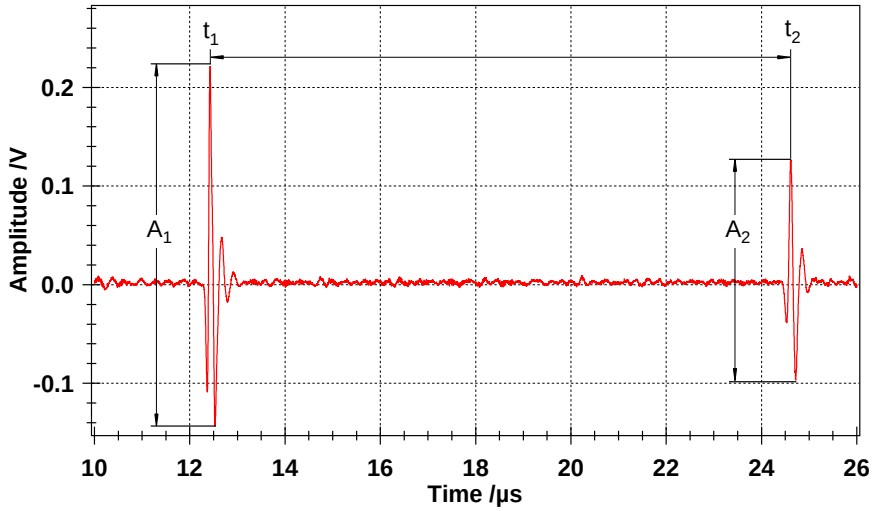

Figure 6.18: Typical A-scan obtained at room temperature, showing first and second back-wall echoes

Thermal expansion correction factors		
Temperature (°C)	α_{Th} ($10^{-}6$ °$C^{-}1$)	L_{ThExp} (mm)
Room temperature	10.77	19.681
100	12.29	19.699
250	14.07	19.74
450	15.74	19.811
600	16.49	19.872

Table 6.5: Thermal expansion value (α_{Th}) and actual sample thickness (L_{ThExp}) for representative experimental temperatures, used in equations 6.1, 6.2 and 6.3 to calculate the shear wave velocity and mass density changes in the low carbon steel sample.

expansion calculated using this equation.

$$L_{ThExp} = L_{RT}[1 + \alpha_{Th}(T - T_0)] \tag{6.2}$$

where T_0=25 °C, T is the temperature during the measurement and α_{Th} is the thermal expansion coefficient of steel at that temperature. Representative values of the thermal expansion correction factors (α_{Th} and L_{ThExp}), for a range of temperatures, is shown in table 6.5. Data from this table is used in equations 6.1, 6.2 and 6.3 to calculate the shear wave velocity and mass density changes in the low carbon steel sample.

The shear wave velocity as a function of increasing temperature is presented in figure 6.19. A linear downward trend in the experimental data is noticeable, however it is known that for temperatures above 600 °C) the decrease in the shear wave velocity is faster and no longer linear for low carbon steel, as reported by other researchers[19,20]. It is worth noting that errors in the calculation of the shear wave velocity arise mainly from the temperature measurements which can vary up to 10 %; which represents only a variation of ± 10 m/s in the shear wave velocity.

The mass density changes were calculated using equation 6.3.

$$\rho_T = \frac{\rho_0}{1 + 3\alpha_{Th}(T - T_0)} \tag{6.3}$$

where ρ_0 = 7850 kg m^{-3}, T_0, T and α_{Th} are the same as for equation 6.2.

For the range of temperatures considered here, a mass density change of ≈ 3% occurs and can be seen in figure 6.20; error bars are smaller than the marker size in the plot. This suggests that the effectively, as has been shown by other researchers[21,20], the mass density changes on the shear wave velocity is negligible and that changes in the elastic constants must be the dominant influence. See figure 2.1(b), in section

2.4; which shows a reduction of ≈39 % and ≈44 % in a mild steel sample for the Shear and Young's modulus, respectively.

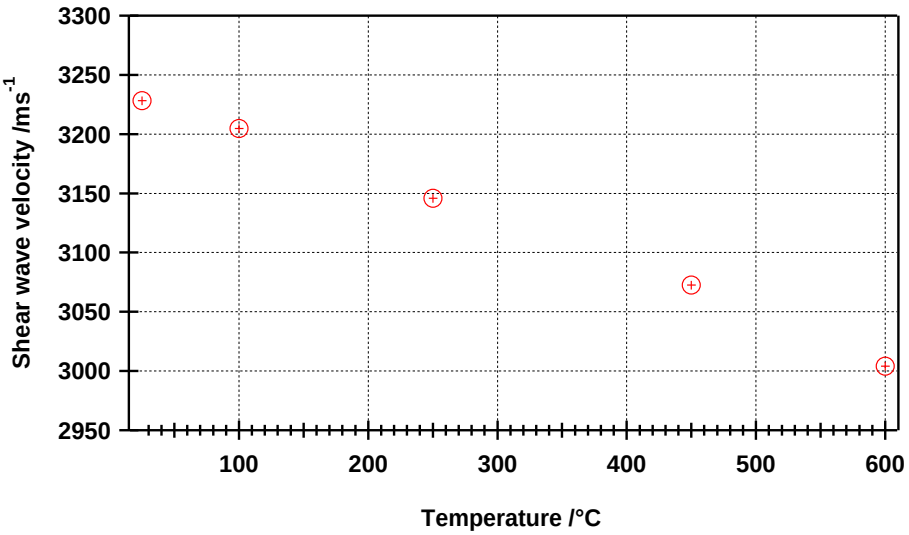

Figure 6.19: Shear wave velocity at a range of temperatures (RT-600 °C). Thermal expansion correction included.

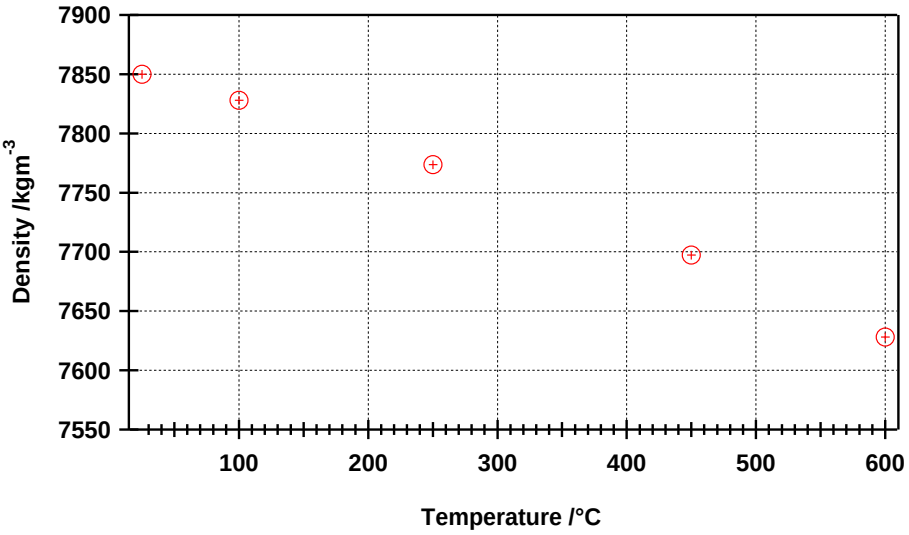

Figure 6.20: Mass density changes at a range of temperatures (RT-600 °C). Thermal expansion correction included.

Ultrasonic attenuation measurements

The amplitude of a wave will attenuate with the distance travelled, as was illustrated in figure 6.16. There are a number of mechanisms that contribute to this reduction (i.e diffraction of the wave front, absorption and scattering); which can be estimated by observing the amplitude decay in two consecutive back-wall echoes, and using the following equation

$$\alpha_{dB/mm} = (\frac{1}{x})(20log\frac{A_1}{A_2}) \tag{6.4}$$

where x is the distance travelled and A_1, A_2 are the initial and final amplitudes, respectively (measured as shown in figure 6.18). If this method is employed, the material attenuation in the low carbon steel sample is found to rise from ≈0.11 dB mm^{-1} at room temperature to a maximum of ≈0.16 dB mm^{-1} at 450 °C, before falling to ≈0.14 dB mm^{-1} at 600 °C, as can be seen in figure 6.22(a).

In order to obtain quantitative frequency dependent attenuation results, it is important to observe changes in the frequency content of each ultrasonic signal as the temperature increases. The magnitude FFT applied independently to a windowed section in the ultrasonic signal containing the first and second back-wall echo, is used to obtained the initial and final amplitudes (A_1 and A_2, respectively) needed to calculate attenuation using equation 6.4. These two values are taken from the corresponding magnitude FFT at the experimental temperature range (RT-600 °C), for a fixed frequency (e.g. centre frequency (cf) at RT = 4.27 MHz, or a representative fraction of this value), as shown in figures 6.21(a) and 6.21(b)). It is worth noting that these figures reveal that the higher frequencies are more strongly attenuated and, as a consequence, how the frequency content is changing as temperature increases.

The calculated attenuation using values for three different frequencies (4.27, 3.84,

and 3.41 MHz) is presented in figure 6.22(b). This figure shows that attenuation is heavily dependent on the frequency content of the ultrasonic signal, especially for the higher temperatures where large attenuation variations can be obtained when it is calculated for frequencies other than the centre frequency. For instance, at 600 ^{o}C, the calculated attenuation using A_1 and A_2 from the magnitude FFT for 4.27 MHz is 0.217 dB mm^{-1}, for 3.84 MHz (0.9*cf) is 0.15 dB mm^{-1}, and for 3.41 MHz (0.8*cf) is 0.106 dB mm^{-1}. Thus, it can be concluded that in order to get a better estimate of the attenuation it is important to determine first the centre frequency of the broadband ultrasonic pulse at room temperature, and then keep track of the changes to the frequency content in the ultrasonic signal as the temperature increases.

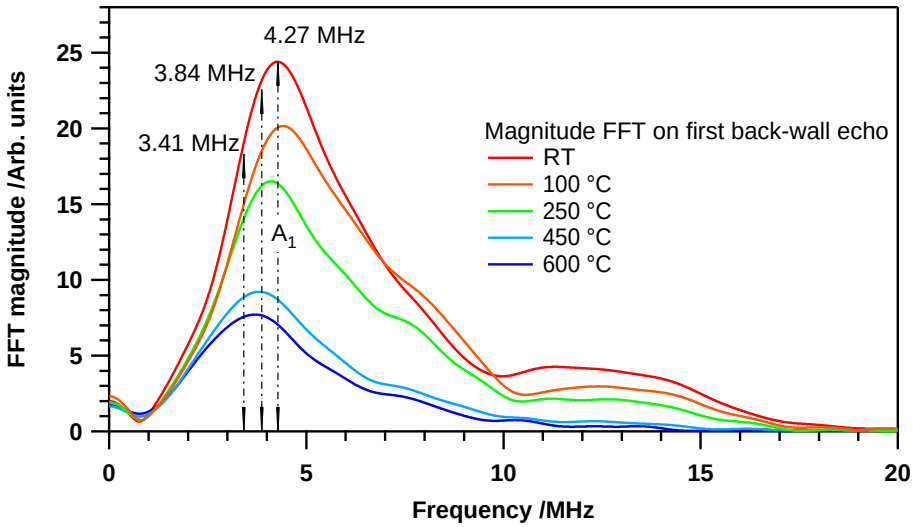

(a)

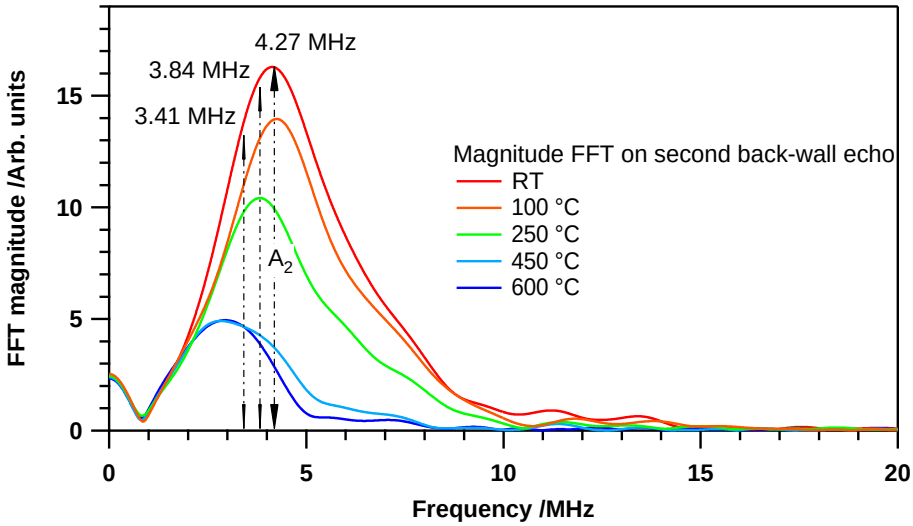

(b)

Figure 6.21: Magnitude FFTs applied to a windowed section of the ultrasonic signal containing only the: (a) first back-wall echo, and (b) second back-wall echo, for a range of temperatures (RT-600 °C).

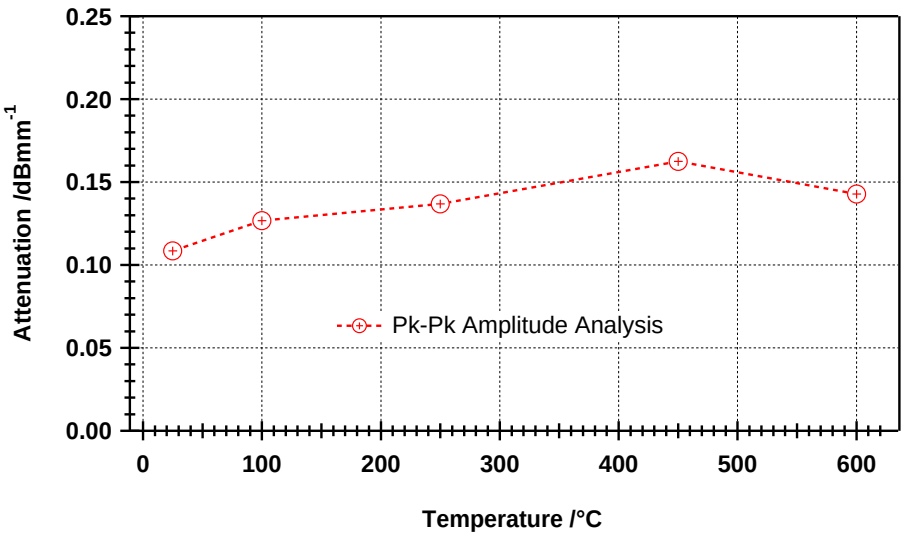

(a)

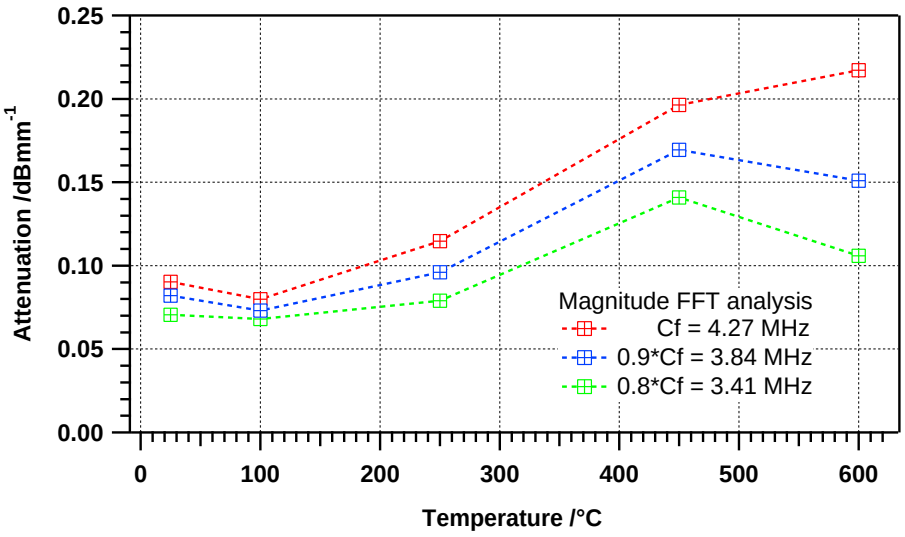

(b)

Figure 6.22: Attenuation changes at a range of temperatures on a steel sample using: (a) Pk-Pk and (b) magnitude FFT analyses.

6.5 Summary

The steps taken to transform the PE-EMAT described in the previous chapter, into a transducer capable of withstanding elevated temperatures without the use of any active cooling, were described in this chapter. Presented first are the design considerations of the EMAT coil for preliminary high temperature trials, which included: selection of a ceramic substrate to protect the front-face of the EMAT coil, and selection of a high temperature ceramic adhesive to encapsulate and bond this element to the centre pole of the electromagnet core. Also included was the main constraint encountered in the its use for temperature above 200 °C (see section 6.1). Then, the design considerations for an alternative EMAT coil that overcomes the insulation's constraint of its predecessor, were presented in a later section (see section 6.2), together with the finite element simulations performed for the electromagnetic analysis; which in this case included: calculation and visualisation of the magnitude of the current density induced by an alternating current in the final EMAT coil design; variation of the dynamic field when the lift-off is increased, and a comparison of the lift-off performance with respect to the performance of the previous coil design (see subsection 6.2.1). Subsequently, the design considerations taken towards building a new electromagnet were also presented (6.3), which included: selection of a suitable material for the coil former, and the selection of suitable insulated wire to wind the energising coil. Also included were the results of the flux density measurements when the new electromagnet was operating on low carbon steel (see figure 6.9).

Additionally, a detailed account of the experimental measurements carried out at a range of different temperatures, and subdivided into two sections in order to present the results from the initial and final PE-EMAT designs, was included in subsections 6.4.1 and 6.4.2. The results from experiments in subsection 6.4.1, demonstrated that

the preliminary design for the PE-EMAT system is capable of generating/detecting shear waves on low carbon steel at temperatures as high as 250 °C without using any active cooling system nor the necessity of sample preparation (see figures 6.11 and 6.12), as long as the transducer is not seated on the sample more than 2 minutes. It was also demonstrated that when the transducer was allowed to operate for periods that exceeded the safety threshold, and the temperature was above 170-180 °C, the coil's insulation starts to deteriorate and eventually melts if temperature increases even more, producing a mechanical ringing in the ultrasonic signal (see figure 6.14, and video in appendix A.2.1).

The results from experiments in subsection 6.4.2, demonstrated that the final design for the PE-EMAT system is capable of generating/detecting shear waves on low carbon steel at temperatures as high as 600 °C without using any active cooling system nor the necessity of sample preparation (see figures 6.16, 6.17, and video in appendix A.2.2), as long as the transducer is not seated on the sample more than 1 minute when operating at temperatures above $\approx$ 350 °C. It is worth noting that when the limitations of this PE-EMAT were tested it was found out that the ceramic coating in the electromagnet's energising coil starts to deteriorate after being constantly subjected to temperatures near 540 °C; which is the maximum continuous operation temperature for this wire (see table 6.4). Regarding the suitability of the PE-EMAT system to be used in the permanent contact regime, it was acknowledged that there are some tests that need to be done, especially those involving the cyclic exposure to elevated temperatures, and those regarding the aging characterisation of the rest of the elements in the PE-EMAT system.

References

[1] Epotek. Innovative epoxy adhesive solutions. Technical paper No. 11, 1980. URL epotek.com/SSCDocs/whitepapers/Tech%20Paper%2011.pdf.

[2] MWS. Insulation Characteristics and Applications. MWS wire industries, 2010. URL mwswire.com/inschar.htm.

[3] Md.S. Rohani. *The development of non-contact laser and EMAT ultrasound measurement systems for hot steel*. PhD thesis, University of Warwick, 1996.

[4] I.D. Kiteley. *A study of EMAT operation on ferromagnetic materials*. PhD thesis, University of Warwick, 1999.

[5] X. Jian, I. Baillie, and S. Dixon. Steel billet inspection using laser-EMAT system. *Journal of Physics D-Applied Physics*, 40:1501–1506, 2007.

[6] I. Baillie. *The development of a laser-EMAT system suitable for on-line inspection in the continuous casting plant-Innovation report*. PhD thesis, University of Warwick, 2008.

[7] Coorstek. Advance ceramic thick film substrates, ADS-96R, 2010. URL coorstek.com/resources/8510-1165ThickFilm.pdf.

[8] DuPont. Kapton, polyimide film, 2010. URL dupont.com/Kapton/en_US/.

[9] Aremco. High temperature ceramic adhesives and pastes. Technical bulletin A2, 2010. URL aremco.com/wp-content/uploads/2010/11/A2_091.pdf.

[10] F. Hernandez-Valle and S. Dixon. Initial tests for designing a high temperature EMAT with pulsed electromagnet. *NDT&E International*, 43(2):171–175, 2010.

[11] F. Hernandez-Valle and S. Dixon. Pulsed electromagnet EMAT for ultrasonic measurements at elevated temperatures. *Insight*, 53(2):96–99, 2011.

[12] Miles-Platts. Approved moulding materials for bobbins and coil formers, 2010. URL milesplatts.co.uk/assets/File/materials.pdf.

[13] Corning. Macor, machinable glass ceramic: properties and technical data, 2010. URL technicalproductsinc.com/pdf/macor.pdf.

[14] S. Jumonji, J. Senoo, K. Ueda, S. Chabata, S. Amano, and A. Ono. Super heat resistant ceramic insulated wire. In IEEE, editor, *Electrical electronics insulation conference, and Electrical manufacturing & coil winding conference*, 1995.

[15] G.W.C. Kaye and T.H. Laby. *Tables of physical and chemical constants*. Harlow-Longman, 16th edition, 1995.

[16] Ceramawire. Ceramawire high temperature magnet wire technical specifications, 2010. URL ceramawire.com/techspec.html.

[17] I. Atkinson, C. Gregory, S.P. Kelly, and K.J. Kirk. Ultrasmart: Developments in ultrasonic flaw detection and monitoring for high temperature plant applications. In *Proceedings of CREEP8*, pages 1–13, 2007.

[18] P. Crowther, C. Edwards, and S.B. Palmer. Ultrasonic thickness measurement of power station boiler tubes using electromagnetic acoustic transducers. *Insight*, 39(9):618–621, 1997.

[19] E.H.F. Date, M. Atkins, and G.V. Beaton. Measurement of the elasticity and ultrasound velocities of steel. *Ultrasonics*, 9(4):209–214, 1971.

[20] C.B. Scruby and B.C. Moss. Non-contact ultrasonic measurements on steel at elevated temperatures. *NDT&E International*, 26(4):177–188, 1993.

[21] R.J. Dewhurst, C. Edwards, A.D.W. McKie, and S.B. Palmer. A remote laser system for ultrasonic velocity measurement at high temperatures. *Journal of Applied Physics*, 63(4):1225–1227, 1988.

Chapter 7

Conclusions

7.1 Thesis review

In this body of work an overview of the basic ultrasonic theory on aspects relevant to this study was presented. For instance, the mathematical formulation used to describe time-varying deformations and internal restoring forces that lead to ultrasonic wave propagation in solid media; basic characteristics of longitudinal and shear (particle displacement and propagation directions, and phase velocity, see section 2.2); and a brief explanation of different mechanisms that have an impact on the amplitude of the ultrasonic wave as it travels through a medium (absorption, scattering, geometric attenuation, and dispersion, see section 2.3). Additionally, considerations on the effect of rise in temperature in solids were included (thermal expansion, density and elastic constants changes), together with references to quantitative data obtained by other researchers for range of temperatures that includes the experimental temperatures used in this body of work (see section 2.4).

It was also portrayed a review of the operation principles of Electromagnetic Acoustic Transducers (EMATs); including mechanisms that contribute to the coupling (Lorentz mechanism (see section 3.3), and magnetoelastic mechanisms (see section

3.4), detection mechanism (EMATs as particle velocity sensors, see section 3.5); typical coil designs and configurations, together with factors that have to be taken into consideration in the coil design to fully exploit the advantage of a couplant-free sample evaluation system (see section 3.6); and, finally, pulsed current electromagnets as an alternative to limitations of permanent magnets for high temperature applications.

Afterwards, a review of the progress of the most representative techniques/transducers employed for high temperature applications, such as: piezoelectric transducers, EMATs, laser-EMAT combinations, lasers, thermal techniques and eddy current probes, were presented. It was shown that the design of piezoelectric transducers is not only dependent on the selection of the piezoelectric material, as coupling to the test component must be considered. Additionally, since there is no definitive solution for high temperature couplants, references to short term and long term coupling materials, and to other technologies (sol gel and chemical deposition) were also given (see section 4.1). Regarding EMATs, details of various water-cooled versions of DC electromagnet and permanent magnet EMATs were included, together with different configurations for generation-reception, for instance: EMAT-EMAT configurations (pitch-catch or pulse echo), or Laser-EMAT configurations. It was acknowledged that the latter has attracted interest recently and a prototype system has been even developed to detect defects in steel on a pilot scale rolling mill, however some work has to be done to refine the system (see section 4.2). Regarding laser methods, details of various configurations were presented: such as a combination of high-energy Nd:glass laser as generator and a continuous wave laser interferometer as detector, or using a Q-switched Nd:YAG to generate and a reference beam laser interferometer to detect together with the solution to certain disadvantages for laser reception systems that need polished surfaces to enhance sensitivity (see section 4.3). Finally, two techniques that are also used for high temperature applications

were included in this chapter: Thermal (infrared testing and thermal imaging) and Eddy current testing. Advantages and factors affecting its response, together with some other weaknesses for both cases, are presented (see section 4.4).

Since the structure of this work broadly follows a chronological sequence in which research was undertaken. Subsequently, the steps taken towards the design and development of the pulsed electromagnet (PE)-EMAT and the supporting electronics, were shown. Emphasis was made in the description of the operation of each piece of equipment, and in the description of the optimisation process followed to obtain the maximum ultrasonic signal. The performance of the PE-EMAT sytem was tested and reported as: generation/detection of shear waves in different media (aluminium and low carbon steel, see section 5.7); effect of an oxide layer adhered to the sample surface (see section 5.8); and lift-off dependence (see section 5.9). The finite element simulations performed for the electromagnetic and ultrasonic analysis were reported in sections 5.10, 5.11, and 5.12. These included: the computation of the flux density produced by the electromagnet and its variation with lift-off (see section 5.10), the calculation and visualisation of the magnitude of the current density induced by an alternating current flowing in two different EMAT coil designs in non-magnetic and magnetic samples (see section 5.11); as well as the validation of the propagation of the ultrasonic wave generated/detected by the PE-EMAT (see section 5.12). The main findings of these experiments and simulations are presented in section 7.2.

Finally, the description of the steps taken to transform the PE-EMAT into a transducer capable of withstanding elevated temperatures without the use of any active cooling, was portrayed. The design considerations of the EMAT coil for preliminary high temperature trials, and the constraints in the its use for temperature above 200 ^{o}C were presented in section 6.1). In addition, the design considerations for an alternative EMAT coil that overcomes the insulation's constraint of its predecessor, were presented in a later section (see section 6.2). Subsequently, the design consid-

erations taken towards building a new electromagnet were also presented (6.3). A detailed account of the experimental measurements carried out at a range of different temperatures, and subdivided into two sections in order to present the results from the initial and final PE-EMAT designs, was included in subsections 6.4.1 and 6.4.2. The main findings of these experiments are also presented in section 7.2.

7.2 Findings

Main findings from chapter related to the design evolution for room temperature of the PE-EMAT system (5).

- The precise synchronisation of the triggering time of the current pulser that drives the EMAT coil, with the time at which the bias field provided by the electromagnet has reached its maximum value, was determined to be 3 ms, and presented in the ultrasonic signal amplitude optimisation (see section 5.6).

- From the comparison presented in 5.7, it was evident that the PE-EMAT system has better performance on low carbon steel to that obtained on aluminium samples. In fact, the first back-wall echo in the ultrasonic signal was approximately ten times bigger in steel than in aluminium (see comparison in figure 5.19). This result was explained in terms of the significantly higher bias magnetic field that was obtained when the PE-EMAT system was operating in the ferromagnetic sample, as was shown by experimental measurements in section 5.4 and confirmed by finite element simulations carried out in Comsol shown in section 5.10.

- Regarding the results presented in section 5.8, it was clear that an oxide layer, such as magnetite, enhance the signal amplitude when compared to that obtained in a "clean", bare metal surface. The presence of a magnetite layer lead

to an enhancement of 7.5 dB in the amplitude of the first back-wall echo in the ultrasonic signal, for the particular case considered here (see comparison in figure 5.21).

- Regarding the comparison presented in section 5.9, it was demonstrated that the PE-EMAT system has better lift-off performance when compare to that obtained using a permanent magnet EMAT (see comparison in figure 5.24). With similar decay factors per millimeter lift-off, the signal amplitude for the tested range of lift-off distances, was on average a factor of three larger with the PE-EMAT.

Main findings from chapter related to the design evolution for high temperature of the PE-EMAT system (6)

- An alternative design for the spiral coil was developed and presented in section 6.2), with the purpose of overcoming the coil's insulation constraint shown in section 6.1. Having changed the EMAT coil design, a new optimisation process to determine the number of turns for this coil was carried out and reported, together with the model in Comsol implemented to quantify the induced current density within the sample surface and the dynamic magnetic field profile across the EMAT coil radius. The results from these simulations are shown in subsection 6.2.1. In general terms, it was shown that increasing the lift-off would have the effect of making a region in the coil more sensitive between the centre and the edge. Additionally, it was demonstrated that the spaced spiral coil has a wider region on which the coil would be more sensitive than its predecessor at 2mm lift-off (see figure 6.6).

- Regarding the final version of the electromagnet's energising coil, it was determined that a standout option amongst the commercially available high temperature wires is Ceramawire, which is a nickel-clad copper wire with a

firmly bonded ceramic insulation that can operate continuously at ≈ 540 °C, or for short periods at ≈ 800 °C. Additionally, the ceramic insulation can assume the same flexibility as the base wire, thus it is ideal for winding coils (see section 6.3). As can be seen in figure 6.9, the measured magnetic flux density was 900 ± 20 mT; which in comparison with its preceding version (see figure 5.14(a)), is similar in amplitude (within 5-10% difference).

- The results from experiments in subsection 6.4.1, demonstrated that the preliminary design for the PE-EMAT system is capable of generating/detecting shear waves on low carbon steel at temperatures as high as 250 °C without using any active cooling system nor the necessity of sample preparation (see figures 6.11 and 6.12), as long as the transducer is not seated on the sample more than 2 minutes.

- It was also demonstrated that when the transducer was allowed to operate for periods that exceeded the safety threshold, and the temperature was above 170-180 °C, the coil's insulation starts to deteriorate and eventually melts if temperature increases even more, producing a mechanical ringing in the ultrasonic signal (see figure 6.14, and video in Appendix A.2.1).

- The results from experiments in subsection 6.4.2, demonstrated that the final design for the PE-EMAT system is capable of generating/detecting shear waves on low carbon steel at temperatures as high as 600 °C without using any active cooling system nor the necessity of sample preparation (see figures 6.16, 6.17, and video in appendix A.2.2), as long as the transducer is not seated on the sample more than 1 minute.

- It was found out that the ceramic coating in the wire starts to deteriorate after being constantly subjected to temperatures near 540 °C; which is the

maximum continuous operation temperature of this wire (see table 6.4). When this happens the ceramic insulation breaks down causing a short circuit in the electromagnet's energising coil.

- The shear wave velocity as a function of increasing temperature is presented in figure 6.19. A linear downward trend in the experimental data is noticeable, however it is known that for temperatures above 600 ^{o}C the decrease in the shear wave velocity is faster and no longer linear for low carbon steel, as reported by other researchers (see references 19 and 20, from this chapter).

- The mass density change of $\approx$ 3% occurs for the range of temperatures presented here and is shown in figure 6.20. This suggests that the mass density changes on the shear wave velocity is negligible, as has been shown by other researchers (see references 20 and 21, from this chapter); and that changes in the elastic constants must be the dominant influence. See figure 2.1(b), in section sec:EffectRiseTemp; which shows a reduction of $\approx$39 % and $\approx$44 % in a mild steel sample for the Shear and Young's modulus, respectively.

- The attenuation as a function of increasing temperature is presented by using two different analyses: time and frequency domain. Results from both analyses are presented in figures 6.22(a) and 6.22(b). It is clear from these figures that it is a better practice to use the frequency analysis since attenuation is heavily dependent on the frequency content of the ultrasonic signal. It was concluded that keeping track of the changes of the frequency content in the ultrasonic signal for the range of temperatures in the experimental measurements allows to get a better estimate of attenuation as a function of temperature.

7.3 Future work

There are exciting prospects for developing this system even further and additional characterisation of the PE-EMAT system is required to improve its performance and to make an industrial prototype viable.

For instance, there are a series of tests that need to be done regarding the cyclic exposure to elevated temperatures. It is a fact that the ceramic insulation of the Ni-Cu alloy wire employed in the electromagnet energising coil is stressed during winding and it is further stressed by temperature changes, thus it is important to measure the ability of the ceramic insulation to resist cracking when it is exposed to changes of temperature. This can be done by increasing or decreasing the temperature at low changing rates until the target temperature is reached, or by changing the temperature at a very high rate (typically 30 ^{o}C per minute or higher). The cyclic exposure should be repeated until the ceramic insulation fails the proof test, and the time to failure is calculated. Likewise, the characterisation of the aging of the rest of the elements in the PE-EMAT system is required: EMAT coil, Ceramic encapsulation, alumina substrate, ceramic former, case and all the connections. It is very important to determine which element in the whole assembly is more likely to break when they are subjected to changes in temperature.

On a different note, there are identified areas in which the PE-EMAT system can be improved, both in its design and/or the supporting electronic circuits. For instance, the actual electromagnet design could be improved to generate a higher flux density, using a larger electromagnet core and/or pulsating a higher current through the energising coil. However, if the size of the transducer is too large to follow certain surface geometry or to be introduced into restricted spaces (e.g. inside a small diameter pipe), then a smaller electromagnet is needed, and, again, a change in the core and the energising coil could be designed in order to produce a suitable flux

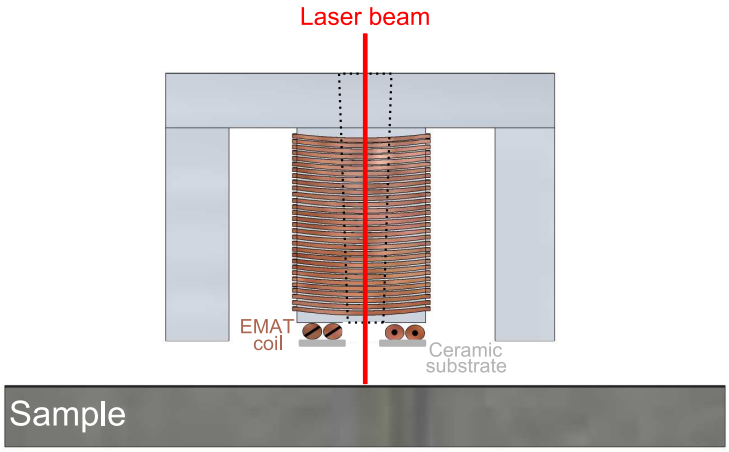

Figure 7.1: Laser/PE-EMAT combination. A Proposal for future work.

density for the EMAT operation. Additionally, a more efficient pulser to energise the electromagnet coil is essential, the actual design is bulky and heavy. In order to solve that issue, higher specification capacitors (as those used in the switched-mode power supplies) are needed, this would result in a size and weight reductions, as well as in a reduction of the cost of the circuit. Also, the amplifier electronics can be improved in the pulser/receiver system in order to reduce the time in which the detection circuitry is paralysed by the current pulse discharged through the EMAT coil, in order to make inspection of thinner samples viable.

In this body of work the defect detection capabilities of the PE-EMAT system were not demonstrated. Thus, some tests with the PE-EMAT mounted on a suitable set of samples containing real defects, would be very valuable to demonstrate its accuracy and detection capabilities. These trials could be perform at room temperature, as well as at elevated temperatures. Regarding those trials at higher temperatures it could be also the opportunity to demonstrate the capabilities of scanning hot moving objects.

Lastly, an interesting combination to evaluate would be a laser generation source and the PE-EMAT system acting as a detector. For this purpose, a small diameter

opening in the central length of the electromagnet core and a concentric EMAT coil (inner diameter equal to the diameter of the opening in the core, and outer diameter equal or minor to the width of the central length), could be used to allow the laser beam to be focused and deposited on the sample surface, as can be seen in figure 7.1. In this manner, the advantages of having a more efficient ultrasound generator and an optimised detector could bring the best of both systems together to be applied in high temperature applications.

Appendix A

Multimedia content

A.1 Ultrasonic propagation modelling

Description: This video file is the result of the transient, finite element simulation used to validate the propagation of the ultrasonic waves generated/detected by the PE-EMAT system presented in this body of work, and described in section 5.12.

The video is composed of a sequence of images as those presented in figure 5.34, but for a wider time range (from 1 to 14μs), with a time-step of 1μs. Each image contains the element x-velocity in the steel sample after having applied a generating shear force with the characteristics shown in figures 5.32(a) and 5.32(b).

Horizontal axis: Length of the steel sample.

Vertical axis: Width of the steel sample.

Colour scale: x-velocity magnitude.

Video codec: XviD.

Click here to see the video.

A.2 Ultrasonic propagation at high temperature

A.2.1 Preliminary trials at high temperature

Description: This video contains a sequence of A-scan images, as those presented in figure 6.16. Each A-scan was obtained using the experimental setup described in subsection 6.4.1, when the PE-EMAT system was operating in a low carbon steel sample (thickness = 19.7 ± 0.1 mm) at a range of different temperatures; from room temperature up to 170 °C.

The main purpose of this video is to show the effect of temperature on the signal amplitude and in the wave velocity (the progressive delay in the first back-wall echo is noticeable). Additionally, it also has the purpose of showing the ringing that appears in the signal as a consequence of the deterioration of the polymer film insulation and the damage in the bonding between the ceramic encapsulated EMAT coil and the electromagnet's core, when the PE-EMAT system has been operating on a hot sample for long periods of time.

Horizontal axis: Time /μs.

Vertical axis: Signal amplitude /V.

Colour scale: N/A.

Video codec: XviD.

Click here to see the video.

A.2.2 Final trials at high temperature

Description: This video contains a sequence of A-scan images, as those presented in figure 6.16, but for a wider range of temperatures. Each A-scan was obtained using the experimental setup described in subsection 6.4.2, when the PE-EMAT system was operating in a low carbon steel sample (thickness = 19.7 ± 0.1 mm) at a range of different temperatures; from room temperature up to 600 ^{o}C. The purpose of this video is to show the effect of temperature on the signal amplitude and the decrease in the wave velocity (the progressive delay in the back-wall echoes is noticeable).

Horizontal axis: Time /μs.

Vertical axis: Signal amplitude /V.

Colour scale: N/A.

Video codec: XviD.

Click here to see the video.